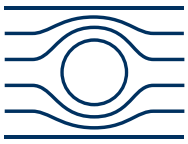

TECHNISCHE UNIVERSITÄT MÜNCHEN

WALTHER-MEISSNER-INSTITUT

BAYERISCHE AKADEMIE DER WISSENSCHAFTEN

Development of Surface Acoustic Wave Resonators Based on Thin-Film Lithium Niobate for Circuit Quantum Acoustics Platforms

Master's thesis

Alexander Jung

Supervisor: Priv.-Doz. Hans Huebl

Advisor: Thomas Luschmann

Garching – November 29, 2022

Abstract

Circuit quantum acoustodynamics (cQAD) is a novel platform to study the light-atom interaction in the giant-atom limit, i.e. the size of the atom is comparable to or exceeds the wavelength of the light. Therefore, the interaction dynamics go beyond the dipole approximation and thereby give access to interesting and novel physics. In this thesis, we explore a cQAD system, where a superconducting quantum bit (qubit) is coupled to a surface acoustic wave resonator. To this end, we study the behaviour of surface acoustic wave resonators in the GHz-regime and at cryogenic temperatures for different substrates. In particular, we compare the behaviour of surface acoustic wave resonators on piezoelectric lithium niobate (bulk) and novel multi-layer substrates, i.e. a thin layer of lithium niobate on silicon. We find, that the model of two-level fluctuators describes one loss contribution of these SAW resonators well. We observe strong indications, that two-level systems degrade the coherence properties in the single phonon limit considerably for the multi-layer systems compared to the bulk lithium niobate substrates, which can be intuitively attributed to the presence of TLS at the interface or within the oxide layer. Subsequently, we discuss two different versions of how to couple a superconducting qubit to a surface acoustic wave resonator, while avoiding a piezoelectric material as substrate for the qubit. Finally, we design two chips for a flip-chip assembly and after pre-characterization measure the coherence times of a single flux-tunable transmon qubit.

Contents

Chapter 1

Introduction

Lord Rayleigh discovered the first type of surface acoustic wave (SAW) in the year 1885 and at this time the main application was seismology [1, 2]. With the advent of the interdigitated transducer (IDT), a thin-metal film on a piezoelectric substrate, on-chip SAW devices for electronic applications became viable [3]. There are multiple different SAW devices in use in nowadays electronics: delay lines, bandpass filters, pulse compression filters and the SAW resonator/cavity in which standing SAWs form [4–7]. As bandpass-filters for communications, in particular for mobile phones, SAW devices are ubiquitous, because of their low insertion loss (less than $1\,\mathrm{dB}$) and small device footprint [2, 6], for sensors, e.g. biosensors that permit highly sensitive detection of biorelevant molecules in liquid media, for ultra-sound imaging and for gas sensing applications [8–10].

However, our focus in this thesis is on quantum applications: The quantum mechanical nature of mechanical oscillators might not be obvious in our everyday life, but even macroscopic mechanical cavities can be cooled to their quantum mechanical ground state [11]. Mechanical excitations in the form of bulk acoustic waves (BAWs) have been demonstrated to coherently interact with quantum bits (qubits) [12]. These mechanical excitations are of interest for the storage of quantum states, because of their long coherence times [12]. The SAW is also a mechanical excitation and the strain, electric or magnetic fields associated with SAWs allow for high precision control and measurement of qubits with applications in quantum information, memory, transduction and sensing [13–15]. In the future, multiple quantum processors need to be combined into quantum networks in order to leverage their full quantum-information processing capabilities [16]. Efficient microwave to optical conversion is a prerequisite for these networks and some schemes utilize piezoelectric materials and SAWs [16–18].

For this thesis, we focus on circuit quantum acoustodynamics (cQAD) in particular on the interaction between a superconducting qubit and a surface acoustic wave resonator. In analogy with circuit quantum electrodynamics (cQED), which covers the interaction between superconducting microwave circuits and a qubit, the novel field of cQAD describes the piezoelectric coupling between a SAW and a qubit [19]. The SAW wavelength for applications in the GHz-regime is on the order of the size of the qubit or artificial atom, because of the slow SAW velocity ($\mathrm{km/s}$) in comparison with the velocity of light ($10^8\mathrm{m/s}$). The artificial atom can interact with the SAWs in the cavity at different points. This leads to interference effects, which give rise to interesting physical phenomena, such as a frequency dependent relaxation rate and lamb shift [19–21]. Even more interesting effects arise, when the so-called giant-atom limit is investigated. This limit also allows to couple two qubits via a SAW cavity while suppressing loss via the latter [20, 22]. Technically, the realization of cQAD devices faces an inherent challenge:

While a large piezoelectric coupling is desired for the SAW cavity, the piezoelectric coupling adds another loss channel for the superconducting qubit. Therefore, the coherence times of the superconducting qubits for the cQAD in Ref. [19] are lower than the state of the art for superconducting qubits on a silicon substrate [23]. There are different approaches to circumvent this issue: One approach is a flip-chip geometry, where the superconducting microwave components on one chip are spatially separated from the acoustic cavity on another chip and the components on the different chips interact through an inductive coupler [14, 15]. The advent of commercially available thin film lithium niobate on silicon wafers opens up an alternative approach - the planar integration of microwave and acoustic cavity on the same chip which involves etching away the piezoelectric layer in proximity of the microwave components. This planar integration provides a clear path to scale up cQAD with the usual planar semiconductor fabrication methods.

This thesis addresses two main objectives: (i) To survey and understand the behaviour of SAW resonators on three different substrates, namely bulk lithium niobate and two multi-layer thin film lithium niobate at cryogenic temperatures. Since this multi-layer material platform has only recently become available, we need to understand the loss mechanisms for the resonators on the multi-layer substrate and compare them to resonators on the established bulk lithium niobate. (ii) Use this information about SAW resonators to envisage and realize a SAW resonator coupled to a superconducting qubit for a cQAD experiment.

In accordance with the two goals, this thesis is split into two parts. The first part focuses on SAW resonators: We discuss the theory in chapter 2 and the experimental methods in chapter 3. The last chapter of this part, chapter 4 discusses the experimental results of our SAW resonator measurements. The second part is dedicated to cQAD: We start with a general discussion on the two different approaches for cQAD in chapter 6. Then we discuss the theory of our superconducting circuit components in chapter 5 and the design for our cQAD chip in chapter 7. Subsequently we introduce the methods for the cQAD measurements in chapter 8 and characterization measurements of qubit in chapter 9. Finally, we summarize the results of both parts and give an outlook in chapter 10.

Part I

Surface Acoustic Wave Resonators

Chapter 2

Theory

Surface acoustic waves (SAWs) are propagating, evanescent acoustic and electric waves confined to the surface of a solid. They accompany a local displacement of the solid a well as local elastic deformations, where their amplitude is localized at the interface and decays on the characteristic wavelength λ [2, 24] (see Fig. 2.1.1 (a)). In this chapter, we present a general introduction into the equations of motion of the SAWs on anisotropic materials and discuss the fundamental properties of SAWs. We place a special focus on multi-layer substrates, where the SAWs are no longer dispersion-free [25]. In order to understand SAW dynamics on multi-layer substrates, we employ finite element simulations. Once we established the behaviour of the SAWs on different substrates we discuss aspects of the transduction of SAWs to electromagnetic waves and vice versa and how to confine standing SAW waves between two Bragg-mirrors to form SAW resonators. The substrate material and the geometry of the SAW resonator have consequences on the performance of these SAW resonators. We also introduce the standard two-level system (TLS) model which will be used later on to gain deeper understanding in the loss mechanisms of SAW resonators in our experiments.

2.1 Surface Acoustic Waves in Anisotropic Materials

While the phenomenon of a surface acoustic wave (SAW) is present in many disciplines, e.g. seismology, digital signal processing for communications and non-destructive testing we will focus on SAWs present at the interface between a piezoelectric and vacuum [2, 6, 26]. This also allows to interface or convert SAWs to electrical signals or vice versa via the piezoelectric effect (see Fig. 2.1.1 (b)). We explain the piezoelectric effect with an example, i.e. a two dimensional crystal with three polar axes. In the absence of an external force (left) the positive and negative charge densities are on top of each other and there is no electric field. If there is a force $\vec{F}$ along one of these polar axes (right) the positive and negative charge densities are displaced against each other and the result is a finite electric field [27]. While the surface acoustic wave problem can be solved analytically for isotropic materials, isotropic materials have per definition no polar axes and are not piezoelectric. Therefore, the presence of piezoelectricity in the solid is connected with its crystal structure and then we need to consider the impact of piezoelectricity and crystalline anisotropy on the propagation properties of the SAWs, which we will discuss here.

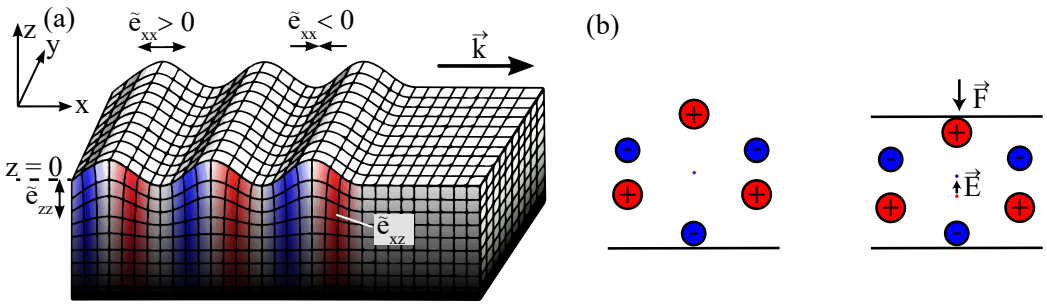

Figure 2.1.1: (a) Illustration of a Rayleigh SAW on an isotropic half space with the wavevector $\vec{k} \parallel x$ and the strain components $\tilde{e}_{xx} \parallel \vec{k}$ and $\tilde{e}_{zz} \perp \vec{k}$. $\tilde{e}_{xz}$ is color coded with $\tilde{e}_{xz} > 0$ in blue and $\tilde{e}_{xz} < 0$ in red. The interface between solid and vacuum is at $z = 0$. (b) Illustration of the piezoelectric effect. Panel (a) is adapted from [28].

Fundamental equations. The general wave equation

$$\rho \frac{\partial^2 u_i}{\partial t^2} = \sum_j \frac{\partial \sigma_{ij}}{\partial j}, \ (i, j = x, y, z) \tag{2.1}$$

describes the temporal and spatial propagation of a wave in a solid with density ρ, with the displacements $\vec{u} = (u_x, u_y, u_z)^T$ and stress components σ_{ij} [2]. The spatial directions are x, y, z. For a piezoelectric and anisotropic substrate the components σ_{ij} can be expressed as

$$\sigma_{ij} = \sum_{kl} \mathbf{C}^{\mathrm{E}}_{ijkl} \tilde{e}_{kl} - \sum_k e_{kij} E_k, \ (i, j, k, l = x, y, z). \tag{2.2}$$

Here, the first term on the right hand side of the equation describes the mechanical response of the solid given by the strain components $\tilde{e}_{ij} = 1/2(\partial u_k/\partial j + \partial u_j/\partial k)$ and the stiffness tensor $\mathbf{C}^{\mathrm{E}}_{ijkl}$ [2]. The second term describes the mechanical response of the solid to a constant electric field $\vec{E}$ via the piezoelectric tensor e_{kij} and the components of the electric field E_k [2]. The electric displacement $\vec{D}$ is given by Ref. [7] as

$$D_i = \sum_j \varepsilon^{\tilde{e}}_{ij} E_j + \sum_{jk} e_{kij} \tilde{e}_{jk}, (i, j, k = x, y, z) \tag{2.3}$$

with $\varepsilon^{\tilde{e}}_{ij}$ the permittivity tensor at constant strain. For an insulator with no free charges $\nabla \cdot \vec{D} = 0$ must hold. Within the regime where the quasi-static approximation, where the electric variables are governed by electrostatics and $\vec{E} = -\nabla\Phi$ is fulfilled, the combination of (2.1)-(2.3) can be

rewritten in the form:

$$\rho \frac{\partial^2 u_i}{\partial t^2} - \sum_{jkl} C^E_{ijkl} \frac{\partial^2 u_k}{\partial j \partial l} - \sum_{kj} e_{kij} \frac{\partial^2 \Phi}{\partial j \partial k} = 0 \tag{2.4}$$

$$\sum_{ikl} e_{ikl} \frac{\partial^2 u_k}{\partial i \partial l} - \sum_{ik} \varepsilon^{\tilde{e}}_{ik} \frac{\partial^2 \Phi}{\partial i \partial k} = 0, \ (i, j, k.l = x, y, z)[2]. \tag{2.5}$$

(2.4) and (2.5) must be solved with appropriate boundary conditions to extract the parameters of SAW propagation.

SAW solutions to fundamental equations. To solve (2.4) and (2.5), we assume a general solution with linear combinations of partial waves for the displacement $\vec{u}_m$ and electric potential Φ_m

$$u_{j,m} = \alpha_{j,m} \exp\{ikb_m z\} \exp\{ik(x - vt)\} \text{ and } u_j = \sum_{m=1}^{4} C_m u_{j,m} \tag{2.6}$$

$$\Phi_m = \alpha_{4,\mathrm{m}} \exp\{ikb_m z\} \exp\{ik(x - vt)\} \text{ and } \Phi = \sum_{m=1}^{4} C_m \Phi_m, \tag{2.7}$$

with the amplitude of the partial waves $\alpha_{j,m}$ and $\alpha_{4,\mathrm{m}}$. The characteristic parameter b_m is complex-valued and describes the amplitude and phase variation with the depth $z < 0$ in the substrate [2, 25]. Here v is the phase velocity and k the wavevector. The partial waves travel in the x-direction. We insert these general solutions into equations 2.4 and 2.5 and solve the linear equation system in order to extract the complex valued b_m and amplitudes of the partial waves. As one of the main characteristics of a SAW is it's localization at the interface, we consider only solutions with vanishing displacement amplitude and potential in the bulk ($u_{i,m}/\Phi_m(z \to -\infty) = 0$) [2]. In order to determine the relative amplitude of the partial waves C_m we use boundary conditions at the interface between vacuum and solid at $z = 0$. The mechanical boundary conditions require of the z-components of the stress $\sigma_{j,z=0} = 0$ at the surface of the substrate. Depending on the choice of the electric boundary condition we can distinguish free and metallized SAWs, where the velocities of the two differ for a piezoelectric solid. The velocity difference is a measure of the coupling between SAW and electric perturbations at the interface [2]. (i) The free-surface case with $D_z = \varepsilon_0 k\Phi = 0$ at $z = 0$. (ii) The metallized case with $\Phi = 0$ at $z = 0$ [2]. We determine the SAW displacement and electric potential and velocities v_{free} and v_{metal} depending on the choice of the electric boundary condition by solving a system of linear equations of these boundary conditions.
In reality these calculations for the an-isotopic are not analytically solvable and we describe the technicalities in appendix A.1. We implement this procedure for the anisotropic case in Python.

Isotropic SAW solution. The compliance tensor $\mathbf{C}$ is intimately linked to the properties of the solid, e.g. crystalline symmetry, etc. For the isotropic case non-vanishing components $\mathbf{C}_{ijkl}$

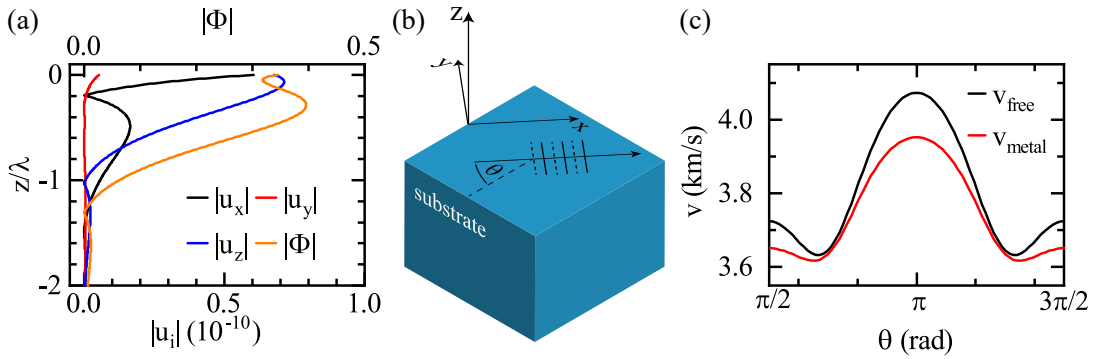

Figure 2.1.2: (a) Absolute value of the displacements $|u_i|$ and potential $|\Phi|$ for a Rayleigh SAW on the anisotropic and piezoelectric 128°-Y-X cut LNO for different penetration depths z/λ.(b) Illustration of the SAW propagation in x-direction, where the angle between a reference axis in the crystal and the propagation direction is given as θ. (c) SAW velocity on the 128°-Y-X cut LNO for the free v_{free} and metal v_{metal} boundary conditions for different propagation directions θ determined with the Finite Element simulations.

are found on the diagonal, which allows to simplify the SAW problem and allows for a analytical solution. The SAW velocity v of the Rayleigh mode is given by

$$\left(2 - \frac{v^2}{v_t^2}\right)^2 = 4\sqrt{1 - \frac{v^2}{v_t^2}}\sqrt{1 - \frac{v^2}{v_l^2}} \tag{2.8}$$

with v_l the longitudinal wave velocity and v_t the transversal wave velocity of the substrate [2]. In Fig. 2.1.1 (a) we illustrate the Rayleigh SAW on an isotropic substrate. This Rayleigh SAW is translational invariant along the y-direction, i.e. a straight crested wave, and the SAW only propagates in the x-z plane, which is known as the sagittal plane [28]. The motion of a single particle in the sagittal plane describes an ellipse. The direction of this elliptical motion changes from retro-grade closer to the surface to a pro-grade motion deeper and decreases exponentially in the substrate [2].

Anisotropic SAW solution. For anisotropic materials, the solution of (2.4)-(2.5) becomes more complex to an extend that solving the equations numerically is preferred. In detail, we use the Python code in App. A.1 to solve the propagation of a SAW on the piezoelectric and anisotropic medium 128°-Y-X cut lithium niobate (LNO), which is a commonly used SAW material [2]. We plot the magnitude of the displacements u_i and the electric potential Φ in Fig. 2.1.2 (a) for different depths z/λ in the substrate. One clear difference to the isotropic case is that $|u_y| \neq 0$ and therefore the displacement is not limited to the sagittal plane. Note that $|\Phi|$ and $|u_i|$ decrease exponentially in the bulk.
In the metal case for v_{metal} the ideal metal on the surface shorts the electric field's parallel component at the surface [2]. The transduction of an electric signal to a SAW is fabricated in practice with an interdigitated transducer (IDT), which is a thin metal film. For SAWs on a piezoelectric solid a piezoelectric coupling between an electric field and the SAW is therefore

given by

$$\frac{\Delta v}{v} = \frac{v_{\text{free}} - v_{\text{metal}}}{v_{\text{free}}},\ \varepsilon_\infty = \varepsilon_0 + \sqrt{\varepsilon_{xx}\varepsilon_{zz} - (\varepsilon_{xz})^2} \tag{2.9}$$

with v_{free} and v_{metal} for the different boundary conditions. ε_∞ is Ingebrigtsen's approximation for the dielectric constant when a piezoelectric Rayleigh wave is present [29]. For the anisotropic substrate the SAW velocity depends on the propagation direction θ with respect to the plane of the substrate material (see Fig. 2.1.2 (b)). For the Rayleigh SAW on 128°-Y-X cut LNO we plot the propagation speed of v_{free} and v_{metal} as function of θ as determined with finite element simulations in Fig. 2.1.2 (c). As evident is Fig. 2.1.2 (c) the velocity depends on θ values. We define a diffraction parameter

$$\frac{d\gamma}{d\theta} = \frac{1}{v_{\text{free}}}\frac{d^2 v_{\text{free}}}{d\theta^2} \tag{2.10}$$

from this θ dependence, which describes the divergence of a SAW packet in a solid. When $d\gamma/d\theta = -1$ the packet does not diverge [2]. The γ is the beam-steering parameter, which describes the deviation between wave vector direction and the power flow of a SAW packet. These parameters, that are a results of the anisotropy and piezoelectric effect are important for the SAW resonator performance and we discuss these effects later (see sec. 2.6).

2.2 SAWs in Multi-Layer Substrates

Now that we understand the normal case of SAWs on a single solid with free and metal boundary conditions we want discuss the case for a multi-layer system as illustrated in fig. 2.2.2 (a). On top of the substrate (Si for instance) is a thin layer with thickness h of a different material. The calculation of the SAWs propagating on multi-layer material-systems is more involved compared to a homogeneous case as each layer comes with its individual mechanical properties and hence propagation velocities. There are different ways to calculate the SAW properties on multi-layer substrates. First, there is the partial waves method, that is discussed in detail in Ref.[25]. Second, one can employ the the transfer-matrix method (see Ref.[30]).
A third option is to rely on finite-element simulations, that will be described later, in order to extract the parameters [31]. For these multi-layer systems one can in general distinguish two different cases. In the first case, the transversal velocity of the layer is larger than that of the substrate, i.e. $v_{\text{t,layer}} > v_{\text{t,substrate}}$. Conversely, the other case describes the situation, where $v_{\text{t,layer}} < v_{\text{t,substrate}}$.

Case I: $v_{\text{t,layer}} > v_{\text{t,substrate}}$. An example for this case is a Si layer with thickness h on the piezoelectric substrate ZnO, because $v_{\text{t,Si}} > v_{\text{t,ZnO}}$. [2, 25]. We plot the phase velocities for this case for different kh values in Fig. 2.2.1. Here k is the wave vector of the SAW. The product $kh = 2\pi h/\lambda$ is a measure of the height of the layer in regards to the wavelength and two SAWs on multi-layers with the same kh product have the same physical properties.
For this case the SAW velocity of the system approaches the Rayleigh velocity of the ZnO for small kh values. The Rayleigh wave velocity increases for larger kh values until it reaches the shear velocity of the Si layer $v_{\text{shear,Si}}$ at a cutoff kh value, where the Rayleigh mode vanishes and there is no SAW mode left. We now understand the general behaviour of a SAW on a multi-layer

for the case $v_{\text{t,layer}} > v_{\text{t,substrate}}$ for different SAW penetration depths in comparison to the height of the layer h.

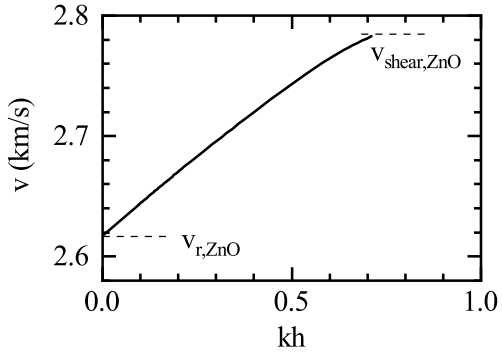

Figure 2.2.1: (a) Velocities with the free boundary condition v_{free} of the Rayleigh mode on a Si-ZnO multi-layer substrate for different values of kh with h the height of the Si layer that we determine with the simulations described in sec. 2.3.

Case II: $v_{\text{t,layer}} < v_{\text{t,substrate}}$. An example for this other case is a piezoelectric LNO layer with thickness h on the substrate Si, because $v_{\text{t,LNO}} < v_{\text{t,Si}}$. We plot the phase velocities for

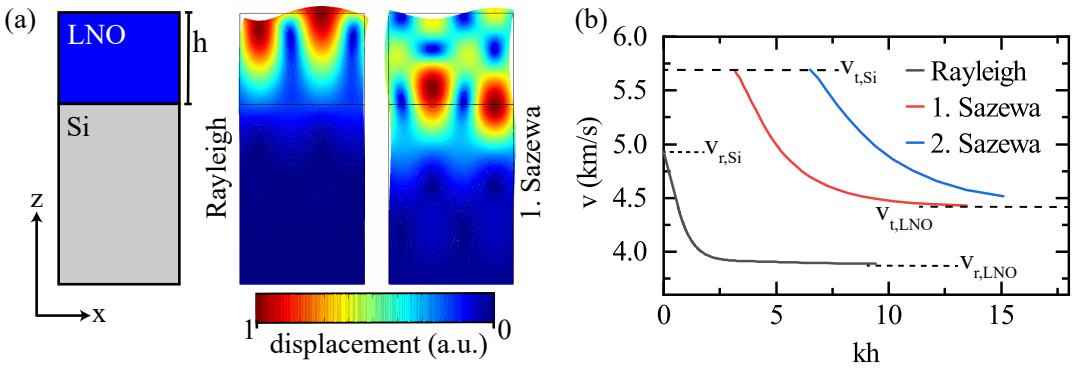

Figure 2.2.2: (a) Illustration of the layer-stack and the displacement of the Rayleigh and Sazewa modes for the Rayleigh and Sazewa mode from the simulation. (b) Velocities with the free boundary condition v_{free} of the Rayleigh and first two Sazewa modes on the LNO-Si multi-layer substrate for different values of kh with h the height of the LNO layer that we determine with the simulations described in sec. 2.3.

this case for different kh values in Fig. 2.2.2 (b) for the multi-layer system illustrated in (a) - LNO on Si. Here the Rayleigh mode SAW velocity is close to the Si Rayleigh velocity $v_{\text{R,Si}}$ for small kh values, because for small wave vectors k the wavelength $\lambda \gg h$ and the SAW travels propagates mainly in Si. The velocity of the Rayleigh mode converges to the layer/LNO SAW velocity $v_{\text{r,LNO}}$ for large values of kh, because for large wave vectors k the wavelength $\lambda \ll h$ and the SAW travels mostly in the LNO. At higher values of kh higher SAW modes,

that are called Sazewa modes, appear. These start of with the transversal substrate velocity $v_{\text{t,Si}}$ and then decrease to the transversal velocity $v_{\text{t,LNO}}$ of the layer for higher values of kh. From the finite element simulations we can determine the displacements in the substrate for the Rayleigh and 1. Sazewa mode in Fig. 2.2.2 (a). We now understand the general behaviour of a SAW on a multi-layer for the case $v_{\text{t,layer}} < v_{\text{t,substrate}}$ for different SAW penetration depths, which deviates substantially from the other case. With the multi-layer substrate the SAWs are no longer dispersion-free, because the phase velocity is a function of kh [2].

2.3 Finite Element Simulations

For the simulations we employ Finite Element modeling to compute the SAW properties using COMSOL Multiphysics, a commercially available software package [32]. We illustrate the multi-layer stack of which we want to find the eigenfrequencies in Fig. 2.3.1 (b). We restrict the simulation to a two dimensional study in the saggital plane of the stack. The materials for the substrate and layer are in general piezoelectric and anisotropic.
As the relative orientation for these anisotropic materials is relevant with respect to the propagation properties of the SAW, we define Euler angles, so that we can relate the spatial coordinates of the crystal lattice X,Y,Z to the laboratory frame used for the spatial propagation of the SAW [2]. These coordinate systems are linked by the three Euler angles, corresponding to three consecutive rotations of the coordinate system. The first angle α defines an anticlockwise rotation around the axis z. Second, an anticlockwise rotation by the angle μ is performed around the new x' axis resulting from the last rotation. The final rotation is around the twice-rotated z'' axis with the angle ν [2]. We illustrate these rotations in Fig. 2.3.1 (a). We note, that the order of rotations as specified in the Finite Element software is reversed, because the software defines the orientation of the crystal with respect to the device [33]. Standards for cutting wafers from a crystal however, specify the orientation of the wafer with respect to the crystal [33].
Careful selection of the simulation volume and the appropriate boundary conditions (BCs) is essential in order to generate valid simulation results. The geometry, that we simulate, consists of a layer with height h on top of a substrate. The entire stack has the width b and BCs are applied to the edges. We illustrate the simulated geometry along with the BCs in Fig. 2.3.1 (b): We apply periodic Floquet boundary conditions to the magenta colored edges of the stack and thereby only allow for waves with a wavelength, that is equal to the width of the stack $n \cdot \lambda = b$ with $n \in \mathbb{N}$ (or multiples thereof) [31]. The height of the entire stack for the simulation must be at least a few times the width b, because the SAW penetration into the material is on the order of the wavelength [2]. The system is charge free for the simulation, which satisfies the BC $\boldsymbol{\nabla} \cdot \vec{D} = 0$ from Section 2.1. The mechanical BCs $\sigma_{i,z} = 0$ at the surface and $\sigma_{i,z}$ continuous across the interface is satisfied for the simulation [25]. For the electric BC (light blue) on top of the layer-stack we choose either a zero charges or ground boundary condition for v_{free} or v_{metal} respectively. The BCs specified up to now allow some bulk acoustic waves (BAWs) in addition to the SAWs. In Fig. 2.3.1 (c) we plot one SAW mode shape (displacement profile) on the left and a BAW mode shape on the right. In case of a BAW there is displacement at the bottom of the simulated stack compared to the absence of displacement in case of a SAW. We can make use of this observation to distinguish between a BAW and a SAW by introducing an additional

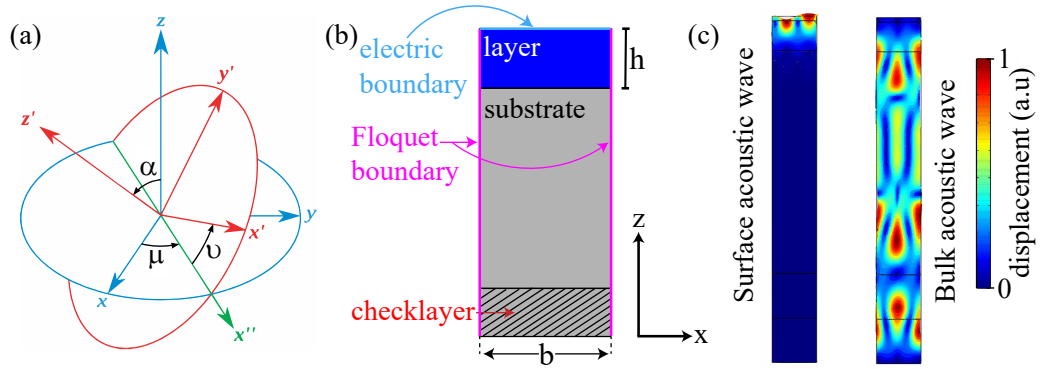

Figure 2.3.1: (a) Euler angles in the Z-X-Z notation with the angles α, μ, ν adapted from [34]. (b) Illustration of the layer stack used to simulate the SAW modes with the Finite Element method. (c) Resulting modes with a SAW mode on the left and for comparison a bulk acoustic wave (BAW) on the right.

layer, here called "checklayer" at the bottom of the stack with the same material properties as the substrate above. This allows to determine the fraction of acoustic energy in this checklayer compared to the total acoustic energy in the stack and sort out all modes that are over a threshold of $\sim 10^{-3}$ [31]. We calculate the velocity of the respective wave using (2.24) based on the eigenfrequency and perform two different studies in the simulations. First, we can vary the propagation direction on the material θ and sweep different directions, which we adjust with the appropriate Euler angles α, μ and ν. The second study involves varying the width b of the stack and thereby the wavelength of the simulated wave in order to determine the SAW velocity for different wavelengths λ and wave vectors $|k| = 2\pi/\lambda$. More insight into these Eigenfrequency simulations can be found in Ref.[31].

2.4 Fit Model for Surface Acoustic Wave Resonators

In Ref.[19], the authors derive a theoretical model for the complex microwave reflection parameter S_{11} of a SAW resonator starting from an RLC-circuit equivalent model. We show in Appendix A.2 that this model can be recast into the standard formula for the scattering parameter of a superconducting microwave resonator in reflection-type measurement [35, 36]. The full equation that is used to describe resonators in the reflection-type measurement is

$$S_{11}(f) = \underbrace{Ae^{i\phi_\mathrm{f}}e^{-2\pi i f\tau}}_{\text{environment}}\left(1 - \frac{2\frac{Q}{Q_\mathrm{e}}e^{i\theta_\mathrm{f}}}{1 + 2iQ\frac{\delta f_\mathrm{r}}{f}}\right), \tag{2.11}$$

where f is the frequency, $\delta f_\mathrm{r} = f - f_\mathrm{r}$ with f_r is the resonance frequency, Q_e the external quality factor that quantifies the coupling to the readout-circuitry, while Q_i quantifies internal losses due to for example two-level systems. Q is the loaded quality factor which is given by $Q^{-1} = Q_\mathrm{i}^{-1} + Q_\mathrm{e}^{-1}$.
We follow the approach from Ref.[37] and allow a complex value for the external quality factor

$Q_e = |Q_e|e^{i\theta_f}$ in order to deal with impedance mismatch quantified by θ_f, which works well for superconducting microwave resonators. However, for convenience we simplify our notation and write $Q_e = |Q_e|$ if not specified otherwise. We include a term $Ae^{i\phi_f}$ to deal with cable loss and amplification in our measurement. The phase ϕ_f rotates the circle, that a resonance signatures describes, in the complex plane. The term $e^{-2\pi i f\tau}$ accounts for the phase change proportional to the frequency, that is attributed to cable delay. In Fig. 2.4.1 (a) a typical resonance signature

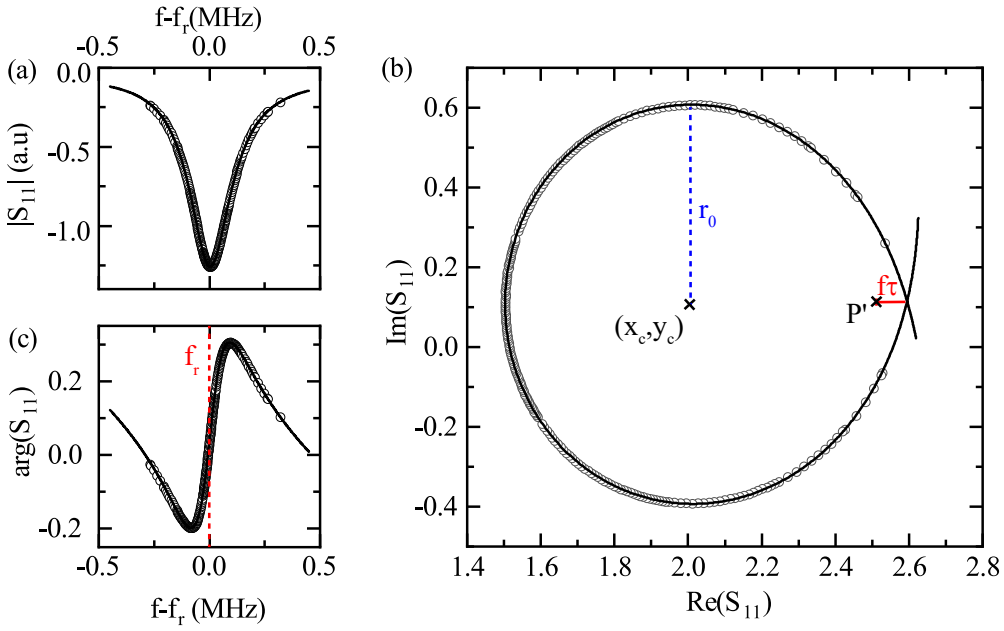

Figure 2.4.1: The complex reflection parameter S_{11} in the vicinity of the resonance allows to determine important figures of merit of the resonance with the circlefit. (a) Absolute value $|S_{11}|$ in the vicinity of the resonance showing a Lorentzian dip profile. (b) Visualized in the complex plain, S_{11} describes a circle with radius r_0 with a shift in the complex plane to the centre (x_c, y_c). (c) Phase $\arg(S_{11})$ in the vicinity of the resonance. The fits to equation 2.11 are performed in the complex plain with the circle-fit algorithm.

of a SAW resonator is shown. It would be possible to fit a Lorentzian to this resonance, but this approach would discard the phase information naturally included in the complex scattering parameter S_{11}. By considering this phase information we can improve the accuracy of the fit [36]. We will only briefly introduce process of the 'circle-fit' algorithm and refer the reader to Ref.[36] for a comprehensive description. In Fig. 2.4.1 (b) we plot the complex valued scattering parameter in the complex plane. In the complex plane a resonance signature corresponds to a circle with radius r_0 and a translation of the center to (x_c, y_c), because of cross talk between cables or coupling structures [38]. There is an additional complex phase shift that rotates the circle in the complex plane because the coupling port of the resonator does not necessarily coincide with the the plane of the measurement [38]. An algebraic fit to the circle in the complex plane yields the diameter d of the circle and the translation (x_c, y_c). The diameter corresponds

to the quality factors $d = 2Q/Q_e$ [36].
An important part of this circle-fit algorithm is the calibration of the data in the complex plane to determine the environment terms. First we fit a linear function to the outer-most data points of the phase in Fig. 2.4.1 (c) and make a guess for the cable delay τ that twists the resonance circle into a loop in Fig. 2.4.1 (b) [36]. In a non-linear least squares algorithm the deviation from the ideal circular shape is minimized to determine τ [36]. The off resonant point, i.e. the point of the signature for $\delta f \to \infty$, is P' (see Fig. 2.4.1 (b)). For the ideal signature of a resonance without the environmental factors this off-resonant point $P = 1$. Therefore the environmental factors can be calculated from the difference between P' and P, but the resonance frequency f_r is needed to determine P'. The resonance frequency f_r can be extracted from the phase vs. frequency data in Fig. 2.4.1 (c) with the formula

$$\arg(S_{11}) = \theta_0 + 2\arctan\left[2Q_e(1 - \frac{f}{f_r})\right]. \tag{2.12}$$

With f_r and the translation of the circle with the radius we determine P' and thereby $A = |P'|$ and $\phi_f = \arg(P')$ [36]. This calibration of the microwave background is also known as diameter-correction method.
It is to be noted that some challenges appear due to the fact that we perform reflection measurements with a circulator instead of the usual transmission measurements with a hanger-type resonator (see Section 3.3). First, the diameter-correction method employed in the circlefit is associated with an error, because of the finite isolation of the circulator, and therefore usually a full calibration of the scattering parameter is necessary [39, 40]. The errors however only affect the separation of Q_i and Q_e from Q and the error ΔQ_i decreases with decreasing Q_i/Q_e. We therefore assume the deviations to be small and not critical to the quantitative analysis of our experiments. Moreover, improvements to the circle fit routine have been proposed recently in Ref.[40] and can be implemented in the future to improve the accuracy of the analysis further. We use the Qkit[1] implementation of the circle fit algorithm [41].

2.5 Surface Acoustic Wave Resonator Building Blocks

The main requirement for a SAW resonator is an efficient reflector for SAWs [2]. In the case of two reflectors, those impose boundary conditions on the propagating SAW between them which results in a standing SAW pattern in this region. For SAW devices one typically uses a Bragg-reflector, which consists of a grating of of many reflective electrodes resulting in a collective constructive reflection of the wave for specific frequencies/wavelength which is discussed in more detail in Subsec. 2.5.1. In order to excite a SAW inside the resonator one needs an additional element which transducers the microwave to an acoustic signal and vice versa. This is usually performed with an interdigitated transducer (IDT) which we discuss in Subsec. 2.5.2.

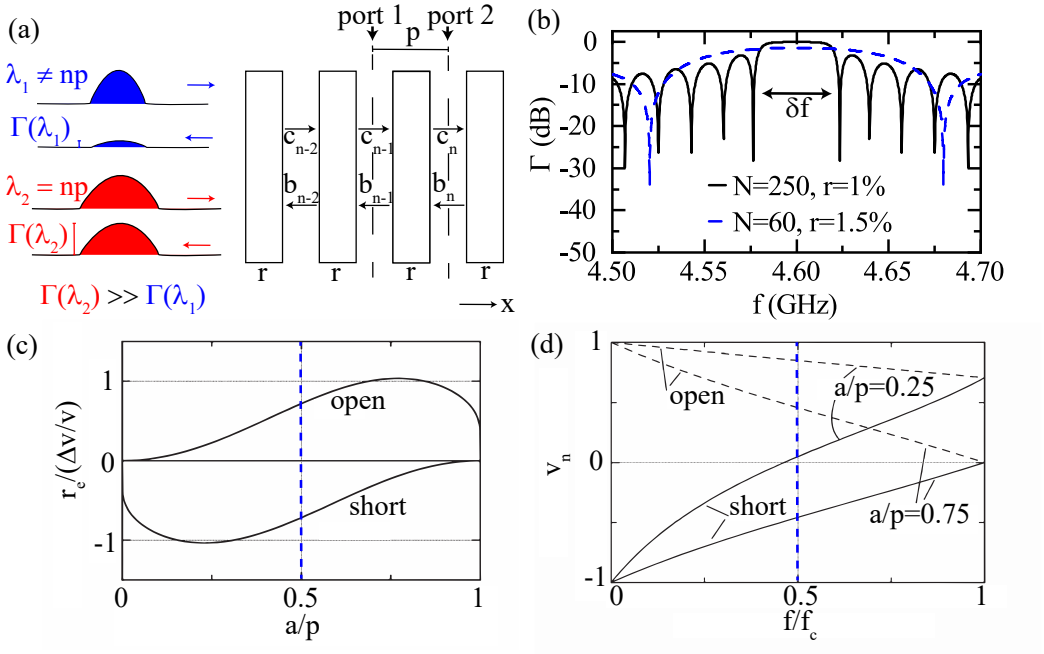

Figure 2.5.1: (a) RAM analysis of an infinite array of strips with pitch p. SAWs with the wavelength of multiples of p with $n \in \mathbb{N}$ are strongly reflected by this Bragg-mirror, while SAWs with a wavelength unequal to multiples of p are not. (b) Reflection coefficient Γ in a logarithmic plot in the vicinity of the centre frequency $f_c = 4.6\,\mathrm{GHz}$ for two different arrays. (c) Electrical contribution to the single grating reflectivity r_e for open and shorted electrodes and different values of a/p. (d) The normalized velocity $v_n = (v_e - v_{metal})/(v_{free} - v_{metal})$ that varies through electrical loading for open and shorted electrodes. Panels (c) and (d) are adapted from Ref. [2].

2.5.1 Reflective gratings

For en efficient reflector of SAWs an array of electrodes, with reflectivity r each, form a Bragg mirror. Each of the electrodes reflects a fraction of the incident SAW. However, if the wavelength λ is twice the pitch electrode pitch p, these partially reflected waves interfere constructively forming a high reflective Bragg mirror for SAWs. As the high reflection of the Bragg mirrors is linked to $\lambda = 2p$ reflections only occur in a small window around this wavelength. These strips can be grooves, open circuit electrodes or shorted electrodes [2]. In order to understand the nature of the problem we will start to look at a grating with infinite length, i.e. an infinite number of electrodes (see Fig. 2.5.1 (a)).

Infinite length grating. We consider the reflective array method (RAM) that is described in detail in Ref. [2]. The RAM approach considers wave scattering by individual electrodes as illustrated in Fig. 2.5.1 (a). Here, c_n and b_n are the amplitudes of waves traveling to the right and left respectively. The electrodes have a transmission coefficient t and a reflection coefficient r_1 for waves incident from the left and r_2 for waves incident from the right. In our case we assume that $r_1 = r_2 = r$ holds and that the mirror is lossless $t = \sqrt{1 - r^2}$. In the style of Ref.[2] we use the P-matrix formalism, which is a scattering matrix commonly used to describe the behaviour of SAWs. A single electrode has the P-matrix components p_{ij}. Here i, j label acoustic ports, where the port 1 is on the left of the nth electrode and 2 on the right. The components p_{ij} are given as

$$p_{11} = r\exp\{-ik_\mathrm{e}p\};\ p_{12} = p_{21} = t\exp\{-ik_\mathrm{e}p\}, \tag{2.13}$$

where k_e is the wave vector [2]. The scattering by one strip can be written as

$$c_\mathrm{n} = \frac{1}{t}c_\mathrm{n\text{-}1}\exp\{-ik_\mathrm{e}p\} + \frac{r}{t}b_\mathrm{n\text{-}1};\ b_\mathrm{n} = -\frac{r}{t}c_\mathrm{n\text{-}1} + \frac{1}{t}b_\mathrm{n\text{-}1}\exp\{ik_\mathrm{e}p\}, \tag{2.14}$$

with the waves c_n and b_n as constituents of the overall wave. The grating mode solution, which is a standing wave in the electrode array, is a combination of the constituents with $c_\mathrm{n} = c_\mathrm{n\text{-}1}\exp\{-i\eta p\}$; $b_\mathrm{n} = b_\mathrm{n\text{-}1}\exp\{-i\eta p\}$ [2]. Here, η is the wavevector of the grating mode solution. Substitution into equation 2.14 yields

$$\cos(\eta p) = \frac{\cos(k_\mathrm{e}p)}{t}. \tag{2.15}$$

Under the assumption that there are no losses k_e becomes real [2]. Therefore, for most frequencies η is real with the solution $\eta = k_\mathrm{e}$. When $k_\mathrm{e}p \approx M\pi,\ M \in \mathbb{N}$ the right side is larger than unity and then η is complex. This imaginary part corresponds to a stopband. The width of the stopband is given by

$$\delta f = 2f_\mathrm{c}\frac{r}{\pi}, \tag{2.16}$$

where $f_\mathrm{c} = v/2p$ is the center frequency of the stopband for the fundamental mode (M=1) [2]. For this frequency the waves, that are reflected at the single electrodes interfere constructively and the stopband appears. In Fig. 2.5.1 (b) we sketch the stop band δf for the black solid line

[1] https://github.com/qkitgroup/qkit

reflectivity Γ.

Gratings with a finite number of elements. In real life implementations of such Bragg mirrors the number of electrodes N_g is finite. The P-matrix ansatz can still be employed for this case and an effective P-matrix P for the entire mirror can be constructed from the set of $p_{i,j}$ in (2.13) [2]. The P-Matrix element P_{11}, which refers to a wave incident from the left - and reflected from the grating, with N_g electrodes and η from the grating mode solution in (2.15) is then given as

$$P_{11} = \frac{p_{11}\sin\left(N_\mathrm{g}\eta p\right)}{\sin\left(N_\mathrm{g}\eta p\right) - p_{12}\sin\left((N_\mathrm{g}-1)\eta p\right)}, \tag{2.17}$$

where the single electrode p_{11} and p_{12} are given in (2.14). With power conservation the reflection coefficient Γ is given as

$$\frac{1}{\Gamma^2} = \frac{1}{P_{11}^2} = 1 + \left|\frac{t}{r}\right|^2 \frac{\sin\left(\eta p\right)^2}{\sin\left(N_\mathrm{g}\eta p\right)}. \tag{2.18}$$

We plot Γ in Fig. 2.5.1 (b). Here we plot Γ for $r = 1\ \%$ and $N_\mathrm{g} = 250$ as black solid line (here we plot the width of the stop band δf) and for $r = 1.5\ \%$ and $N_\mathrm{g} = 60$ as blue dashed line. For the centre of the stop-band Γ is closer to unity for the black solid line with the larger $N_\mathrm{g}r$ product, while δf is larger for the blue dashed line with the larger r. It holds, that $\Gamma \leq 1$ and at the centre of the first stop band the reflection coefficient is $\Gamma \approx \tanh\left(N_\mathrm{g}r\right)$ [2].

Single electrode reflectivity r The reflectivity of a single electrode r arises from a perturbation caused by two factors

$$r = r_\mathrm{e} + r_\mathrm{m}, \tag{2.19}$$

where r_m and r_e the mechanical and electrical loading, respectively. These contributions can be calculated with Auld's perturbation theory [2]. In Fig. 2.5.1 (c) we plot the electrical component $r_\mathrm{e}/(\Delta v/v)$ which was calculated in Ref. [42] for different metallization values a/p. For $a/p = 0.5$ the absolute value for the reflectivity from the electrical contributions is

$$|r_e| = 0.718\frac{\Delta v}{v}, \tag{2.20}$$

where the absolute value r_e the identical for open circuit and shorted electrodes [2]. The mechanical contribution r_m depends on the film thickness h and the properties of the material and orientation [43] and is given by

$$r_m = iR_M\frac{h}{\lambda}\sin\left(2\pi\frac{a}{\lambda}\right) \tag{2.21}$$

$$R_M = -\frac{2\pi\Delta v/v}{\epsilon_\infty}\left[\left(\frac{u_x}{\Phi}\right)^2(\alpha_1 + \rho v_\mathrm{free}^2) + \left(\frac{u_y}{\Phi}\right)^2(\alpha_2 + \rho v_\mathrm{free}^2) + \left(\frac{u_z}{\Phi}\right)^2\rho v_\mathrm{free}^2\right]. \tag{2.22}$$

Here, u_i/Φ are the displacements at the surface normalized by the surface potential Φ. The SAW velocity with free boundary condition v_free can be determined with the methods from Sec. 2.1. For the prototypical electrode layer aluminum $\alpha_1 = 7.8 \times 10^{10}\,\mathrm{N/m^2}$, $\alpha_2 = 2.5 \times$

$10^{10}\,\mathrm{N/m^2}$ and the density $\rho = 2695\,\mathrm{kg/m^3}$. The electrical and mechanical loading also leads to a change in the velocity of the SAW. In Fig. 2.5.1 (d) we plot the normalized velocity $v_\mathrm{n} = (v_\mathrm{e} - v_\mathrm{metal})/(v_\mathrm{free} - v_\mathrm{metal})$ for open and shorted electrodes. This velocity change is important for the SAW resonator, because the SAW velocity is reduced in the transducer and Bragg-mirror.

2.5.2 Interdigitated transducers

IDTs are the most common way to generate SAWs on a piezoelectric (PE) substrate. The basic concept can be summarized as follows: A number of periodically placed electrodes are wired in alternating polarity in order to generate a periodically alternating electrical potential. Due to the piezoelectric effect, this potential is transduced into an periodically alternating strain. SAWs are generated efficiently, when the pitch of the electrodes is twice the SAW wavelength [2, 44]. The piezoelectric effect is reciprocal, i.e. when the SAW is incident on the transducer the acoustic signal is converted to a microwave signal in the same fashion. We illustrate a typical IDT in Fig 2.5.2 (a) with regular electrodes which means that they all have the same pitch p and width a [2]. The metallization ratio $a/p = 0.5$ for this illustration. We define the polarization of an electrode with a $\hat{P}_n = 0$, when the nth electrode is connected to ground (the lower bus in the illustration) and $\hat{P}_n = 1$ when the nth electrode is connected to the signal bus (top bus in the illustration). An alternating voltage V, i.e. a microwave signal, is applied to the signal bus. For a single electrode transducer, such as we illustrate here, the electrodes have the polarizations $\hat{P} = 0, 1, 0, 1, \ldots$. The fundamental wavelength of a SAW emitted from this single electrode transducer is

$$\lambda_0 = 2p. \tag{2.23}$$

The fundamental frequency f_c, of the transducer response is given as

$$f_c = \frac{v}{\lambda_0} \tag{2.24}$$

with the wavelength λ_0 taken from (2.23) and the SAW velocity v [2]. We assume here, that the transducer electrodes are non-reflective [2]. This is not true for the single electrode transducer ($S_\mathrm{e} = 2$), because the transducer has the same spacing for the electrodes as the Bragg reflector (see Subsec. 2.5.1) and partially reflected waves at the electrodes interfere constructively. As long as the reflectivity and number of fingers N is small the analysis is approximately valid [2]. A double electrode transducer ($S_\mathrm{e} = 4$) with the polarizations $\hat{P} = 0, 0, 1, 1, 0, 0, 1, 1, \ldots$, i.e. two fingers with the spacing $p/2$ connected two the same bus followed by two electrodes connected to the other bus, is not reflecting, because the electrode spacing is $\lambda/4$ and therefore outside the stopband of the reflective array of transducer electrodes (see Subsec. 2.5.1) [2]. As the pitch of the IDT defines the fundamental frequency, single electrode transducers eventually allow for highest fundamental frequency, as they naturally are the largest structure of a given pitch p and thus are least likely to be limited by fabrication constraints [44]. Furthermore we assume that effects, that originate from the boundary of the transducers, can be ignored. Usually this affects only a small portion of the electrodes and the distortion is acceptable [2]. The response of the transducer is given by the electrostatic charge density $\rho_\mathrm{e}(x)$, which can be

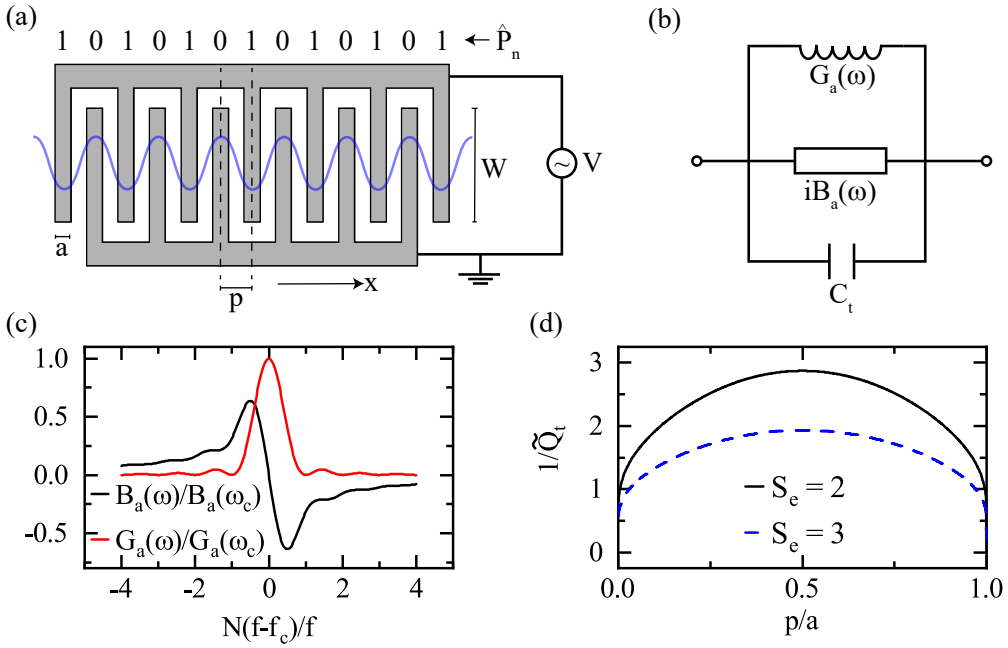

Figure 2.5.2: (a) Illustration of a uniform single electrode transducer with the element factor $S_\mathrm{e} = 2$ and $p/a = 0.5$. Neighboring fingers are connected to ground bus and signal bus in a alternating fashion. A voltage V is applied to the signal bus. (b) Equivalent circuit model of the IDT with the acoustic conductance $G_\mathrm{a}(\omega)$, susceptance $B_\mathrm{a}(\omega)$ and geometric capacitance C_t. (c) Response of the IDT in the vicinity of ω_c with the normalized acoustic conductance $G_\mathrm{a}(\omega)/G_\mathrm{a}(\omega_\mathrm{c})$ and susceptance $B_\mathrm{a}(\omega)/B_\mathrm{a}(\omega_\mathrm{c})$. (d) Inverse electrical quality factor $1/Q_\mathrm{t}$ for different metallization ratios p/a.

expressed using the array factor

$$A(x) = \sum_{n=1}^{N} \hat{P}_n \delta(x - x_n) \xrightarrow{\mathrm{FT}} \bar{A}(\beta) = \frac{\sin\left(\frac{N}{4}\beta p S_\mathrm{e}\right)}{\sin\left(\frac{1}{2}\beta p S_\mathrm{e}\right)} \begin{cases} 1 & \text{for } S_\mathrm{e} = 2, 3 \\ 2\cos\left(\beta\frac{p}{2}\right) & \text{for } S_\mathrm{e} = 4 \end{cases}, \tag{2.25}$$

with delta distributions for all the electrodes. The polarity of the nth $\hat{P}_n$ is 1 when it is connected to the signal bus and 0 for a connection to the ground bus. The electrostatic charge density is $\rho_\mathrm{e} = A(x) * \rho_\mathrm{f}(x)$, the convolution between array factor and the single electrode charge density factor ρ_f [2]. With a Fourier transform one can calculate $\bar{A}(\beta)$ with $\beta = \pi m/p$, where m is an integer value describing higher harmonics. The Fourier transform of the electrostatic charge density $\bar{\rho}_\mathrm{e}(\beta) = \bar{\rho}_\mathrm{f}(\beta)\bar{A}(\beta)$. In the fundamental pass-band with ω close to $\omega_c = 2\pi v/pS_\mathrm{e}$, with

v the SAW velocity, $G_\mathrm{a}(\omega)$ and $B_\mathrm{a}(\omega)$ can be approximated by

$$G_\mathrm{a}(\omega) = \omega W \frac{\Delta v/v}{\varepsilon_\infty} |\bar{\rho}_e(k)|^2 \approx G_\mathrm{a}(\omega_\mathrm{c}) \left(\frac{\sin X}{X}\right)^2; \tag{2.26}$$

$$B_\mathrm{a}(\omega) \approx G_\mathrm{a}(\omega_\mathrm{c}) \frac{\sin 2X - 2X}{2X^2}; \tag{2.27}$$

$$G_\mathrm{a}(\omega_\mathrm{c}) = \omega_\mathrm{c} N^2 W \frac{\Delta v}{4v} \left[\frac{2\varepsilon_\infty \sin(\pi/2)}{\mathcal{P}_{-1/2}(-\cos \pi a/p)}\right]^2, \tag{2.28}$$

where $X = \pi N(\omega - \omega_\mathrm{c})/4\omega_\mathrm{c}$ and $G_\mathrm{a}(\omega_\mathrm{c})$ depends on SAW parameters. We assume here $m = 1$, and a single electrode transducer ($S_\mathrm{e} = 2$) [2]. $\mathcal{P}_{-1/2}(-\cos \pi a/p)$ is a Legendre function [2]. We plot this response in Fig. 2.5.2 (c). One can define a mechanical quality factor as the ratio of susceptance to conductance at the centre of the band as

$$Q_\mathrm{t} = \frac{M\omega_\mathrm{c} C_\mathrm{t}}{G_\mathrm{a}(M\omega_\mathrm{c})} = \frac{2\tilde{Q}_\mathrm{t}}{N\Delta v/v}, \tag{2.29}$$

with C_t the static capacitance [2]. Here, $1/Q_\mathrm{t}$ is a measure of the SAW-transducer coupling strength. In Fig. 2.5.2 (d) we plot $1/\tilde{Q}_\mathrm{t}$ for different p/a values. The coupling is maximal for $a/p = 0.5$ and the single electrode transducer with $S_\mathrm{e} = 2$.

2.5.3 SAW resonator

Having introduced components acting as mirrors and transducers, they can be combined to form a resonator device for SAWs. Between the mirrors with separation distance L, standing SAWs form and they are excited by the application of electromagnetic waves using the IDT. We illustrate this single-port SAW resonator in Fig. 2.5.3 (a). Analogous to Subsec. 2.5.1, we assume, that $r_1 = r_2 = r$ and use the results for the grating with a finite number of electrodes N_g. We define a detuning parameter $\delta k = k - k_0$ with k_0 the wavevector at the Bragg-frequency. Assuming lossless behaviour this δk is real. It is important to determine the phase ϕ_g of the grating reflection parameter $\Gamma = |\Gamma| e^{i\phi_\mathrm{g}}$,because an incoming SAW that is reflected at the mirror picks up that phase ϕ_g. The total phase change a SAW picks up in the resonator during one oscillation $\Delta\phi$ ultimately results in a resonance condition $\Delta\phi = 2\pi n, n \in \mathbb{N}$. The phase of the grating reflection parameter ϕ_g is given by Ref.[2]

$$\tan(\phi_\mathrm{g} - \phi_\mathrm{r}) = -\frac{\delta k}{\sqrt{\left|\frac{r}{p}\right|^2 - \delta k^2}} \tanh\left(N_\mathrm{g} p \sqrt{\left|\frac{r}{p}\right|^2 - \delta k^2}\right). \tag{2.30}$$

When we insert into (2.30), that the Bragg-frequency $\delta k = 0$ and $\sqrt{|r/p|^2 - \delta k^2} = \pm r/p$ at the centre of the stop band, we get $\tan(\phi_\mathrm{g} - \phi_\mathrm{r}) = 0$. Therefore at the centre of the stop band $\phi_\mathrm{g} = \phi_\mathrm{r}$, the grating reflection coefficient Γ has the same phase as the reflection coefficient r of one electrode. Even though we did not discuss it in Subsec. 2.5.1 the phase of the reflectivity r

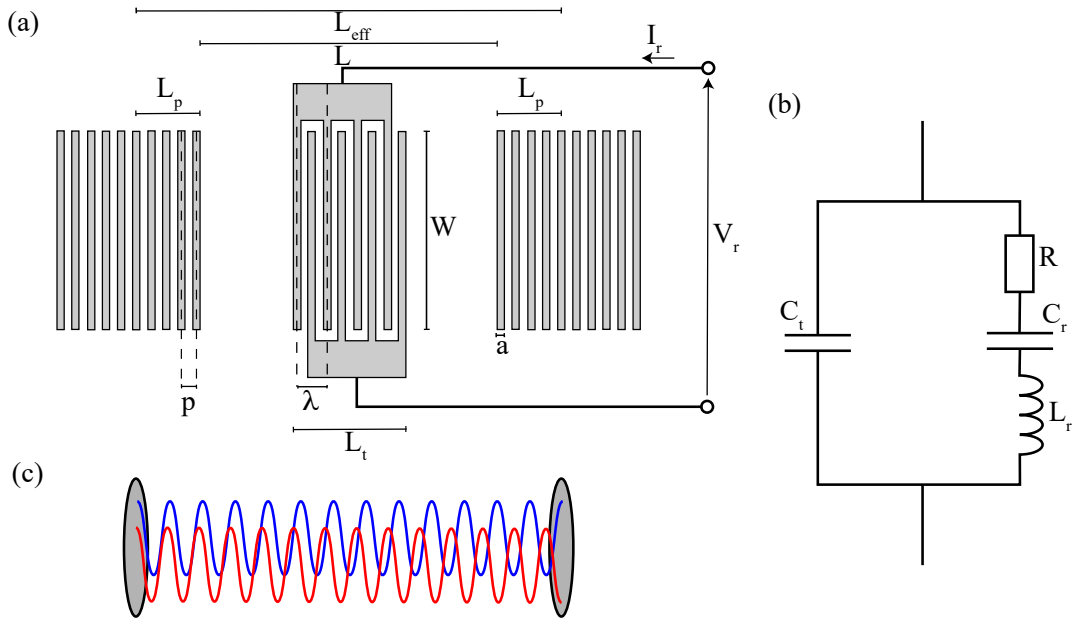

Figure 2.5.3: (a) Illustration of a single port SAW resonator made up of two Bragg-mirrors that form a cavity with a uniform single-electrode transducer in between. (b) Butterworth-van Dyke equivalent circuit model of the single port SAW resonator. (c) Fabry-Perot cavity illustration for the SAW resonator in (a) with the effective length L_{eff}.

is $\phi_{\text{r}} = \pm\pi/2$, because r is for our purposes usually imaginary.
The SAW enters the mirror in an evanescent fashion and one can define an effective reflection point at L_{P} (see Fig. 2.5.3 (a)). The length L_{P} is connected with a delay τ_{g}, which is the time that passes before a SAW packet incident on the mirror is completely reflected. The delay of the reflected wave at the Bragg frequency is given as $\tau_g = \tanh(rN_{\text{g}})/(v_{\text{free}}|r/p|)$. In the delay τ_{g} the SAW with velocity v_{free} travels in the mirror to L_{P} is reflected and travels out of the mirror. The SAW travels the distance $2L_{\text{P}}$ with velocity v_{free} in the mirror and the penetration depth is therefore $L_{\text{p}} = \tau_{\text{g}} v_{\text{free}}/2$ [2]. The result for L_{p} as a function of r and with $a/p = 1/2$ is

$$r = \frac{a}{L_{\text{p}}}. \tag{2.31}$$

The effective length of the SAW resonator is then

$$L_{\text{eff}} = L + 2L_{\text{p}}. \tag{2.32}$$

Up to now, we considered a situation, where the IDT is absent in the resonator. We next, assume a transducer inside the SAW resonator, that has no reflective properties. Double electrode transducers or a single electrode transducers with a small number of fingers N and low reflectivity r approximate this situation well.

Non-reflective transducer electrodes. For the resonator, the SAW is transduced with the IDT and travels to the right[2], where it is reflected on the right Bragg mirror and picks up the phase ϕ_g. The reflected SAW travels to the left until it is reflected at the left Bragg mirror, where it again picks up the phase ϕ_g. The SAW also picks up the phase $-2\omega L/v_{free}$ while it travels freely between the Bragg-mirrors. The total phase change is $\Delta\phi = 2\phi_g - 2\omega L/v_{free}$. One implicit assumption is, that the velocity is homogeneous/constant across the entire resonator volume, while in practice the velocity changes due to electric and mechanical loading through the mirror and transducer electrodes. A standing wave forms in the resonator, if the total phase change during one oscillation is $\Delta\phi = 2\pi n$ with $n \in \mathbb{N}$. For a given length L the resonance condition is fulfilled for wavelengths λ according to

$$L = (n \pm \frac{1}{2})\frac{\lambda}{2} \xrightarrow{\text{symmetric}} L = (2n \pm \frac{1}{2})\frac{\lambda}{2}, \tag{2.33}$$

where $\phi_g = \pm\pi/2$ has been used.The transducer is symmetric in the center between the reflectors (see Fig. 2.5.3 (a)). Both symmetric and antisymmetric standing SAWs in between the reflectors are possible, however because the transducer is symmetric only symmetric standing waves modes can be excited with the transducer. This modifies the resonance condition in (2.33). In Fig. 2.5.3 (c), we illustrate the SAW resonator as a Fabry-Perot cavity with length L_{eff}. Within this cavity standing waves form and we plot a symmetric (blue) and antisymmetric (red) standing wave between two mirrors. For Fabry-Perot cavities the free spectral range Δf_{fsr} is the frequency spacing between neighbouring modes. This free spectral range is given as

$$\Delta f_{fsr} = \frac{v_{free}}{2L_{eff}}. \tag{2.34}$$

When $\Delta f_{fsr} > \delta f$ a single resonance is in the stop-band, while for larger resonators $\Delta f_{fsr} < \delta f$ and multiple resonances appear in the stop-band [45].

Reflective transducer electrodes. When the electrodes of the transducer are reflective the SAW picks up another phase shift ϕ_t, when it passes through it. This modifies the resonance condition in (2.33) and the modified condition is

$$L = \left(2n + \frac{\phi_g + \phi_t}{\pi}\right)\frac{\lambda}{2} + L_t, \tag{2.35}$$

where $n \in \mathbb{N}$ and L_t the length of the transducer itself [2]. The phase change ϕt the SAW picks up when is passes through the transducer is $\phi t = -2\pi L_t/\lambda$. It is desirable to make the resonance frequency coincide with the frequency, where the transducer's conductance $G_a(\omega)$ (2.28) is maximal.

For a single resonance the SAW resonator can be approximated as a resonant RLC circuit, which is known as Butterworth-van Dyke model and we illustrate it in Fig. 2.5.3 (b). This RLC circuit has the inductance L_r, capacitance C_r with $w_r = \sqrt{C_r L_r}$ the resonance frequency, and the resistance R. Loss mechanisms in the resonator are included with this resistance R. This equivalent

[2]The IDT is bidirectional and we just look at one of the two cases.

circuit model is extremely useful to link the behaviour of a SAW resonator to an equivalent electric circuit picture, as this allows to model the combined response of the electromagnetic and mechanical excitation and understand it in terms of a complex scattering matrix (see Sec. 2.4).

2.6 Properties of SAW Resonators

Resonance linewidth and quality factors

Superconducting microwave resonators confine electromagnetic waves, whose excitations can be described in the particle picture by photons [35]. SAW resonators on the other hand confine acoustic waves. Their excitations are commonly described by introducing the phonon as the corresponding quasi-particle [27, 45].
The SAW cavity decay rate κ, which can also be expressed as the lifetime of phonons on resonance κ^{-1}, has two contributions. One from the input and output coupling κ_e and the other from intrinsic losses κ_i and $\kappa = \kappa_\mathrm{e} + \kappa_\mathrm{i}$ [46]. One can define the loaded quality factor Q of a resonator mode with frequency f_r as

$$Q = \frac{f_\mathrm{r} 2\pi}{\kappa}; \; \frac{1}{Q} = \frac{1}{Q_\mathrm{i}} + \frac{1}{Q_\mathrm{e}}. \tag{2.36}$$

When $\kappa_\mathrm{e} \gg \kappa_\mathrm{i}$ the cavity is 'overcoupled'. The external coupling rate is far larger than the internal loss rate of the SAW resonator. If $\kappa_\mathrm{e} = \kappa_\mathrm{i}$ the cavity is 'critically coupled' and the external coupling rate is the same as the internal loss rate. For $\kappa_\mathrm{e} \ll \kappa_\mathrm{i}$ the cavity is 'undercoupled' and the internal cavity losses dominate the total loss rate [46]. We characterize the external coupling to the SAW resonator in form of the loss rate κ_e or the quality factor $Q_\mathrm{e} = f_\mathrm{r} 2\pi/\kappa_\mathrm{i}$, which depends on the geometric parameters of the SAW resonator.

External quality factor

The external coupling rate κ_e and thereby the quality factor Q_e through the coupling of a microwave field to the single port SAW resonator is expressed in the equivalent circuit model (see Fig. 2.5.3 (b)) through the impedance L_r. The external quality factor Q_e for such a series resonator is $Q_\mathrm{e} = \omega_\mathrm{r} L_\mathrm{r}/Z_0$, where ω_r is the resonance frequency L_r the inductivity of the resonance and Z_0 the impedance at the port [47, 48]. L_r is given for a SAW resonator at the resonance frequency $L_\mathrm{r} = L_\mathrm{eff}/4 v_\mathrm{free} G_\mathrm{a}(\omega_\mathrm{r})$ [2]. Assuming that $p/a = 1/2$ and that the single electrode transducer has the acoustic conductance $G_\mathrm{a}(\omega_\mathrm{r})$ [2] the result for Q_e becomes

$$Q_\mathrm{e} = \frac{\omega_\mathrm{r} L_\mathrm{r}}{Z_0} = \frac{4 L_\mathrm{eff}}{11.48 v_\mathrm{free} Z_0 \varepsilon_\infty W \Delta v / v N^2}, \tag{2.37}$$

which contains geometric parameters of the SAW resonator that can be adjusted during the design stage (see Sec. 3.1).

Intrinsic quality factor

The intrinsic losses in the resonator can be characterized in form of a loss rate κ_i or in form of a quality factor $Q_\mathrm{i} = f_\mathrm{r} 2\pi/\kappa_\mathrm{i}$. As the intrinsic losses are connected with a microscopic loss mechanisms e.g. in the form of so-called two-level systems, Q_i and consequently κ_i can become dependent on the SAW amplitude or power applied to the resonator respectively. It is useful to state this power as the average number of excitations (phonons) in the cavity n_phonon. As long as the decay rate fulfills $\kappa/2\pi \ll \Delta f_\mathrm{fsr}$, i.e. one is considering a high-Q cavity, where the average number of phonons is given by

$$n_\mathrm{phonon} = \frac{4\kappa_\mathrm{e} P}{2\pi\hbar f_\mathrm{r}(\kappa_\mathrm{e}+\kappa_\mathrm{i})^2}. \tag{2.38}$$

Here, P is the input power in Watts incident on the IDT [46].
There are several primary sources of loss that impact Q_i of SAW resonators [49]:

- finite grating reflectivity $Q_\mathrm{i,g}$
- acoustic diffraction $Q_\mathrm{i,d}$
- material viscosity $Q_\mathrm{i,v}$
- electrode resistivity $Q_\mathrm{i,\Omega}$
- bulk wave generation $Q_\mathrm{i,bg}$

, which contribute to the total Q_i given by

$$\frac{1}{Q_\mathrm{i}} = \frac{1}{Q_\mathrm{i,g}} + \frac{1}{Q_\mathrm{i,d}} + \frac{1}{Q_\mathrm{i,\Omega}} + \frac{1}{Q_\mathrm{i,bg}} + \frac{1}{Q_\mathrm{i,v}} + \frac{1}{Q_\mathrm{i,TLS}}. \tag{2.39}$$

Therefore Q_i is limited by the contribution $Q_{\mathrm{i},\ldots}$ with the smallest quality factor. In the following, we will discuss the relevance of every single contribution to the intrinsic quality factor Q_i. We add the term $Q_\mathrm{i,TLS}$ for TLS contributions, that we discuss in more detail later in Sec. 2.7. Since we are working at mK temperature with superconducting aluminium for the electrodes the resistive contribution $Q_\mathrm{i,\Omega}$ is negligible. The SAW attenuation through the substrate's viscosity is quantified by $\Omega_\mathrm{i,v} \sim 1/f^2$. For large frequencies (as in our case) this contribution becomes important [49]. A SAW incident on the mirror can be scattered into bulk waves, which is described by $\Omega_\mathrm{i,bg}$. However the contribution is typically small for shallow reflectors $h_\mathrm{groove/electrode}/\lambda \ll 1$ with the height of the electrode or the depth of groove $h_\mathrm{groove/electrode}$ [50]. For $Q_\mathrm{i,v}$,$Q_\mathrm{i,bg}$ formulas are given in [49], however they depend on empirically determined constants. For the materials we use for our SAW resonators these constants are to the best of our knowledge presently not available and therefore we can not make any quantitative predictions. As we discussed in Sec. 2.5.3 the reflection Γ of the grating in the centre of the stop-band is smaller than unity for a grating with a finite number of fingers N_g. The limit on Q_i given by the finite reflectivity $Q_\mathrm{i,g}$ is given as

$$Q_{i,g} = \frac{\pi L_\mathrm{eff}}{\lambda_0(1-\tanh rN_g)}, \tag{2.40}$$

where r is the reflectivity of a single strip and L_{eff} the effective length of the resonator [45]. When the number of grating electrodes N_{g} is chosen sufficiently large, this loss contribution can become negligible. In order to discuss the diffraction limit $Q_{\text{i,d}}$ we need to introduce diffraction and beam steering for SAWs.

Diffraction and beam steering. The wave vector of a straight-crested wave on an anisotropic substrate is described by $k(\phi) = \omega / v_{\text{free}}(\phi)$ where ϕ is the propagation direction [2]. A wave with wavevector $k(\phi)$ can be decomposed in a wavevector k_{x} and k_{y} (see Fig. 2.6.1 (a)). For an anisotropic material the slowness curve is $1/v(\phi)$ and we illustrate it for an anisotropic material in Fig. 2.6.1 (a) [2]. Here, θ is again the angle in reference to a chosen axis in the crystal.

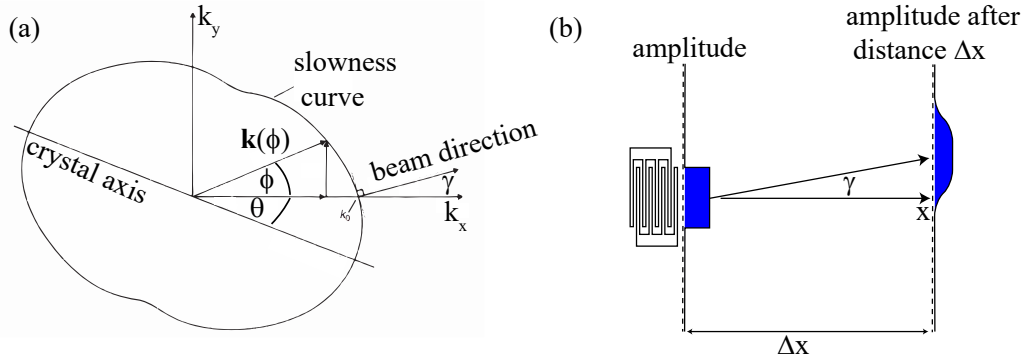

Figure 2.6.1: (a) Illustration of the slowness curve of the SAW on an anisotropic substrate. (b) Illustration of beam steering and diffraction of a SAW transduced with an IDT. Panel (a) is adapted from Ref.[2]

The x-axis is the main propagation direction normal to the electrodes of a transducer (see Fig. 2.6.1 (b)). When the wave is perturbed it contains components that propagate with the angle ϕ relative to the main propagation direction [2]. A general solution for the propagation of a wave packet launched in the x-direction can be obtained by summing over all contributions with propagation directions ϕ. In the parabolic approximation, which is valid for most materials, the k_{x} is a quadratic function of k_{y}: $k_{\text{x}}(k_{\text{y}}) \approx k_0 - a k_{\text{y}} - 1/2\, b k_{\text{y}}^2 / k_0$. This is essentially a Taylor expansion around a single point on the slowness curve. This expansion thus leads to the effective beam-steering angle γ,$a = \tan\gamma$ and the diffraction via $b = 1 + (1/v) d^2 v / d\theta^2$.
We illustrate both beam steering and diffraction of a SAW in Fig. 2.6.1 (b). The transducer, which emits a SAW packet with the amplitude along the transducer electrodes resembling a rectangular function. After the distance Δx the amplitude of the SAW is no rectangular function along the y-direction anymore, but dissolves (diffraction) and is translated with the angle γ (beam steering) [51]. The SAW packet drifts out the the reflectors of the SAW resonator through diffraction and therefore there is a limit $Q_{\text{i,d}}$ on the intrinsic quality factor through diffraction. This limit through the SAW diffraction is given as

$$Q_{\text{i,d}} = \frac{5\pi}{\left|1 + \frac{d\gamma}{d\theta}\right|} \left(\frac{W}{\lambda_0}\right)^2, \tag{2.41}$$

where W is the aperture of the resonator and $d\gamma/d\theta$ is a parameter that needs to be determined for the substrate [45]. For our resonators the W/λ is usual large, because our resonators have small wavelength λ and therefore the loss contribution through diffraction is small.

2.7 Two-Level Systems and Influence on SAW Resonator Losses

In order to extract the two-level system (TLS) contributions from our resonance signatures at different phonon numbers in the resonator and at different temperatures we derive theoretic functions for Q_i and f_r at weak and strong fields. We follow the approach described by Ref.[35] in order to link the ansatz from analogous measurements performed with superconducting microwave resonators to our SAW resonators. There are suspects for the TLS from cQED measurements, that might also be relevant for SAW resonators, i.e. tunnelling atoms and tunnelling electrons, but it is likely that for the SAW resonators other types of TLS play a significant role [52]. While of extreme importance to understand the TLS, a concrete microscopic picture is not required to model the impact of the TLS into $Q_{\mathrm{i,TLS}}$. The two-level system model (TLS) assumes a broad spectrum of tunneling states in amorphous solids. The tunneling states have elastic and electric dipole moments, which can couple to the **elastic** and **electric** fields [35].The Hamiltonian of this particle is approximated by a double well potential

$$\hat{H} = \begin{bmatrix} -\Delta & \Delta_0 \\ \Delta_0 & \Delta \end{bmatrix}. \tag{2.42}$$

, where Δ is the energy between left and right well and Δ_0 is the tunneling matrix element [35]. Diagonalization of $\hat{H}$ yields the eigenenergies $\pm\epsilon/2$ with $\epsilon = \sqrt{\Delta^2 + \Delta_0^2}$. In this new basis $\hat{H}_0 = 1/2\epsilon\hat{\sigma}_\mathrm{z}$ is the Hamiltonian with $\hat{\sigma}_i$ the Pauli matrices. Electric field $\vec{E}$ and strain field $\tilde{e}$ can interact with the TLS. The dominant effect of these external fields on the TLS is through the perturbation in Δ and not Δ_0 [35]. These interactions have the forms

$$\hat{H}^\mathrm{e}_\mathrm{int} = \left[\underbrace{\frac{\Delta}{\epsilon}\hat{\sigma}_\mathrm{z}}_{\mathrm{rel}} + \underbrace{\frac{\Delta_0}{\epsilon}\hat{\sigma}_\mathrm{x}}_{\mathrm{res}} \right] \vec{d_0} \cdot \vec{E};\ \hat{H}^\mathrm{a}_\mathrm{int} = \left[\frac{\Delta}{\epsilon}\hat{\sigma}_\mathrm{z} + \frac{\Delta_0}{\epsilon}\hat{\sigma}_\mathrm{x} \right] \zeta \cdot \tilde{e} \tag{2.43}$$

with $\hat{H}^\mathrm{e}_\mathrm{int}$ the interaction of TLS with microwave photons and $\hat{H}^\mathrm{a}_\mathrm{int}$ the interaction TLS with the phonon bath [35]. The $\hat{\sigma}_\mathrm{z}$ terms describe a relaxation response, while $\hat{\sigma}_\mathrm{x}$ term are a resonant response. The full Hamiltonians $\hat{H} = \hat{H}_0 + H^\mathrm{e/a}_\mathrm{int}$ have the form of a spin $1/2$ particle in a magnetic field. When considering relaxation processes with the T_1 longitudinal and T_2 transverse relaxation times this problem is the evolution of the spin-ensemble described by the Bloch equations. The solution to this problem is given in [35]. For the TLS in an electric field one can define an electric susceptibility tensors $\boldsymbol{\chi}_\mathrm{res}(w)$ for the resonance process and $\boldsymbol{\chi}_\mathrm{rel}(w)$ for the

relaxation process

$$\left\langle \vec{d} \right\rangle = \boldsymbol{\chi}_{\text{res}}(\omega)\vec{E};\ \left\langle \vec{d'} \right\rangle = \boldsymbol{\chi}_{\text{rel}}(\omega)\vec{E} \tag{2.44}$$
$$\boldsymbol{\chi}_{\text{res}}(\omega) = \frac{-\sigma_{\text{z}}^0}{\hbar}\left[\frac{1}{\omega_\epsilon - \omega + iT_2^{-1}} + \frac{1}{\omega_\epsilon + \omega - iT_2^{-1}}\right]$$
$$\sigma_{\text{z}}^0 = \frac{1 + (\omega_\epsilon - \omega)^2 T_2^2}{1 + \Omega^2 T_1 T_2 + (\omega_\epsilon - \omega)^2 T_2^2}\sigma_{\text{z}}^{\text{eq}}(\epsilon);\ \sigma_{\text{z}}^{\text{eq}}(\epsilon) = -\tanh\left(\frac{\epsilon}{2k_{\text{B}}T}\right).$$

Here $\omega_\epsilon = \epsilon/\hbar$ and $\Omega = 2\vec{d}\cdot\vec{E}/\hbar$ the Rabi frequency [35]. The permanent dipole moment $\vec{d'} = 2\vec{d}_0\Delta/\epsilon$ and transition dipole moment $\vec{d} = \vec{d}_0\Delta_0/\epsilon$. We want to discuss the dielectric properties under weak and strong electric fields. At microwave frequency in the GHz regime and at low temperatures $T < 1\,\text{K}$, $T_1 > 1\,\mu\text{s}$ and $\omega T_1 \gg 1$ the relaxation contribution is much smaller than then resonant contribution $\boldsymbol{\chi}_{\text{rel}}(\omega) \ll \boldsymbol{\chi}_{\text{res}}(\omega)$ [35]. For the resonant interaction the TLS contribution to the dielectric function is

$$\varepsilon_{\text{TLS}} = \iiint \left[\tilde{e}\boldsymbol{\chi}_{\text{res}}(\omega)\tilde{e}\right]\frac{\varrho_{\text{TLS}}}{\Delta_0} d\Delta d\Delta_0 d\hat{d} = \varepsilon'_{TLS} - i\varepsilon''_{TLS}, \tag{2.45}$$

where we average over the uniform distribution in Δ, log uniform in Δ_0 with ϱ_{TLS} the two level system density and over all polarisations $\hat{d}$.

Weak field

In the limit of weak fields with $\Omega^2 T_1 T_2 \ll 1$ Ref.[35] shows that the result for the imaginary and real part of the dielectric functions are

$$\frac{\varepsilon''_{\text{TLS}}(\omega)}{\epsilon} = \delta^0_{\text{TLS}}\tanh\left(\frac{\hbar\omega}{2k_{\text{B}}T}\right)$$
$$\frac{\varepsilon'_{\text{TLS}}(\omega)}{\epsilon} = -\frac{2\delta^0_{\text{TLS}}}{\pi}\left[Re\Psi\left(\frac{1}{2} - \frac{\hbar\omega}{2ik_{\text{B}}T\pi}\right) - \ln\left(\frac{\epsilon_{\text{max}}}{2\pi k_{\text{B}}T}\right)\right].$$

here Ψ is the digamma function and ϵ_{max} the maximum energy splitting of the TLS. $\delta^0_{\text{TLS}} = \pi P d_0^2/3\varepsilon$ is the TLS-induced loss tangent at zero temperature in weak field with ε the dielectric constant. When these TLS are coupled to a resonance the average effects to the frequency shift and quality factors are for a weak field

$$f_{\text{r}}(T) - f_{\text{r}}(0) = \frac{1}{Q_{\text{i,TLS}}\pi}\left[Re\Psi\left(\frac{1}{2} + \frac{hf_{\text{r}}(T)}{2\pi i k_{\text{B}}T}\right) - \log\frac{hf_r(T)}{2\pi k_{\text{B}}T}\right]f_{\text{r}}(0) \tag{2.46}$$

$$\frac{1}{Q_{\text{i}}(T)} = \frac{1}{Q_{\text{i,TLS}}}\tanh\left(\frac{hf_{\text{r}}(T)}{2k_BT}\right) + \frac{1}{Q_{\text{res}}} \tag{2.47}$$

according to [35]. Here $F\delta^0_{\text{TLS}} = \frac{1}{Q_{\text{i,TLS}}}$ with F the filling factor, which accounts for the fact that the TLS material may only partially fill the resonator volume [35].

Strong field

For strong fields one has to evaluate the full integral in (2.45) with the modified Rabi-frequency $\bar{\Omega} = 2d_0\left|\vec{E}\right|\Delta_0/\sqrt{3}\hbar\epsilon$. The power profile of the Lorentzian in $\chi_{\text{res}}(\omega)$ is widened by the factor $\kappa = \sqrt{1+\bar{\Omega}^2 T_1 T_2}$. For the loss tangent δ_{TLS} for different field strengths this means

$$\delta_{\text{TLS}} = \delta_{\text{TLS}}(\left|\vec{E}\right| = 0)\frac{1}{\sqrt{1+\left|\vec{E}/E_{\text{c}}\right|}}. \tag{2.48}$$

Here E_{c} is the critical field for the TLS saturation defined in [35]. This saturation behaviour is also given

$$\frac{1}{Q_{\text{i}}} = \frac{1}{Q_{\text{i,TLS}}}(1+\frac{n_{\text{phonon}}}{n_{\text{c}}})^{-\alpha} + \frac{1}{Q_{\text{res}}}, \tag{2.49}$$

where n_{c} is the critical phonon number for the TLS saturation with $\alpha = 1/2$ from the TLS model. Q_{res} is the contribution to Q_{i} from other sources [53]. Equations (2.49), (2.46) and (2.49) allow us to extract quality factors, that arise from TLS $Q_{\text{i,TLS}}$, from the temperature dependence of the resonance frequency f_{r} , and the phonon number and temperature dependence of Q_{i}.

Chapter 3

Methods

In order to perform systematic surveys of surface acoustic wave resonators at cryogenic temperatures and GHz frequencies careful design of not only the investigated SAW devices, but also the measurement setup is required. In this chapter we will discuss the design parameters which will allow us to control the basic properties of SAW resonators as introduced in Sec. 2.5.3, and explain the reasoning behind the design of our fabricated devices. Then we will briefly introduce the fabrication processes as well as the cryogenic microwave spectroscopy setup used to characterize the devices.

3.1 Parameter Choices

Figure 3.1.1 (a) illustrates the basic SAW resonator design used for all of the devices in this work. SAW resonator design requires careful selection of geometric parameters in order to achieve the desired operating frequency and performance. We aim for operating frequencies f_0 between 4 and $5\,\mathrm{GHz}$, for best compatibility with state-of-the-art quantum circuits [54]. Here, f_0 is given by $f_0 = \frac{v_{\mathrm{SAW}}}{\lambda_0}$, where λ_0 is the resonator modes wavelength and v_{SAW} is the phase velocity of SAWs in the respective substrate [2]. As discussed in Sec. 2.5.3, the fundamental SAW resonator wavelength λ_0 can be designed by setting the pitch p of the transducer and reflector structures. We choose $p = 0.4\,\mu\mathrm{m}$ for all investigated substrates and resonators to keep the fabrication process identical and therefore reproducible. Since v_{SAW} varies for different substrates and can be frequency dependent for multi-layer systems (see Ref. [25]), the operating frequencies of the devices are not identical, however, they are all set in the desired target range.

The metallization ratio ζ denotes the width a of a single metal electrode in relation electrode separation g. Hence, $\zeta = a/(a+g)$. We further choose a ratio of $\zeta = 0.5$ and thereby width and gap of the transducer fingers $g = a = 200\,\mathrm{nm}$. With $\zeta = 0.5$, the coupling of the transducers is maximized for a metallization ratio of $\zeta = 0.5$ [2] (see Sec. 2.5.3). For the gratings we choose the same metallization ratio $\zeta = 0.5$, because the electrical component of the reflectivity of a single grating r_{e} is identical for both shorted and open electrodes, while the deviation between the SAW velocity in- and outside of the transducer and reflector metal structure due to electrical loading is reduced [2]. In order to produce a metallization ratio of $\zeta = 0.5$ we had to calibrate our resist stacks and more details can be found in the Appendix B.

To compare the properties of SAW resonators fabricated on standard bulk LNO substrate with devices based on multi-layer substrates we identify three relevant configurations A,B and C (see Fig. 3.1.1 (c)): A bulk lithium niobate (LNO) crystal prepared in a $128°$-rotated Y-X-cut – an established material for SAW resonators [2], B a thin film lithium niobate on insulator (LNOI)

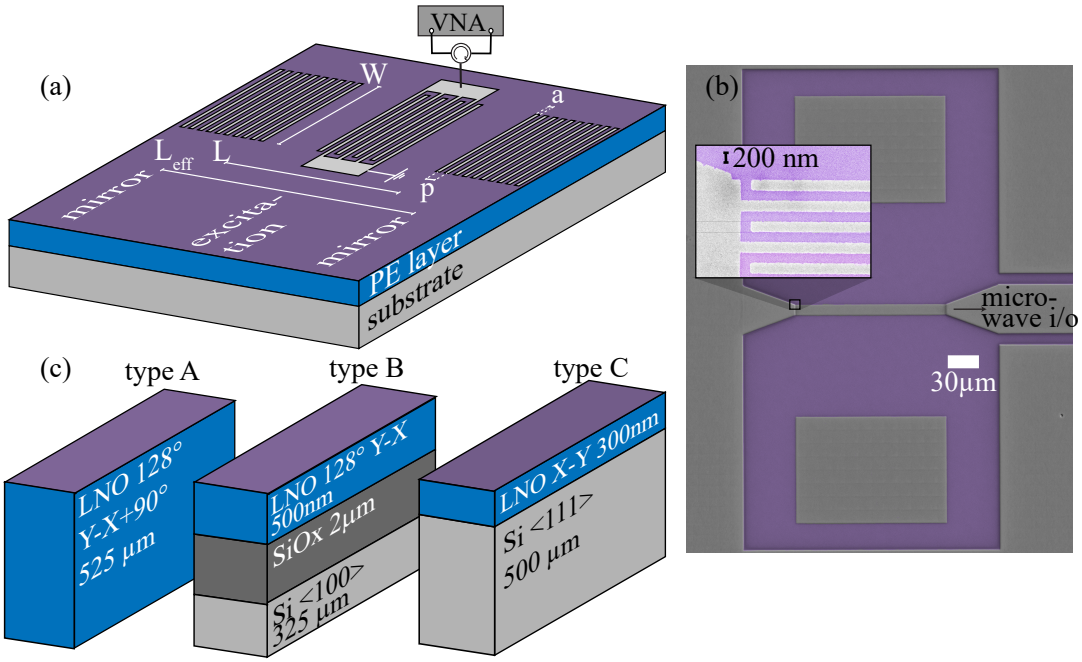

Figure 3.1.1: (a) Schematic illustration of the surface acoustic wave resonator and the measurement setup mounted inside of a commercial dilution refrigerator. (b) False color optical micrograph of a SAW resonator structure. Aluminum is shown as gray, while the LNO is colored violet. The inset shows a scanning electron micrograph (SEM) highlighting the individual strips of the transducer with a width of 200 nm. (c) Illustration of the material-systems A,B and C studied within the scope of this thesis.

stack with a $500\,\mathrm{nm}$ 128°-rotated Y-cut LNO thin film prepared on a $2\,\mu\mathrm{m}$ SiO_x buffer layer resting on a $350\,\mu\mathrm{m}$ Si(100) carrier, and C a $300\,\mathrm{nm}$ Y-X-cut LNO thin film prepared on a $525\,\mu\mathrm{m}$ Si(111) carrier. We choose the orientation of the SAW propagation direction on the substrate to avoid no beam steering and maximize the coupling to our resonator, while $d\gamma/d\theta$ is minimized to reduce diffraction losses and therefore increase the intrinsic quality factor of the SAW resonator (see Sec 2.6).
The number of gratings in the array should be chosen such that the losses are not dominated by the reflectivity of the Bragg-Mirrors $N_g r \gg 1$. Here, we experimentally choose $N_g = 500$ and discuss specifically for each configuration if this condition was fulfilled. The aperture W, length L_{eff}, number of transducer fingers N and piezoelectric coupling constant $\Delta v/v$ determine the external coupling of the SAW resonator to the environment. For resonators on type A with $\Delta v/v \approx 2\,\%$, W is chosen in the range of $140\,\mu\mathrm{m}$ - $406\,\mu\mathrm{m}$, L within $0.3\,\mathrm{mm}$ - $0.7\,\mathrm{mm}$ and N in the range of 11-31. Resonators on type C have a reduced coupling $\Delta v/v \approx 1.14 - 1.58\,\%$ and thus require larger N in the range 21-27, W is chosen within $388.5\,\mu\mathrm{m}$ - $502\,\mu\mathrm{m}$ and L in the range $0.8\,\mathrm{mm}$ - $1.2\,\mathrm{mm}$. Resonators on type B have a coupling of $\Delta v/v = 1.77 - 1.93\,\%$ and we choose more fingers 51-151[1], W in the range $110\,\mu\mathrm{m}$ - $238\,\mu\mathrm{m}$ and L in the range $0.4\,\mathrm{mm}$ - $0.8\,\mathrm{mm}$. As the external Q-factor Q_e has the following dependence on these quantities $Q_e \sim L_{\mathrm{eff}}/WN^2(\Delta v/v)$ (see Sec. 2.6). We aim to achieve critical coupling for our resonator i.e. $Q_e \approx Q_i$ for our devices.

3.2 Fabrication

Figure 3.2.1 sketches the fabrication flow of surface acoustic wave resonators. (a) We start with a cleaned substrate. (b) The substrate is coated with the positive electron beam resist CSAR 6200.09 and subsequently structured using electron beam lithography (EBL).
Important for EBL is that the charges deposited with the electron beam in the writing process are drained from the surface of the substrate to prevent charging effects. When we are dealing with an insulating substrate such as e.g. $LiNbO_3$ we spin-coat an additional layer of conductive Elektra 92 resist to reduce charging effects. However, this fabrication strategy was insufficient for the fabrication of $200\,\mathrm{nm}$ features. To mitigate blurring of the structures, we implemented proximity correction techniques [44, 55]. The software and simulation tool TRACER and BEAMER[2] by GenISys [56, 57] allows to compensate for charging by subdividing the actual design into smaller elements. Then, the optimal doses for these sub elements are computed accounting for back-scattering of electrons and charging. These sub-elements are returned in form of an updated design and exposure file which is subsequently used for the EBL patterning. In the top view in Fig. 3.2.1 (f) we indicate the exposed area in red color shades. In order to account for the proximity effect a larger dose is deposited at the edges. The same argument applies for the inner part of the structure with a lower dose. (c) The resist is developed. (d) Subsequently we evaporate a thin $20\,\mathrm{nm}$ aluminium Al film on the chip with our in-house ultra high vacuum (UHV)

[1] On hindsight, a smaller number N would have been a better choice here. However, as we have determined $\Delta v/v$ from simulations (see Sec. 4.2.1), an additional design iteration would have been required which goes beyond the timeline of this master's thesis.
[2] https://www.genisys-gmbh.com/

PLASSYS system. (e) In a lift-off process the excess aluminum that was deposited on top of the resist is removed and we get a surface acoustic wave resonator with uniform properties. We illustrate the resulting uniform Al electrode structure in Fig. 3.2.1 (g). Figure 3.1.1 (b) shows a

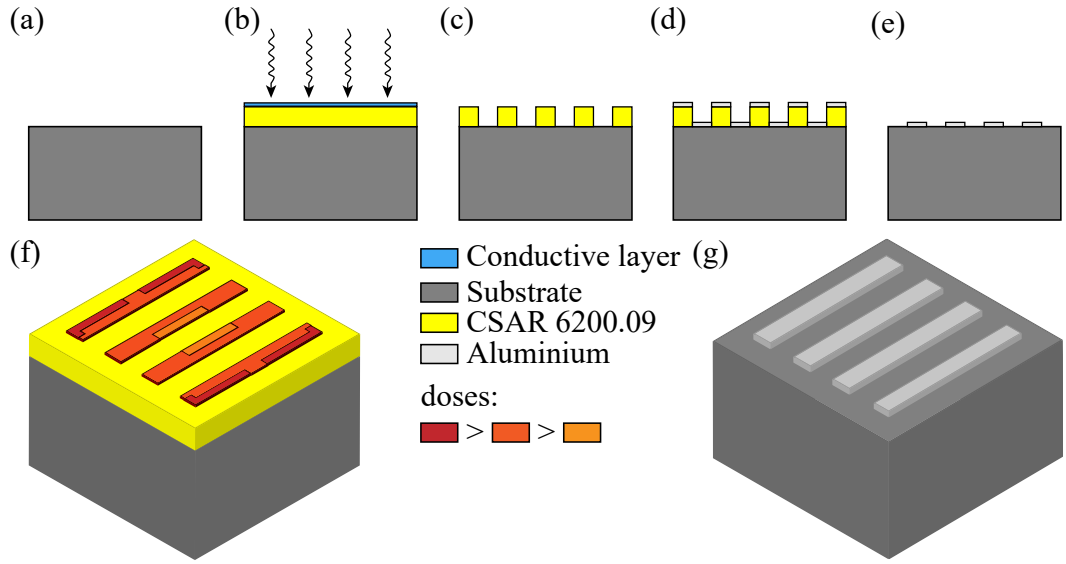

Figure 3.2.1: Schematic illustration of the fabrication steps for surface acoustic wave resonators. These steps are described in the main text.

micrograph of a resulting SAW resonator. In the insert we show a scanning electron microscope (SEM) image of the transducers structure of the resonator that shows the true scales of these structures.

3.3 Experimental Setup and Approach

The SAW resonators are investigated in a commercial dilution refrigerator with a base temperature of $T_{\text{base}} \approx 10\,\text{mK}$. This dilution refrigerator allows for temperature dependent experiments in the range from T_{base} to $900\,\text{mK}$. While the critical temperature T_c, of bulk Al is $1.19\,\text{K}$ – the critical temperature of thin film Al is typically below this value [27, 58]. Above T_c the resistance-losses in the transducers dominate the behaviour of the resonator. We measure the complex microwave reflection spectrum $S_{11}(f)$ using a vector network analyzer (VNA) [39] with the setup illustrated in Fig. 3.3.1. To thermalize the microwave lines and guarantee that we reach the single excitation limit at the device under test (DUT), we attenuate the input lines by $-66\,\text{dB}$. Using multiple cryogenic circulators, the reflected signal is routed into a non-attenuated readout-line and pre-amplified using two consecutive low-noise amplifiers at 4K and room temperature.

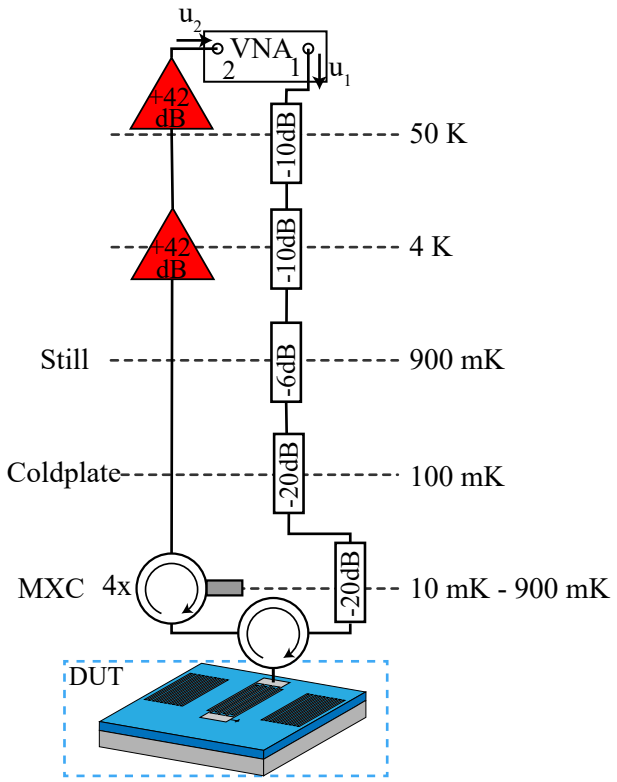

Figure 3.3.1: Schematic of the SAW resonator cryogenic measurement setup. The attenuated microwave signal reaches the device under testing (DUT) and is reflected at the SAW resonator and routed with a circulator to a non-attenuated readout-line and subsequently measured with a VNA.

The VNA measures the complex scattering parameter S_{21}

$$S_{21} = \frac{u_2}{u_1}, \tag{3.1}$$

where the voltage u_2 is sensed at port 2 and the voltage u_1 is used as a stimulus provided by port 1. As u_1 and u_2 describe oscillating voltages, they are expressed as complex values [59]. Note, that we measure our SAW resonator in reflection, which would be typically denoted as a S_{11} measurement. However, to sensitively amplify the reflected signal, we employ a circulator (a non-reciprocal microwave routing device) [60] and this practically measure a S_{21} quantity in our experiment. To avoid confusion in the later chapters of this thesis, we will label all spectra measured as described here as S_{11} to emphasize the reflection measurement performed with out DUT.

Chapter 4

Results

In this chapter, we present experimental results of the characterization of SAW resonators on the three different material systems using the methods and measurement techniques introduced in Sec. 3.3. We begin with the study of SAW resonators on bulk LNO (type A), a well established SAW substrate and compare the results to literature values on order to verify the validity of our experimental setup and measurement procedure. Using the results of this established material system as a baseline, we present and compare data on SAW resonator performance on more complex, multi-layer material-systems as LNOI (type B) and thin film LNO on silicon (type C). Lastly, we present a comprehensive comparison of data of the three material systems and attempt to provide explanations for the observed differences.

4.1 SAW Resonators on Bulk LNO

We start with material specific simulations and calculations to understand the behaviour of the SAW modes in the resonator. Based on this understanding we, analyse experimental data of four fabricated SAW resonator samples and extract material-dependent parameters such as the SAW velocity and grating reflectivity r. Subsequently, we quantify the performance of individual resonator modes, using the internal quality factor, Q_i, as our main figure of merit. Finally, the underlying loss channels of the SAW resonators are investigated for different VNA output powers and temperatures.

4.1.1 Simulations with material parameters for cryogenic temperatures

For surface acoustic wave resonators, properties of the surface acoustic wave mode in the resonator, e.g. $\Delta v/v$, v_free are important. We calculate the properties of this mode for 128°-Y cut LNO as described in Sec. 2.1 and simulate them with the Finite Element method we describe in Sec. 2.3. For these calculations, we need properties of the substrate material such as the stiffness tensor $\mathbf{C}$, piezoelectric tensor $\mathbf{e}$, density ρ and permittivity tensor $\boldsymbol{\varepsilon}$. There is extensive literature on these properties for LNO at room temperature [61, 62]. However, these properties are temperature dependent and there is to the best of our knowledge a lack of data available at cryogenic temperatures. Critically, LNO exhibits comparatively large thermal expansion coefficients, which is correlated with a strong temperature dependence for some of the mentioned material properties [63]. As such, simply assuming room temperature values is not sufficient for our study. Smith and Welsh [64] present relevant experimental data from experiments conducted

from $-20\,^{\circ}\mathrm{C}$ to $110\,^{\circ}\mathrm{C}$ and use linear interpolations for the material properties. As a first attempt, we extrapolate these material properties from this publication down to $T = 1\,\mathrm{K}$ for our simulation. Later, we will compare the results of the calculation and simulation to the experiments, but we can already say that the agreement between experiment and simulation is vastly improved with this linear extrapolation instead of the room-temperature material properties.
Using the interpolated parameters, we can now analytically calculate the relevant free c_{free} and metallized v_{metal} phase velocities for any propagation direction θ, along the crystal surface (see Fig. 4.1.1 (a)). Solutions in the direction $\tilde{\theta}$ with $\tilde{\theta} = \theta + \pi$ result in the same phase velocities as the θ direction, since waves travelling in opposite directions must have the same phase velocities due to crystal symmetry. The phase velocity shows a global maxima at $\theta = \pi, 0$ and local maxima at $\theta = \pi/2, 3\pi/2$ with large coupling $\Delta v/v$ and no beam-steering, because the phase velocities are symmetric in θ around these maxima (see theory Sec. 2.1). At these extremal points we calculate the free and metallized SAW phase velocities exactly with the methods from Sec. 2.1. As we show in Fig. 4.1.1 (a) for $\theta = 0, \pi$ there is a reasonable overlap between simulation and calculation ($\pm 8\,\mathrm{m/s}$ for the free boundary and $\pm 27\,\mathrm{m/s}$ for the metal boundary condition), however for the $\theta = \pi/2, 3\pi/2$ directions the phase velocities from the calculation are higher than for the simulation ($+44\,\mathrm{m/s}$ for the free boundary and $+87\,\mathrm{m/s}$ for the metal boundary condition). In Fig. 4.1.1 (b), we plot the diffraction parameter $d\gamma/d\theta$ from the simulation results as function of the angle between the propagation direction and a reference axis of the crystal θ. For the directions $\theta = \pi/2, 3\pi/2$ and $\theta = 0, \pi$ $d\gamma/d\theta$ is small, suggesting that beam diffraction is minimal. For our resonators we want $\gamma = 0$, in order to be free of beam-steering and $d\gamma/d\theta \approx -1$ (or as close to it as possible) for diffraction free propagation (in first order). We summarize these simulation results in Table 4.1.1. Here, we emphasize that the direction

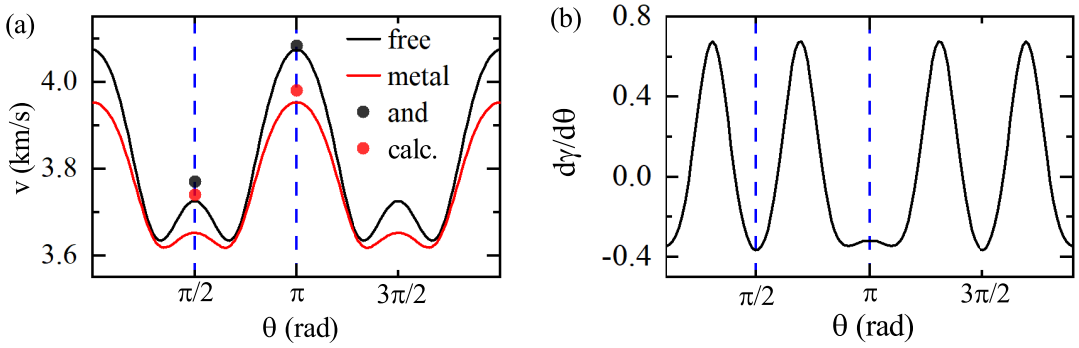

Figure 4.1.1: In (a) SAW phase velocity from simulations on bulk 128°-Y cut LNO for different propagation directions θ with free and metal electric boundary conditions. For the beam-steering free ($\gamma = 0$) propagation directions we plot results for v_{free} and v_{metal} from calculations. (b) Diffraction $d\gamma/d\theta$ of the SAW on the same material for different θ values.

$\theta = 0, \pi$ is the 128°-Y-X cut LNO frequently used for SAW devices [2]. We wall make use of these results later when we characterize the resonator performance.

Table 4.1.1: Properties of the SAWs on bulk LNO in the beam-steering free directions from the finite element simulation.

orientation (rad)	Euler angles λ, μ, θ (°)	$v_{\text{free}}(\text{km/s})$	$\Delta v/v$ (%)	γ	$d\gamma/d\theta$
0,π	0,38,0	4.073	2.37	0	-0.37
$\pi/2$, $3\pi/2$	0,38,90	3.725	1.98	0	-0.32

4.1.2 Resonator spectrum and properties

In Fig. 4.1.2 (a), we show the S_{11} spectrum of the SAW resonator (A3) fabricated on bulk LNO in green for a high output-power $P = -10\,\text{dBm}$ at the VNA corresponding to $P_{\text{in}} = -76\,\text{dBm}$ at the input of the resonator. Within the displayed frequency range the Bragg-mirrors are strongly reflecting and we can see standing wave modes confined between the two mirrors as absorption signatures in the spectrum. We mark the prominent standing wave mode in the spectrum in red at $f_{r,1}$. Panel (b) shows a zoom into this resonance and fit to (2.11). We extract the figures of merit for all of the resonances in the spectrum, for instance resonance frequency $f_{r,1} = 4.592\,\text{GHz}$, intrinsic quality factor $Q_{\text{i}} = 62.4 \times 10^3$ and external quality factor $Q_{\text{e}} = 55.3 \times 10^3$, from this particular fit.

We determine centre of the stop-band $f_{\text{c}} = 4.619\,\text{GHz}$ of the resonator by taking the average

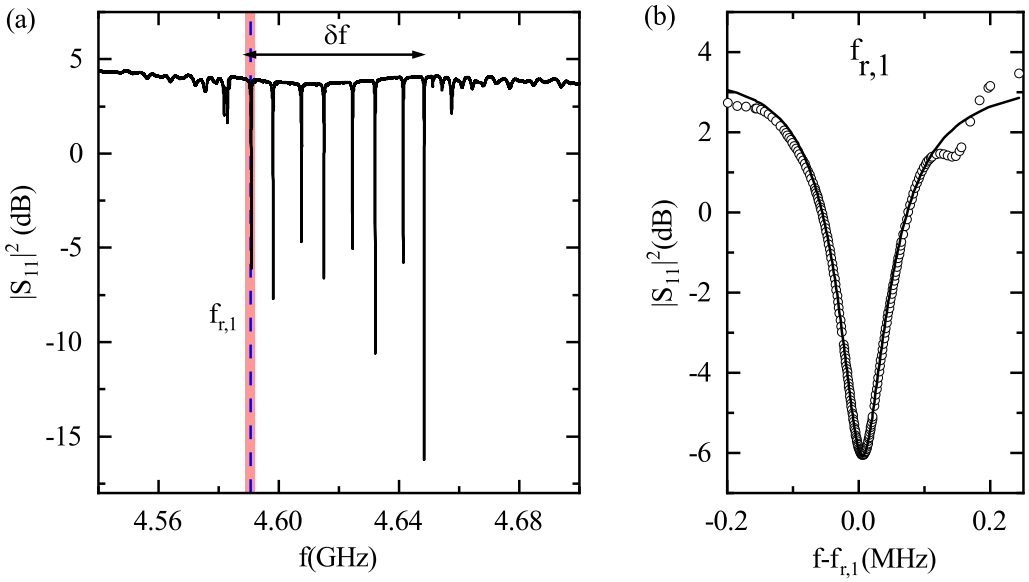

Figure 4.1.2: (a) Uncalibrated spectrum of the SAW resonator A3 from table 4.1.2 in black. The resonance at the frequency $f_{r,1}$ in the spectrum is marked with a dashed line (blue). (b) Close zoom on the resonance at the frequency $f_{r,1}$ and fit to equation 2.11

Table 4.1.2: Physical properties of the SAW resonators on bulk LNO.

device	orientation (rad)	v_{SAW} (km/s)	L_{eff} (mm)	r (%)
A1	$\pi/2$	3.681	0.724	1.6
A2	$\pi/2$	3.702	0.425	1.6
A3	$\pi/2$	3.695	0.321	1.9
A4	$\pi/2$	3.696	0.22	2.0

value of all visible resonance frequencies f_{r} of the modes in the resonator. The error Δf_{c} for the center of the stop-band is given roughly by the free-spectral-range of the resonator modes. From this parameter, we determine the SAW velocity $v_{\mathrm{SAW}} = 3695\,\mathrm{m/s}$ using the design parameter $\lambda_0 = 800\,\mathrm{nm}$ and (2.24). The resulting velocities are given in table 4.1.2 for the four different resonator structures A1-A4 with varying geometric properties. The average velocities of the four structures is $3.7\,\mathrm{km/s}$. There is good agreement of these results in comparison with the simulated SAW velocity $\pm 25\,\mathrm{m/s}$ displayed in Table 4.1.1. The velocity determined experimentally is slightly lower than the simulated values, because metal on top of the substrate (mirrors and transducer) leads to a mass loading and a reduction of the SAW velocity in these areas [2]. Our implementation of the calculations (see Sec. 2.1) is not completely in agreement with the experimental results.

From the cavity model in Sec. 2.5.3 we can determine the effective length L_{eff} of the resonators from (2.34). For the resonator A3 in particular we determine the free-spectral range $\Delta f_{\mathrm{fsr}} = 5.75\,\mathrm{MHz}$ from fits to the resonances in the spectrum in Fig. 4.1.2 (a). With (2.34) we calculate $L_{\mathrm{eff}} = 0.321\,\mathrm{mm}$ for the resonator A3, which has the length $L = 0.3\,\mathrm{mm}$. The results for the effective length for the different resonators are given in Table 4.1.2. We make use of L_{eff} and calculate the reflectivity $r = 1.87\ \%$ (for A3) of a single electrode for the different resonators with (2.31) and give the results in Table 4.1.2.

In Sec. 2.5.3 we introduced the reflectivity r of a single electrode, which is comprised of two contributions $r = r_{\mathrm{e}} + r_{\mathrm{m}}$, where r_{e} is the electric contribution and r_{m} the mechanical contribution. In the experiments we only have access to the absolute value $|r|$ of this complex quantity. When we insert the simulated$\Delta v/v$ from Sec. 4.1.1 into (2.20) we predict an electric contribution of $r_{\mathrm{e}} = 1.42\ \%$. It is more complicated to predict the mechanical contribution r_{m} using (2.22). The constants α_1,α_2 and ρ for aluminium are summarized in Sec. 2.5.3. While the free velocity v_{free} can be predicted by the simulations (see Table 4.1.1), the contributions from the shape of the SAW mode u_x/Φ, u_y/Φ and u_z/Φ require more elaborate calculations along the lines of Sec. 2.1. We do these calculations with our Python program (see Sec. 4.1.1). When we use these results to predict the mechanical contribution with (2.22) as $r_{\mathrm{m}} = (-0.2i + 0.8)$. Therefore the absolute value of the single grating reflectivity $|r| = |r_{\mathrm{e}} + r_{\mathrm{e}}| = r = 2.2\ \%$ is in good agreement with the experimental results for the four resonators in Table 4.1.2.

In Sec. 2.5.3, we introduce that the width of the stop band δf in which the mirrors are strongly reflecting is determined by the reflectivity r of the single gratings according to equation 2.16. For the resonator A3 the calculation with the values for v_{SAW} and r in table 4.1.2 predicts $\delta f = 55\,\mathrm{MHz}$. As we illustrate in Fig. 4.1.2 (a), this value is in good agreement with the

experimental results.

4.1.3 External quality factors

Fitting the complex microwave reflection data individually for the separated resonance features shown in Fig. 4.1.2 (a) using (2.11) we determine the external quality factor Q_e of individual SAW resonator modes. To obtain some statistics for the chip performance we determine the average value of external quality factor for the five center-most modes and display the resulting $\bar{Q}_e$ for each of the different resonators A1-A4 in the Tab. 4.1.3.
According to the theory introduced in Sec. 2.5.3, in particular (2.37), Q_e depends on the properties of the resonator like the effective length L_{eff}, number of transducer-fingers N and aperture W with the proportionality $Q_e \sim L_{\text{eff}}/N^2W$. In Fig. 4.1.3 we plot $\bar{Q}_e$ against the dimensionless combination of these properties for the different resonators A1-A4. The error $\Delta\bar{Q}_e$ is the standard deviation from the mean value of the five center-most modes. With the theory (2.37)

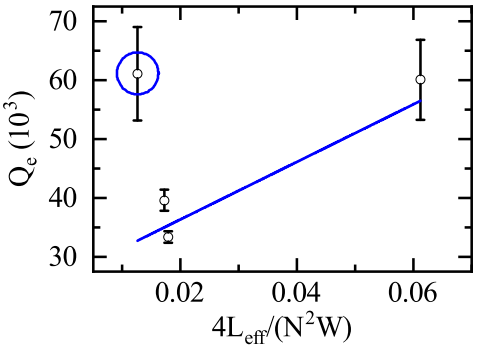

Figure 4.1.3: Mean external quality factor $\bar{Q}_e$ for the different resonators A1-A4 with the results given in Tab. 4.1.3. We visualize the expected linear dependence on L_{eff},W and $N/2$ using a fit to (4.1) (blue line) under exclusion of the outlier (blue circle).

in mind, we expect a linear dependence of Q_e as function of the dimensionless plot variable $4L_{\text{eff}}/(N^2W)$. The quality factor $Q_e \approx 35 \times 10^3$ for $4L_{\text{eff}}/(N^2W) \approx 0.017$ seems to be corroborated by the samples A3 and A4, sharing similar parameters for $4L_{\text{eff}}/(N^2W)$. In theory (2.37), Q_e should follow a linear dependence to the dimensionless factor $4L_{\text{eff}}/(N^2W)$. The other variables in (2.37), which we exclude here are the port impedance Z_0, piezoelectric coupling $\Delta v/v$, SAW velocity v_{free} and the effective dielectric constant ε_∞. All of these additional variables are strictly positive and therefore the slope of the linear function, that describes the dependence of Q_e on $4L_{\text{eff}}/(N^2W)$ must be strictly positive. The quality factor extracted for resonator A2 (blue circle) clearly deviates from this expected behaviour and if we were to include it in a linear fit the slope of the linear function would be negative. A2 has a larger number of transducer fingers $N = 31$, compared to the other devices, which yields a large total reflectivity of the transducer itself close to $50\ \%$ ($Nr = 0.5$). We suspect this leads to a more complex mode shape within the resonator and modifies the out-coupling properties of the IDT significantly. However, the reflectivity of the in- and out-coupling IDT is not accounted for in the description of the fit-model in (2.11). Therefore, we exclude this data point from further

Table 4.1.3: Mean external quality factors $\bar{Q}_\mathrm{e}$ of the four SAW resonators on bulk LNO for different values of N,W and L_eff.

device	orientation (red)	N	W (µm)	L_eff (mm)	$\bar{Q}_\mathrm{e}$ (10^3)
A1	$\pi/2$	11	391	0.724	60.1 ± 6.8
A2	$\pi/2$	31	140	0.425	61.1 ± 7.9
A3	$\pi/2$	17	258	0.321	39.6 ± 1.8
A4	$\pi/2$	11	406	0.22	33.4 ± 1.0

analysis, we fit the linear function

$$Q_\mathrm{e}\left(L_\mathrm{eff}, W, N\right) = a\frac{4L_\mathrm{eff}}{WN^2\Delta v/v} + b \tag{4.1}$$

using the remaining data point of resonator A1 in Fig. 4.1.3, where take $\Delta v/v$ from Tab. 4.1.1 and obtain $b = (27.1 \pm 5.0) \times 10^3$ and $a = (10.7 \pm 2.6) \times 10^3$. When we compare this with (2.37), the linear function for Q_e (4.1) should pass the origin, i.e. $b = 0$ and $a = 1/(11.48\varepsilon_\infty v_\mathrm{free} Z_0 \Delta v/v) = 1.5 \times 10^3$ with $Z_0 = 50\,\Omega$, $\varepsilon_\infty = 3.11 \times 10^{-11}\mathrm{F/m}$, $\Delta v/v$ from Tab. 4.1.1 and v_free from the experimental results in Tab. 4.1.2. The determined variables a and b do not fit to the theory (2.37).

4.1.4 Intrinsic quality factors

High power limit

By fitting the complex microwave reflection data individually for the resonance features in Fig. 4.1.2 (a) using (2.11) we determine the intrinsic quality factor Q_i of the individual resonator modes. As before, we compute the average value of the intrinsic quality factors of the five center-most modes at high VNA output power and summarize the results $\bar{Q}_\mathrm{i,HP} = 59.6 \times 10^3$ (resonator A3) for each of the different resonators A1-A4 in the Tab. 4.1.4. For resonator A3 the spread for Q_i is between 55.9×10^3 and 63.1×10^3 and the mean standard deviation is $\Delta Q_\mathrm{i} = 3.0 \times 10^3$.

As discussed in Sec. 2.6, any SAW resonator mode is subject to a number of different loss

Table 4.1.4: High power intrinsic quality factor contributions of the four SAW resonators on bulk LNO.

device	L_eff (mm)	W (µm)	$Q_\mathrm{i,g}$ (10^9)	r (%)	$Q_\mathrm{i,d}$ (10^6)	$\bar{Q}_{i,\mathrm{HP}}$ (10^3)
A1	0.724	391	12.7	1.6	5.9	52.8 ± 5.9
A2	0.425	140	7.4	1.6	0.76	238.4 ± 94.4
A3	0.321	258	112.5	1.9	2.6	59.6 ± 3.0
A4	0.22	406	209.6	2.0	6.4	64.1 ± 6.9

mechanisms, such as the diffraction of the SAW or the finite reflectivity of the Bragg mirrors.

All of these different loss channels are included in the experimentally observed Q_i. However, one usually finds on loss channel to be dominating and limiting Q_i. In the following, we will attempt to identify the most likely limiting contribution for the investigated bulk LNO devices: One contribution of loss for SAW resonators is diffraction – as described in Sec. 2.5.3 and, as captured by (2.41). $Q_\mathrm{i,d}$ depends on the aperture W and the diffraction coefficient $d\gamma/d\theta$. In (2.41) the intrinsic quality factor $Q_\mathrm{i,d}$ is inversely proportional to $|1 + d\gamma/d\theta|$, which vanishes when $d\gamma/d\theta = -1$. Hence, this condition is the optimum, as it describes the case of vanishing diffraction. We take $d\gamma/d\theta$ from Tab. 4.1.1, insert the aperture W for the different SAW resonators A1-A4, and calculate the contribution of the diffraction in the substrate $Q_\mathrm{i,d}$ to the intrinsic quality factor. For our resonators these expected contributions are summarized in Tab. 4.1.4. However, the impact of $Q_\mathrm{i,d}$ is orders of magnitude larger compared to than the average intrinsic quality factors we see in experiment.
The contribution from the finite reflectivity of the Bragg mirrors as described in Sec. 2.5.3 and given by (2.40) depends on the effective length L_eff of the resonator and the total reflectivity $\Gamma = \tanh(rN_g)$ of the mirror. We list the resulting contributions to Q_i in Tab. 4.1.4 and find $Q_\mathrm{i,g} \gg \bar{Q}_\mathrm{i,HP}$.
We therefore expect that these two contributions are not limiting the internal Q-factor of our SAW resonators. In order To understand this we refer to (2.41) and (2.40), where W/λ and L_eff/λ enter respectively. Due to the high frequency of the resonators the wavelength $\lambda = 800\,\mathrm{nm}$ is much smaller than the dimensions of the resonator, thus making diffraction and reflection effects negligible.
The question what limits our resonators at high power remains. It was observed that in the limit of a large reflectivity, i.e. $N_g r \gg 1$, and high frequency the resonators are limited by the phonon propagation loss of the SAWs in the substrate material [65]. Having ruled out most other contributions, we assume that the intrinisic quality factor is dominated by the propagation loss α_P according to

$$\alpha_\mathrm{P} = \frac{\pi}{\lambda \bar{Q}_\mathrm{r,HP}}. \tag{4.2}$$

The average value for the propagation loss from resonators A1,A3 and A4 is $\alpha_P = 0.0672\,\mathrm{mm}^{-1}$. From this we can calculate the average free length of a phonon traveling in the resonator before being scattered $l_\mathrm{free} = 1/\alpha_P = 14.9\,\mathrm{mm}$. Ref.[45] found $l_\mathrm{free} = 6\,\mathrm{cm}$ for SAW resonators on STX-quartz at $f = 3.1\,\mathrm{GHz}$ and cryogenic temperatures, which is considerably larger than our result. However, one should take into account that the free phonon length is frequency dependent $l_\mathrm{free} \sim f^{-3}$ [45]. Now when we take account that for our SAW resonators the center-frequency of the stopband is $1.5\times$ larger – then our free phonon propagation length should be $0.3\times$ smaller. When we take this into account our experimental result is in good agreement with Ref.[45].

Low power limit and TLS contributions

In order to examine the low power characteristics of the SAW resonators we repeatedly measure a single resonance in the resonator spectrum (cf. Fig. 4.1.2 (a)) as function of the output power of the VNA from $P_\mathrm{VNA} = -94\,\mathrm{dBm}$ to $P_\mathrm{VNA} = -4\,\mathrm{dBm}$ corresponding to $P_\mathrm{in} = -160\,\mathrm{dBm}$ and $P_\mathrm{in} = -70\,\mathrm{dBm}$ applied to the IDT. For this experiment we specifically choose one individual resonator mode, due to measurement time constraints. Specifically for the low P_in, we need

to operate the VNA with low detection bandwidths and need to acquire multiple averages to obtain an adequate signal-to-noise ratio (SNR). However, it is unlikely that the nature of loss contributions would differ significantly between two modes of roughly identical frequency and confined to the same resonator volume. If specific defects, that are resonant with the frequency of a single mode, are in fact important we would not be able to detect this. We select the resonance out of the spectrum with the highest $Q_\mathrm{i}/\Delta Q_\mathrm{i}$ obtained at high microwave powers to determine Q_i with the highest precision.
We fit the theoretical model to the complex microwave reflection data for every applied power using (2.11). In Fig. 4.1.4, we plot Q_i as function of the average number of phonons n_phonon in the resonator mode. We calculate n_phonon using (2.38), where we insert the linewidth κ, external linewidth κ_ext, resonance frequency f_r, that can be extracted from the fit to (2.11) and the microwave input power at the sample P_in. For the correct phonon number n_phonon the power at the sample P_in is important. Cable losses, that we did not take into account, can reduce the input power P_in at the sample. Therefore the phonon number n_phonon has an unspecified uncertainty Δn_phonon. We can see that Q_i of the different resonators A1-A4 in general increases with the effective length L_eff of the resonator. In the limits of very small phonon numbers (< 10) and very large phonon numbers ($> 10^6$) we can see a saturation behaviour of Q_i with increasing Q_i in between. This behaviour is well described by the TLS model described in Sec. 2.7. For large phonon numbers the TLS are saturated and the TLS contribution to the intrinsic loss rate $1/Q_\mathrm{i}$ is suppressed.The fit to the data are displayed as solid lines in Fig. 4.1.4. As evident from the plot, the model described mathematically in (2.49) describes the data extremely well (using $\alpha \approx 0.5$). From the fit, we determine the TLS contribution to the intrinsic quality factor $Q_\mathrm{i,TLS}$, critical phonon number n_c, that is a measure of when the phonons begin to saturate TLS, and the contribution to the intrinsic quality factor, that is independent of TLS contributions, Q_res. The $Q_\mathrm{i,TLS}$ of the different resonators A1-A4 are given in Tab. 4.1.5. We also list the low power saturation value $Q_{i,\mathrm{LP}}$ for the resonators in Tab. 4.1.5. As quantum circuits usually operate with power levels corresponding to single excitations, $Q_{i,\mathrm{LP}}$ is in fact the more relevant figure of merit with regard to quantum acoustic applications. The critical phonon numbers n_c for the resonators A1-A3 are spread in the interval between 21.4 and 30.3, while it is significantly higher for the resonator A4 with 159.4. Temperature sweeps are an alternative method to determine the TLS contribution $Q_\mathrm{i,TLS}$ (see Sec. 2.7) for a single mode of the resonator. We perform temperature sweeps from $10\,\mathrm{mK}$ to $600\,\mathrm{mK}$, while we measure the complex reflection parameter S_{11} in the vicinity of a single resonance for resonators A3 and A4. For each discrete temperature step, we wait $12\,\mathrm{min}$ for the sample to thermalize with the mixing chamber stage before we measure the S_{11} response close to the resonance frequency. The output power of the VNA is chosen such that $n_\mathrm{phonon} \sim 10^5$ and the mode of the SAW resonator is in the weak field limit, because the theoretical behaviour for f_r and Q_i as a function of temperature in (2.46) and (2.47) pertain only within this limit (see Sec. 2.7) [66]. Again we fit the reflection data of a single mode for all temperatures to determine f_r, Q_i and Q_e. Fig. 4.1.5 displays the temperature dependence of f_r (a) and Q_i (b) for resonator A3. Above approximately $100\,\mathrm{mK}$, the resonance frequency shifts to higher frequencies by about $6\,\mathrm{kHz}$ over the acquired temperature range. For a quantitative analysis of this data, we compare the temperature dependence with the model outlined in Sec. 2.7 (2.46) and determine the TLS contribution $Q_\mathrm{i,TLS}$ from these temperature sweeps. The fit-result $Q_\mathrm{i,TLS} = 155.6 \times 10^3$ is similar to the result from the power sweep

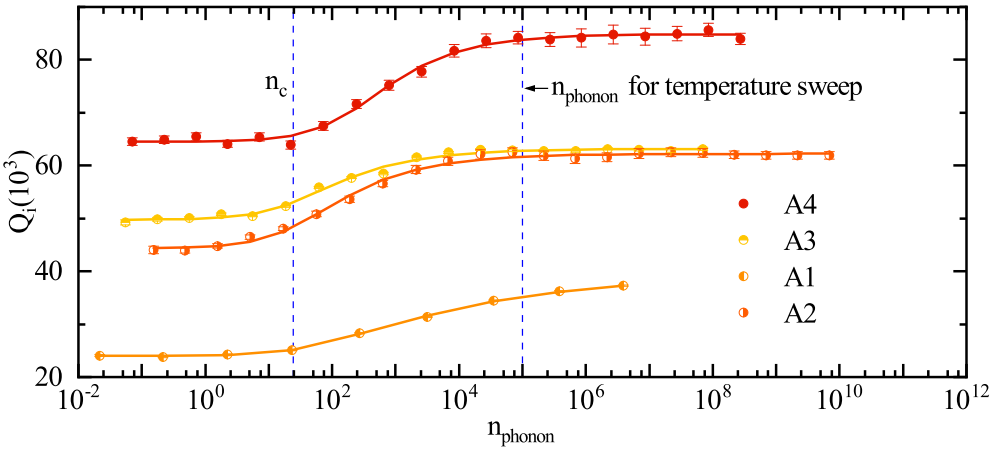

Figure 4.1.4: Intrinsic quality factor Q_i with errorbar ΔQ_i, extracted from a fit to (2.11) for one mode of each of the devices from Tab. 4.1.5 as a function of the applied microwave power (converted to phonon number in the resonator). Clear saturation behaviour for high power and low power in accordance with the TLS model is observed. The critical phonon number n_c from the fit for the resonators A1-A3 is the left blue dashed line. At higher power n_phonon we plot the phonon number, which is used for the temperature sweep with another blue dashed line.

Table 4.1.5: TLS contributions and the low power saturation limit $Q_{i,\mathrm{LP}}$ of the four SAW resonators A1-A4 on bulk LNO.

device	orientation (rad)	L_eff (mm)	$Q_\mathrm{i,TLS}$ (10^3)	$Q_\mathrm{i,LP}$ (10^3)
A1	$\pi/2$	0.724	61.2 ± 1.7	24.0 ± 0.5
A2	$\pi/2$	0.425	154.7 ± 4.3	44.4 ± 0.5
A3	$\pi/2$	0.321	234.8 ± 7.1	49.8 ± 0.5
A4	$\pi/2$	0.22	270 ± 6.8	64.6 ± 0.6

and confirms our results from before. In many cases these TLS related losses dominate the coherence of the resonators in the low power limit, which is relevant for quantum applications. The intrinsic quality factor Q_i shows almost no change over the temperature range and the fit to (2.47) does not converge. We summarize $Q_{i,\mathrm{TLS}}$ from the temperature sweeps for the two resonators in Tab. 4.1.6. The experimental results from the temperature sweep for the resonators A3 and A4 are not in complete agreement (c.f. Tab. 4.1.5). A possible explanation for this difference is that the dispersive shift $f_\mathrm{r} - f_0$ depends, unlike Q_i, also on non-resonant TLS, that are not saturated [66, 67]. The results from the temperature sweep in Tab. 4.1.6 are susceptible to more TLS losses and are therefore lower than the results from the power sweep in Tab. 4.1.5. However, they confirm the suspicion from the power sweep: These SAW resonators on bulk LNO are not limited by TLS related losses in the single phonon limit. Additionally, the TLS contribution $Q_{i,\mathrm{TLS}}$ seems to scale with the mode volume in our measurements. For a resonator

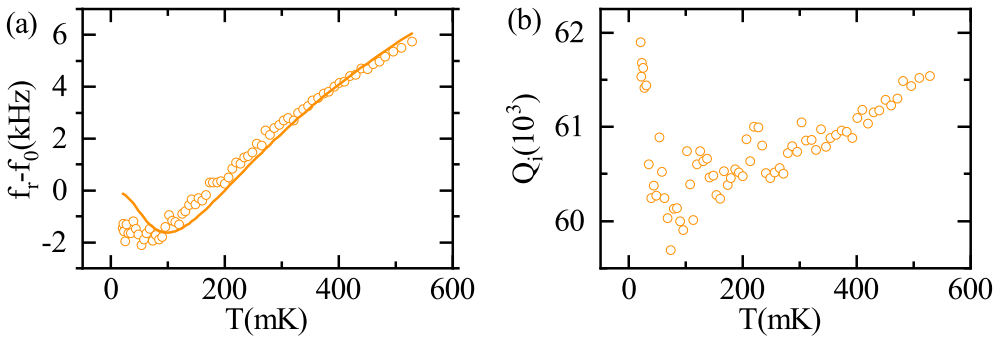

Figure 4.1.5: f_r (a) and Q_i (b) of a single mode from resonator A3, extracted using (2.11). The solid line in panel (a) is a fit to (2.46). A fit to (2.47) of the data in panel (b) does not converge.

Table 4.1.6: TLS contributions of the two resonators A3,A4 after from the frequency shift of temperature sweep.

device	orientation (rad)	$Q_{\mathrm{i,TLS}}$ (10^3)
A3	$\pi/2$	155.6 ± 1.1
A4	$\pi/2$	189.1 ± 6.0

with a larger L_eff the TLS contribution to Q_i becomes larger. One possible explanation is that for a larger volume more TLS in the substrate participate in the resonator and therefore the loss rate increases. However, in order to confirm this hypothesis more measurements are neccessary. We report TLS contributions comparable with literature results on STX-quartz in Ref. [45], where $Q_{\mathrm{i,TLS}} \approx 93 \times 10^3$. The large low power quality factors $Q_{\mathrm{i,TLS}}$ on the bulk LNO are an excellent starting point for cQAD measurements and the SAW resonators are a good reference for SAW resonators on the multi-layer substrates.

4.2 SAW Resonators on LNO-SiO$_x$-Si

After establishing a baseline for SAW resonators using bulk LNO as substrate material, we start with SAW simulations for the multi-layer LNO on insulator (LNOI). These simulations allow us to analyse the different SAW modes in the spectrum for the multi-layer material and determine the SAW velocity and electrode reflectivity r for three different SAW modes in three different SAW resonators. We extract Q_e for the resonances and then discuss different loss channels contributing to the loss rate $1/Q_\mathrm{i}$ in the multi-layer substrate.

4.2.1 Simulations with material parameters for cryogenic temperatures

For the SAW resonators on the material B from Sec. 3.3, i.e. a thin film lithium niobate on insulator (LNOI) stack with a $500\,\mathrm{nm}$ 128°-rotated Y-cut LNO thin film prepared on a $2\,\mu\mathrm{m}$ SiO$_x$ buffer layer resting on a $350\,\mu\mathrm{m}$ Si(100) carrier, the free v_free and metallized v_metal phase

velocities are determined with Finite Element simulations as for SAW resonators on the (bulk) LNO in Sec. 4.1.1. The main difference here is however, that the SAW velocity is no longer dispersion-free in the multi-layer material (see Sec. 2.2) [25] and the SAW wave velocity v_{free} is wavelength λ dependent. For the Finite Element simulations we require the cryogenic material properties of LNO, SiO_x and Si, such as stiffness tensor $\mathbf{C}$, piezoelectric tensor $\mathbf{e}$, density ρ and dielectric tensor ε. The material properties for the LNO at cryogenic temperatures have been described in detail in Sec 4.1.1. The cryogenic properties for the Si are described in Sec. 4.3.1. For the properties of the isotropic SiO_x we use the built in values of our Finite Element software. For the Euler angles of the LNO we choose the same values from Tab 4.1.1 and for the Si/SiOx we only need rotations in the plane.

We show the results from the Finite Element simulations for SAWs on the LNOI substrate

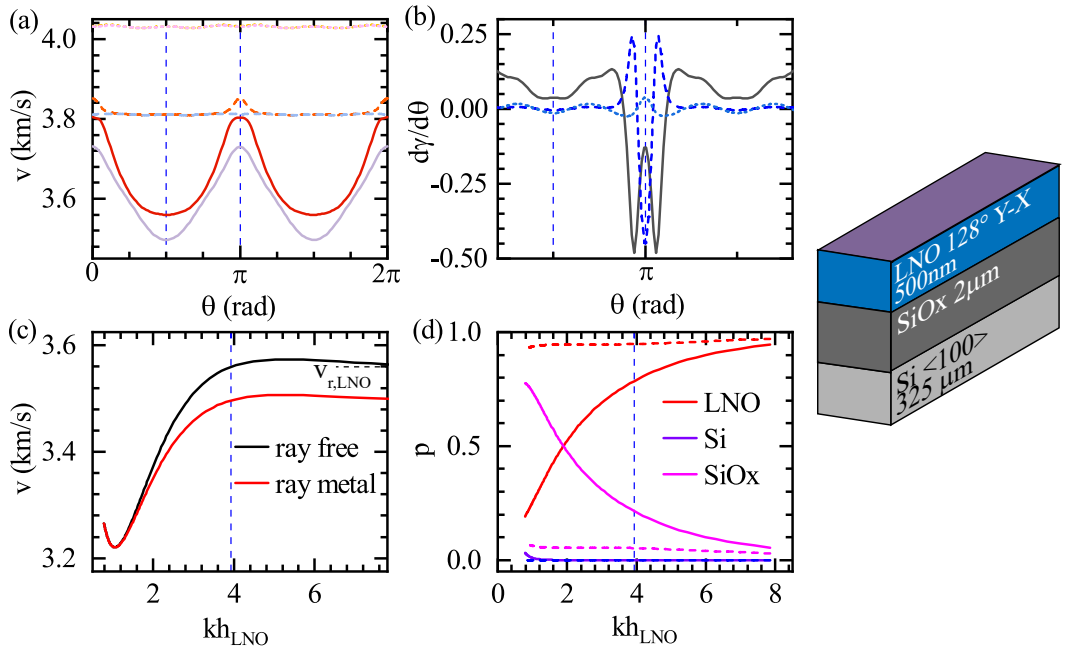

Figure 4.2.1: Simulations of the SAW properties on the LNOI substrate and we repeat the multi-layer stack on the right. (a) Free and metallized SAW phase velocity as a function of the propagation direction θ on the substrate surface. In this LNOI multi-layer system multiple SAW modes exist: Rayleigh mode (solid) for small phase velocities and emerging higher Sazewa modes (dashed and dotted) that display higher phase velocities. (b) Diffraction $d\gamma/d\theta$ of the Rayleigh mode (solid line) and the Sazewa modes (dashed and dotted). (c) the free (black) and metallized (red) SAW phase velocity as a function of kh_{LNO} with wavevector k and LNO film thickness h_{LNO} for the orientation $\theta = \pi/2$. (d) acoustic and electric participation ratios of the SAW mode in SiOx, Si and LNO as a function of kh_{LNO}. The kh_{LNO} value for our multi-layer system and operating wavelength is marked with a dashed line for $kh_{\text{LNO}} = 3.97$.

in Fig. 4.2.1. Panel (a) shows the phase velocity of the SAW for the different propagation directions θ on the LNO-SiO_x-Si substrate. Here it is important that in contrast to the bulk case in Fig. 4.1.1 we see multiple modes with different velocities. The first mode (solid line) with the

Table 4.2.1: Properties of the SAWs on the LNO-SiOx-Si multi-layer in the beam-steering free directions. We give these properties for the Rayleigh and first Sazewa mode. The $d\gamma/d\theta$ is only given for the Rayleigh mode because it is negligible for the Sazewa mode.

orientation (rad)	$v_{\text{free,Ray}}(\text{km/s})$	$\Delta v/v_{\text{Ray}}$ (%)	$d\gamma/d\theta$	$v_{\text{free,Saz}}$	$\Delta v/v_{\text{Saz}}$ (%)
0,π	3804	1.93	-0.07	3852	1.04
$\pi/2, 3\pi/2$	3560	1.77	0.04	3811	$7.7\,10^{-3}$

lowest velocity and a strong dependence on θ is called Rayleigh mode. The next higher mode (dashed line) at $\sim 3.8\,\text{km/s}$ is called Sazewa mode and is way less θ dependent. At $\theta = \pi$ we see a mode splitting between the Sazewa and Rayleigh modes leading to a higher piezoelectric coupling $\Delta v/v$ for the Sazewa mode at this orientation. At even higher velocity $\sim 4.05\,\text{km/s}$ we see the second Sazewa mode (dotted line) with very small $\Delta v/v$. The two directions $\theta = \pi/2, \pi$, indicated with the vertical blue dashed lines, are the orientations that we use for our resonators. For these orientations, the beam-steering vanishes ($\gamma = 0$). In Fig. 4.2.1 (b) we plot the diffraction $d\gamma/d\theta$ of the Rayleigh mode for different θ values. The Sazewa modes show less diffraction compared to the Rayleigh mode, because their phase velocities v_{free} are not as θ dependent. The SAW velocity of the Rayleigh mode becomes dependent on kh_{LNO} and therefore dependent on the wavelength λ, because $k = 2\pi/\lambda$. We plot this dependence in (c) with h_{LNO} the height of the LNO layer. The SAW penetrates the substrate material to about one λ. Therefore, for large λ or small k the SAW travels mostly in the Si and SiO_x and the SAW velocity approaches the the values, which we expect for the SAW velocity on Si. Now for small λ or large k the wave travels mostly in the LNO layer and therefore displays approaches the values expected for bulk LNO in terms of the SAW velocity and the piezoelectric coupling. In (d) we plot the acoustic (solid lines) and electric (dashed lines) participation ratios of the Rayleigh mode for different kh_{LNO} values for the different materials SiO_x,Si and LNO. We witness the same behaviour previously described. We operate our resonators at $kh_{\text{LNO}} = 3.97$ (marked in (c) and (d) with a blue dashed line).
The results for the relevant θ and kh_{LNO} as used in our experiments are summarized in Tab. 4.2.1 and we will make use of these results later to discuss the experimental results.

4.2.2 Resonator spectrum and properties

In Fig. 4.2.2 (a) we show the magnitude of the complex reflection spectrum $|S_{11}|^2$ of the SAW resonator B3 (black), fabricated on LNOI (type B), for high VNA output power $P_{\text{VNA}} = -10\,\text{dBm}$ which translates into an input power $P_{\text{in}} = -76\,\text{dBm}$. The mirrors confine standing SAWs in the stop-band – they appear in the spectrum with the free-spectral range given by the effective distance between the mirrors L_{eff}. We mark one standing wave mode in the spectrum with the resonance frequency $f_{r,6}$ with a dashed blue line and analyze its properties by fitting the data to the reflection mode described in Sec. 2.4 and in particular (2.11).
Some of the individual resonance features in Fig. 4.2.2 (a) have a complex substructure, where next to one main resonance feature there is at least one other feature with smaller magnitude (the

first distinct feature from the left in the spectrum of B3 is the prime example). In our experience this strange behaviour increases, when the number of fingers for the IDT N increases (the SAW resonators on the LNOI substrate have a large $N = 51 - 151$). We suspect, that the reflectivity of the transducer cannot be neglected in the limit of large N and standing SAWs form not only in between the reflectors, but also in between the IDT and either one of the two reflectors. These standing waves could overlap in the frequency space due to their different Δf_{fsr} and lead to the complex peak structure. Regardless of the reason for this effect it complicates the fits of the resonance features in the complex reflection spectrum with (2.11) and we mitigate this by reducing the frequency range around the main resonance feature for the fit, such that we are able to fit with the model of a single resonance feature. Similar to the procedure in Sec. 4.1.2 we analyze

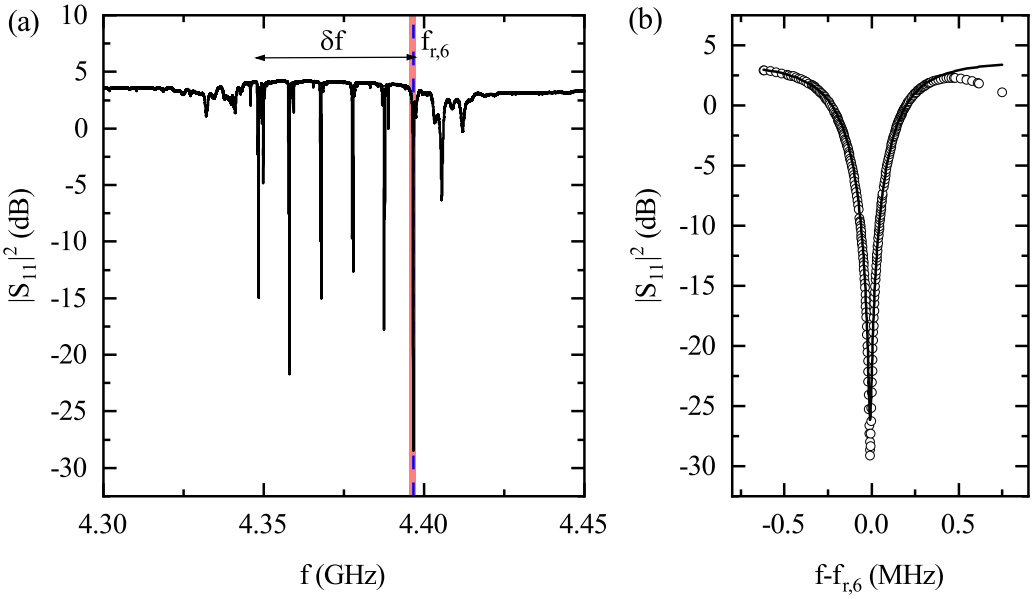

Figure 4.2.2: (a) Uncalibrated spectrum of the SAW resonator B3 from Tab 4.2.2 (black). The resonance at the frequency $f_{r,6}$ in the spectrum is marked with a blue dashed line. (b) Close zoom on the resonance at the frequency $f_{r,6}$ and fit to (2.11) (solid line).

multiple modes present in this resonator the operating frequency of the resonator. We determine the center frequency of the stop-band of the resonator f_{c}, by taking the average frequency of the resonance frequencies f_{r} of the modes in the stop band in Fig. 4.2.2 (a). The wavelength of the standing SAW waves in the resonator is given by the geometry of the reflective gratings $\lambda = 800\,\mathrm{nm}$ and thus we can calculate the velocity of the SAW modes using (2.24) with the stop-band frequency f_{c}. We follow the same procedure for the the resonators B1 and B2 and give the results for the phase velocity of the SAW mode in the resonator in Tab 4.2.2.
The phase velocities differ even for the resonators B1 and B2 with the same orientation $\theta = 0$. The reason is the complex mode structure shown in Fig. 4.2.1 (a). On one hand, for the resonator B1 we measure the spectrum of standing Rayleigh SAWs with the velocity given in Tab 4.2.1

Table 4.2.2: Physical properties of the SAW resonators on LNO-SiO_x-Si multi-layer substrate.

device	orientation (rad)	v_{SAW} (km/s)	L_{eff} (mm)	r (%)	r_{SB} (%)
B1	0	3.762	0.754	0.7	–
B2	0	4.058	0.870	0.6	0.28
B3	$\pi/2$	3.498	0.365	0.6	1.73

for this propagation direction. On the other hand for B2 we measure the spectrum of standing second Sazewa SAWs[1] with a velocity of $v_{2.\mathrm{Saz}} = 4.032\,\mathrm{km/s}$ (see simulation in Sec. 4.2.1). This does not mean however, that the stop-band we did not measure in the experiment is absent for resonators B1 and B2. At the time of the experiment we did not recognize the multi-mode structure of their respective spectrum, which just became apparent with the Finite Element simulations after the measurement. For the case of resonator B3 with propagation direction $\theta = \pi/2$ (see spectrum in Fig. 4.2.2 (a)) the resonances in the spectrum are Rayleigh SAWs. There is good agreement between the experimental results for the phase velocities and the simulation in Tab. 4.2.1, when we distinguish the different modes. The phase velocity difference between Finite Element simulation (see Tab. 4.2.1) and experimental results (see Tab. 4.2.2) for the SAW resonator B3 is $\pm 62\,\mathrm{m/s}$, for resonator B1 it is $\pm 28\,\mathrm{m/s}$ and for resonator B2 $\pm 42\,\mathrm{m/s}$. We want to conclude that for SAW resonators on the LNOI (type B) substrate the complex multi-mode structure, that is a result of the multi-layer substrate, is of great importance for the SAW phase velocities and in the future it would be desirable to measure the stop bands of the different Rayleigh and Sazewa modes in order to quantitatively understand and compare their behaviour. Next, we calculate the free spectral range Δf_{fsr} as the frequency difference between neighboring resonances from the spectrum in Fig. 4.2.2 and take the average value of these differences. From the cavity model in Sec. 2.5.3 we determine L_{eff} of the resonators B1, B2 and B3 using (2.34). We give the results for L_{eff} of the resonators in Tab. 4.2.2. We calculate the penetration depth into the mirror $L_{\mathrm{P}} = (L_{\mathrm{eff}} - L)/2$ from which we can calculate the reflectivity of a single electrode using (2.31). We give the results for the single electrode reflectivity r for the different resonators B1-B3 in Tab. 4.2.2.

The reflectivity r comprises of a mechanical r_{m} and electric contribution r_{e} (see Sec. 2.5.3). For now we neglect the mechanical contribution, because we can not calculate it with our simulations and it is considered to be smaller than r_{e}. We can calculate the electric contribution from (2.20) given our knowledge of $\Delta v/v$ for the Rayleigh and Sazewa modes (see Tab. 4.2.1). Note, that the contribution r_{e} differs for Rayleigh and Sazewa SAWs, because they display different piezoelectric coupling (2.20). For the resonator B1 we expect $r_{\mathrm{e}} = 0.75\ \%$ which is in good agreement with our experimental result ($0.7\ \%$). For the resonator B2 we identified the second Sazewa mode as the dominant SAW mode in the resonator and we expect $r_{\mathrm{e}} = 0.031\ \%$ from our simulations. This value is very small, but consistent with the very weak piezoelectric coupling for this second Sazewa mode predicted by our simulations. However, it is much smaller than the experimentally determined value ($0.6\ \%$). The mechanical contribution r_{m} differs for

[1] We do not show the $|S_{11}|^2$ spectrum of resonators B1 and B2 here, however the phase velocity in Tab. 4.2.2 is calculated using the center frequency of their respective stop-bands.

Table 4.2.3: Mean external quality factors $\bar{Q}_e$ of the three SAW resonators on LNOI multi-layer substrate for different geometric parameters N,W and L_{eff}.

device	orientation (red)	N	W (µm)	L_{eff} (mm)	$\bar{Q}_e$ (10^3)
B1	0	51	285	0.754	13.6 ± 2.6
B2	0	61	238	0.870	15.1 ± 3.3
B3	$\pi/2$	151	110	0.365	18.6 ± 1.4

Rayleigh and Sazewa modes as well, because the displacements u_x, u_y and u_z and potential Φ enter (2.22) and they likely differ for Rayleigh and Sazewa solutions. Potentially, the the mechanical contribution r_m is unusually large for this mode. However, for the resonator B3 we calculate $r_e = 1.27\ \%$ with the $\Delta v/v$ from the Rayleigh mode. This is larger than the experimental result ($0.6\ \%$) and cannot be explained with a mechanical contribution r_m. This indicates either a fundamental problem in our calculations or that we do not complete understand the single electrode reflectivity r. For this reason we employ another method to determine the single electrode reflectivity r, which relies on the fact that the width of the stopband δf is a function of r (2.16).

We explain the method for the resonator B3 as an example: From the spectrum of the resonator B3 in Fig. 4.2.2 (a) we can also determine the width of the stop band $\delta f = 48.16\,\text{MHz}$. We can calculate the single electrode reflectivity r using (2.16) and the result is $r_{\text{SB}} = 1.73\ \%$. This result agrees much better with the single electrode reflectivity, that we calculate beforehand. In the same fashion, we determine from the spectrum of the resonator B2 $\delta f = 9.2\,\text{MHz}$ and calculate $r_{\text{SB}} = 0.28$. This is also in good agreement with calculation from before, when we assume some non-negligible r_m contribution. Unfortunately we cannot employ the same method for the resonator B1, because the stop bands of the Rayleigh and first Sazewa modes overlap, which makes it hard to determine the width of the individual stop bands.

4.2.3 External quality factor

From the individual resonance features in the reflection spectrum of the resonator B3 in fig. 4.2.2 (a) we determine the external quality factor Q_e with a fit to (2.11). We take the mean value of the five center-most resonances $\bar{Q}_e$ for each of the resonators B1, B2 and B3 and list the results in Tab. 4.2.3. Note, that the quality factors of each of these resonators belong to different SAW modes with different coupling factor determined by $\Delta v/v$, which complicates any comparison between the quality factors of the resonators. The resonator B3 should have the smallest $\bar{Q}_e$ from the three resonators, since from the theory follows (2.37) and $Q_e \sim L_{\text{eff}}/(WN^2\Delta v/v)$ and $\Delta v/v$ and N are far larger for B3 than for the other two resonators. The opposite is true for the experimental results in Tab. 4.2.3.

One possible explanation is the complex substructure in the individual resonance features, that we discuss in Sec. 4.2.2. The model, that we use to fit for Q_e using (2.11) assumes a single resonance feature with enough frequency separation between neighboring modes, such that they do not influence one another. This assumption does not really hold for resonance features with this substructure. We see a similar effect in section 4.1.3 for the resonator A2. Therefore the

results for Q_e given here should only be seen as a rough baseline for SAW resonators on the LNOI (type B) substrate. In the future the number of transducer fingers N should be chosen far smaller for SAW resonators on the LNOI multi-layer substrate.

4.2.4 Intrinsic quality factor

High power limit

We determine the intrinsic quality factor Q_i of individual modes in the resonator with a fit to individual resonance features in the complex reflection data using (2.11). As before, the average value of the five center-most resonances at high output power at the VNA - the same procedure is repeated for the other two resonators B1 and B2. We list the result $\bar{Q}_{i,HP}$ in Tab. 4.2.4 for the three different resonators on the LNOI substrate.
The SAW resonator B3 with the Rayleigh SAW mode displays a larger Q_i than the other two resonators with the Sazewa mode. The SAW resonator modes are subject to a number of different loss mechanisms (see Sec. 2.6), such as the finite reflectivity of the mirrors and the diffraction of the SAW in the substrate material. In the Q_i of the individual modes the contribution of all different loss channels is relevant. However, usually a single loss channel dominates and therefore we attempt to identify the limiting contribution for the investigated SAW resonators on the LNOI substrate: The loss contribution due to the finite reflectivity of the mirrors depends on the mirror reflectivity $\Gamma = \tanh\left(N_g r\right)$ at the center of the stop-band and the effective length of the resonator L_{eff}, which we discuss in Sec. 2.5.3. The expected contribution to Q_i from this finite reflectivity $Q_{i,g}$ is determined by (2.40) and we calculate this contribution from the results for the SAW resonators on LNOI and list the results in Tab. 4.2.4. This contribution is not limiting for the SAW resonator B3, while it might be limiting for the Sazewa mode resonators B1 and B2, which have far less piezoelectric coupling $\Delta v/v$ and therefore smaller reflectivity r.
The loss contribution of the diffraction in the substrate depends on the aperture W of the resonator and the diffraction parameter $d\gamma/d\theta$ (see Sec. 2.6). For the resonators B1 and B2 we assume $d\gamma/d\theta = 0$, because the Sazewa modes show far less dependence on the propagation orientation in comparison with the Rayleigh mode in resonator B3 (see Sec. 4.2.1). For resonator B3 we take the simulation result from Tab. 4.2.1 for $d\gamma/d\theta$ and calculate the expected diffraction loss contribution with (2.41) and list the result in table 4.2.4. This contribution is orders of magnitude larger than the result that we determine from the measurements of the resonators. Therefore, we assume that the SAW resonators B1-B3 on the LNOI multi-layer substrate are limited by the propagation loss of the phonons as for the bulk LNO in Sec. 4.1.4.
For the resonator B3, where the Rayleigh SAW mode dominates the spectrum, we can assume

Table 4.2.4: High power intrinsic quality factor contributions of the three SAW resonators on LNO-SiOx-Si LNOI multi-layer substrate.

device	L_{eff} (mm)	W (µm)	$Q_{i,g}$ (10^6)	r (%)	$Q_{i,d}$ (10^6)	$\bar{Q}_{i,HP}$ (10^3)
B1	0.754	285	1.6	0.7	2.0	10.3 ± 1.0
B2	0.870	238	0.03	0.28	1.4	10.7 ± 2.7
B3	0.365	110	2337	1.73	0.3	20.4 ± 1.6

that the losses beside the propagation loss of the phonons is small. We calculate this propagation loss from the quality factor in Tab. 4.2.4 using (4.2). We calculate $\alpha_{\mathrm{P}} = 0.19\,\mathrm{mm}^{-1}$ for the propagation loss and the free phonon propagation length is $l_{\mathrm{free}} = 1/\alpha_P = 5.2\,\mathrm{mm}$. This free phonon propagation length is smaller than the baseline for LNO (bulk) (see Sec. 4.1.4). The multi-layer LNOI system appears to have a detrimental effect on the free phonon propagation length in the SAW resonators in comparison with baseline SAW resonators on LNO (bulk).

TLS contributions

For the low power characteristics of the SAW resonators we measure S_{11} in the vicinity of a single resonance out of the spectrum in Fig. 4.2.2 for different output powers of the VNA between $P_{\mathrm{in}} = -130\,\mathrm{dBm}$ and $P_{\mathrm{in}} = -70\,\mathrm{dBm}$. This individual resonance is chosen as such, that the ratio $Q_{\mathrm{i}}/\Delta Q_{\mathrm{i}}$ is maximized, because this increases the accuracy for Q_{i} and we exclude the resonance peaks with the complex substructure. We extract Q_{i} with fits to the complex reflection data in the vicinity of the individual resonance using (2.11) for the different output powers at the VNA. In Fig. 4.2.3, we plot Q_{i} for different numbers of phonons in the SAW resonator. As before, the average number of phonons in the resonator is calculated using (2.38) accounting for the attenuation, output power at the VNA and line-widths of the resonance that we extract from the fit. Again, the unknown cable loss add an uncertainty to the average number of phonons in the resonator, however this is just a scale factor for the number of phonons n_{phonon} in the SAW resonator. In Fig. 4.2.3, we can see that Q_{i} of resonator B3 saturates for large and

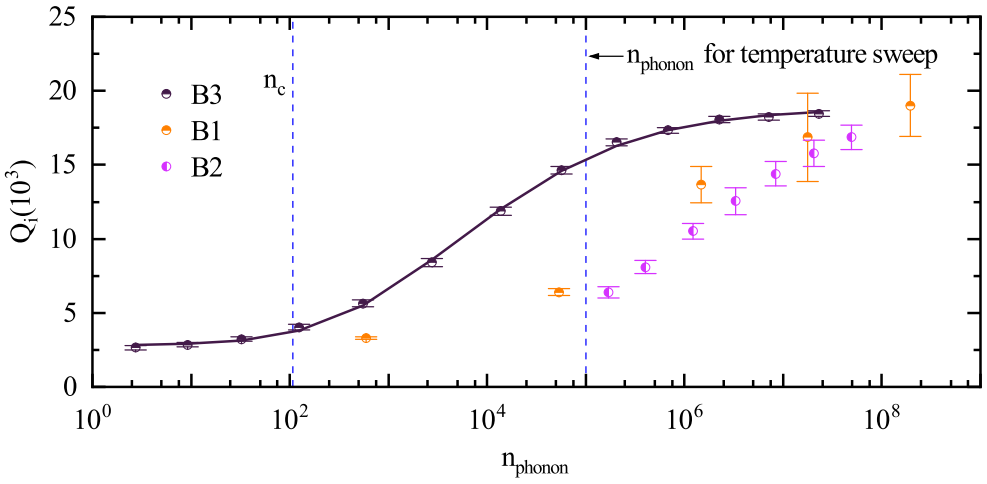

Figure 4.2.3: Q_{i} for one mode of the different devices on LNOI from Tab. 4.2.2 as a function average phonon number in the SAW resonator. The errors ΔQ_{i} are extracted with our fit routine. For resonator B3 we see a clear saturation behaviour for high power and low power in accordance with the TLS model and fit (solid line) to (2.49). The other two resonators B1 and B2 do not saturate for large and small n_{phonon} values and we can not reach the single phonon level with these resonators. We mark the critical phonon number n_{c} for resonator B3 with a blue dashed line.

small phonon numbers. This behaviour is similar to the behaviour of the baseline (bulk) LNO

in Sec. 4.1.4. However, the saturation value for low powers is very small $Q_\mathrm{i} \sim 3 \times 10^3$ in comparison to the resonators on bulk LNO. Q_i of the other two resonators B1 and B2 does not saturate for high or low phonon numbers. For B1 and B2 the resonators have a larger L_eff and therefore smaller Δf_fsr. When the resonance features become very broad for small powers the neighbouring resonance lines overlap and the fit using (2.11) no longer converges. Therefore the resonators B1 and B2 with larger L_eff would also show a TLS induced saturation behaviour (as resonator B3) at low phonon numbers if the resonance were still visible, i.e. the effective length L_eff shorter. We fit the behaviour of the B3 resonance to the TLS model (2.49) (using $\alpha \approx 0.5$) and extract an TLS contribution $Q_\mathrm{i,TLS} = (3.3 \pm 0.1) \times 10^3$ to the intrinsic quality factor for the resonator B3. The critical phonon number $n_\mathrm{c} = 107.5$ for the SAW resonator B3. In Section 2.7, we discuss that temperature sweeps can help to extract the TLS contribution and improve the understanding of the TLS loss channels for the SAW resonator. To this end, we also perform a temperature sweep with the resonator B3. We extract f_r and Q_i from a fit to the complex reflection data of a individual mode of the SAW resonator using (2.11). We measure the complex reflection data of the SAW resonator with $n_\mathrm{phonon} \sim 10^5$ in the resonator, such that we are in the limit of weak fields and (2.47) and (2.46) apply. We plot the results for $f_\mathrm{r}(T) - f_\mathrm{r}(0)$ in panel (a) and Q_i in panel (b) as a function of the temperature in Fig. 4.2.4. The

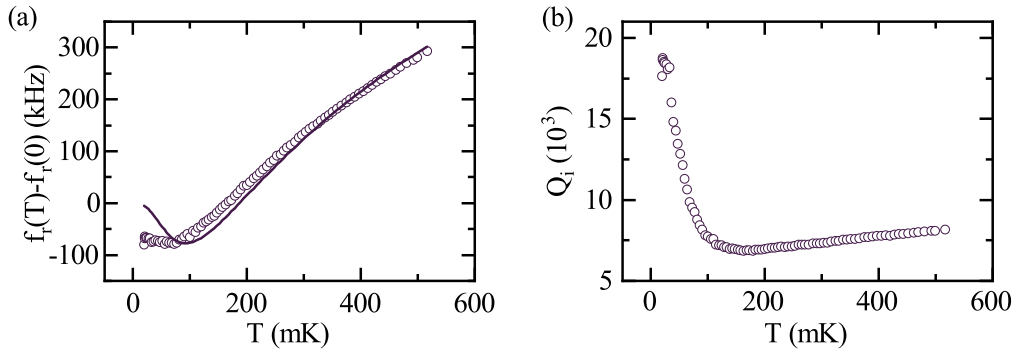

Figure 4.2.4: (a) f_r of a single mode from resonator B3 as function of the temperature. Fit to (2.46) (solid line). The errors are smaller than the size of the symbols. (b) Q_i of the same resonance as a function of temperature. The fit to (2.47) does not converge.

resonance frequency increases with increasing temperature. The total observed shift of 400 kHz is by far stronger than for the bulk LNO in Sec. 4.1.4. We fit the experimental data to the theoretically expected temperature dependence (see (2.46)) and extract the TLS contribution to $Q_\mathrm{i,TLS} = (3.74 \pm 0.01) \times 10^3$. This result is in good agreement with the results we obtained from our power sweeps. The kink in the frequency shift at very low temperatures (100 mK), that is predicted from the TLS theory in (2.46) is absent in the experimental data for the frequency shift. The explanation might be the temperature dependence of Q_i in panel (b), that we discuss soon. For very low temperatures $T < 100\,\mathrm{mK}$ the TLS freeze out - therefore Q_i in (b) increases, but the frequency shift in (a) for $T < 100\,\mathrm{mK}$ through the TLS is absent. Q_i in Fig. 4.2.4 (b) decreases drastically within the first 100 mK from $Q_\mathrm{i} = 20.0 \times 10^3$ to $Q_\mathrm{i} = 6.0 \times 10^3$ before increasing slightly, but roughly linearly towards $T = 600\,\mathrm{mK}$ with $Q_\mathrm{i} = 7.5 \times 10^3$. This

behaviour can not be explained by the TLS model and (2.47) is not able to describe the data. The TLS contributions that we calculated for resonator B3 are far more limiting to Q_i in the single phonon limit than for the resonators on bulk LNO from Sec. 4.1.4. From the study of superconducting microwave resonators it is known that SiO_x is material that has large TLS loss contributions [68]. For microwave resonators, the TLS couple to the electric field of the resonator and dissipate the energy by a possible structural change in their configuration e.g. dangling bonds [52]. We expect that a similar behaviour is thus plausible within SAW resonators based on non-piezo and piezoelectric materials as the elastic and the electric component of the SAWs can couple to the TLS and hence those can cause dissipation. This theory is supported by our Finite Element simulations in Sec. 4.2.1 in Fig. 4.2.1 (d), where we see that there is a finite electric participation ratio $p \sim 0.05$ of the Rayleigh SAW mode in the SiO_x. If the SiO_x has in fact a large density of TLS, that cause losses, a substantial ($p \sim 0.05$) ratio of the energy in the SAW mode can interact with these TLS and cause dissipation. This might explain our experimental result $Q_{\mathrm{i,TLS}} = 3.74 \times 10^3$, which is far smaller than the result for the baseline SAW resonators on LNO in Sec. 4.1.4. The large losses related with TLS severely limits the performance of the SAW resonators on LNOI at low average phonon numbers. This means, that this material system's performance is subpar for applications in cQAD at the current moment.

4.3 SAW Resonators on LNO-Si

We argued that TLS contribute significantly to the losses of the material system B, because of the SiO_x layer in between the Si and LNO layers. One way to strengthen this claim is to compare this data to SAW resonators on the multi-layer system LNO on Si without a SiO_x layer in between. We then expect that the TLS related losses should be reduced and the performance of these devices on a Si-LNO substrate in the single phonon-limit for the SAW resonator should improve. However, the technology for the fabrication of LNO on Si wafers with wafer bonding is still a subject of current research [69–71]. As we cannot fabricate the base material within the WMI we rely here as well on external sources of mixed quality and availability. We again start with Finite Element simulations on this Si-LNO layer-stack, because this allows us to determine the SAW properties, such as phase velocities with free and metal boundary conditions. We determine the experimental results for the SAW velocity and grating reflectivity from the from cryogenic reflection measurements and compare the results with the simulations for four different SAW resonators. Subsequently, we extract Q_e and discuss the loss channels in the multi-layer system at different VNA output powers and temperatures in the fridge.

4.3.1 Simulations with material properties for cryogenic temperatures

We simulate the SAW properties, e.g. $\Delta v/v$ and v_free, with the Finite Element method described in Sec. 2.3 and employed for the Si-LNO multi-layer system in Sec. 3.3. Here, the material system consists of a $300\,\mathrm{nm}$ Y-X-cut LNO thin film prepared on a $525\,\mu\mathrm{m}$ Si(111) carrier (see Fig. 4.3.1). For the simulation we require the material constants $\mathbf{C}$, ρ and ε of LNO and Si at cryogenic temperatures. In detail, we refer to Appendix A.3.1 for LNO material properties extrapolated to these low temperatures and experimentally verified in Sec. 4.1.1. For the low

temperature constants of Si we perform a similar linear interpolation towards $T = 1\,\mathrm{K}$ from the room temperature values for $\mathbf{C}$ and show the result in Appendix A.3.2 [72]. Silicon is a well studied material allowing us to use cryogenic parameters from literature for the permittivity tensor ε [73]. We choose the Euler angles $45, 54.75, \theta$ (°) to adapt the material constants of Si for the <111> direction and tune the SAW propagation direction in the crystal plain by choosing θ.

In Fig. 4.3.1, we show the results of these simulations. In (a) we plot the free and metallized

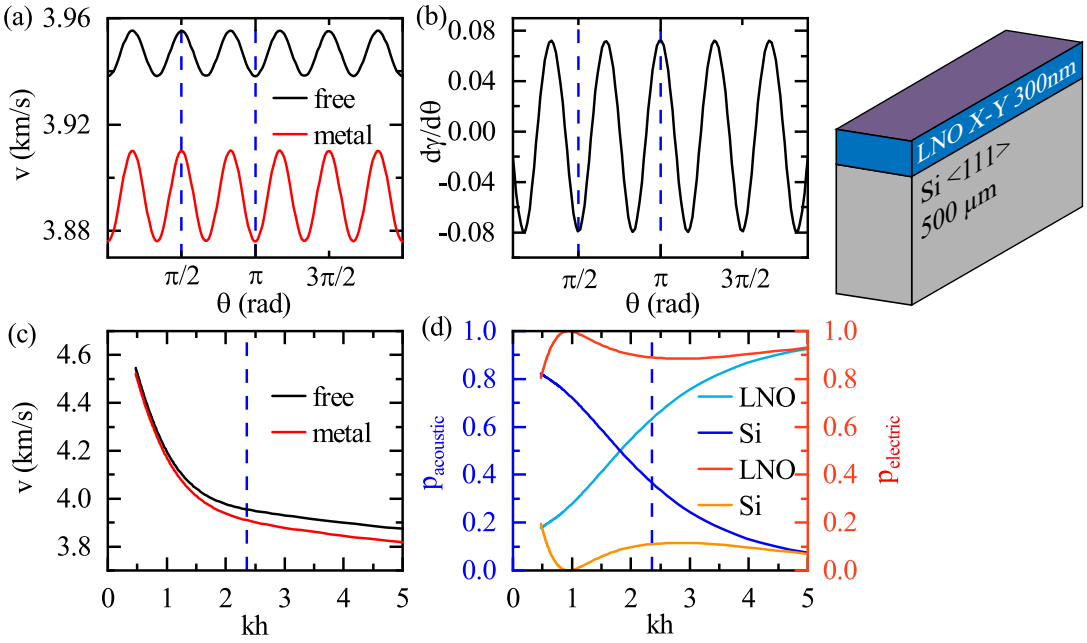

Figure 4.3.1: Simulations of SAW properties on the Si-LNO multi-layer substrate, which is illustrated on the right. (a) Free (black) and metallized (red) SAW phase velocity as a function of the propagation direction θ on the substrate surface. (b) Diffraction $d\gamma/d\theta$ as a function of θ. (c) Free (black) and metallized (red) SAW phase velocity as a function of kh with wavevector k and LNO film thickness h. (d) Acoustic (blue) and electric (red) participation ratios of the SAW mode in Si and LNO as a function of kh. θ and kh values for the SAW resonators are marked with dashed lines.

SAW phase velocity for different propagation directions θ on the surface of the material. There are minima and maxima in the free velocity and there are two directions of interest at $\theta = 0, \pi$ and $\theta = \pi/2, 3\pi/2$ (dashed lines). These directions are nominally free of any beam-steering effects. The free SAW velocity is maximal at $\theta = \pi/2, 3\pi/2$ and minimal at $\theta = 0, \pi$ however the velocity difference between these directions is very small. The piezoelectric coupling given by $\Delta v/v$ is larger for the $\theta = 0, \pi$ direction. In (b) we plot the diffraction $d\gamma/d\theta$ for different directions θ. The diffraction $d\gamma/d\theta$ is smaller for the direction $\theta = \pi/2, 3\pi/2$. We described in Sec. 2.2 that for this Si-LNO multi-layer material the phase velocity of SAWs is not dispersion-free, but instead depends on the wavevector k [25]. For these simulations we choose the direction $\theta = \pi/2$ and simulate the SAW properties for different k values. In (c) we plot the free and

Table 4.3.1: Properties of the SAWs on the Si-LNO multi-layer substrate in the beam-steering free directions that we fabricated resonators on.

orientation (rad)	Euler angles λ, μ, θ (°)	$v_{\text{free}}(\text{km/s})$	$\Delta v/v$ (%)	γ	$d\gamma/d\theta$
0,π	0,90,90	3.938	1.58	0	0.036
$\pi/2$, $3\pi/2$	90,90,90	3.955	1.14	0	-0.079

metallized SAW phase velocity for the dimensionless kh, where $h = 300\,\text{nm}$ is the height of the LNO layer. The kh value with $k = 2\pi/\lambda$, where we operate our SAW resonators is marked with a dashed blue line. v_{free} decreases with increasing kh while the difference between the free and metallized phase velocities increases for larger kh values. This can be explained by the acoustic and electric participation ratios in the two materials Si and LNO as shown in (d). We sum over the acoustic energy/electric energy in the material and divide by the total acoustic/electric energy in the mode to calculate these participation ratios. From (d) it is obvious that for small kh values most of the mode is situated in the Si, which has a higher SAW phase velocity compared to LNO. With increasing kh more of the mode energy is diverted to the LNO and the SAW velocity approaches the LNO SAW phase velocity. This also explains the increase in the coupling for larger kh values as only the LNO is piezoelectric. In general the electric energy in the SAW mode is far smaller than the acoustic energy, which is readily explained by the small coupling factor $\Delta v/v$ of the material. In Tab. 4.3.1 we summarize the simulation results for the two propagation directions that we use for our SAW resonators. We will come back to these results later when we discuss the experimental results.

4.3.2 Resonator spectrum and properties

We measure four different resonators C1-C4 with different properties and propagation directions on the material type C. In Fig. 4.3.2 (a) we show the $|S_{11}|^2$ spectrum of the SAW resonator C1 on material type C with a high output power $P_{\text{VNA}} = -10\,\text{dBm}$ at the VNA and $P_{\text{in}} = -76\,\text{dBm}$ at the device. As we can see there are several resonances in the frequency window in which the mirror reflection Γ is large. We zoom in on the resonance feature at frequency $f_{r,1}$ in Fig. 4.3.2 (b) and fit it to the theoretical model (2.11) for the resonance signature (see Sec. 2.4). From this we obtain the properties of the resonance feature, such as Q_{i},Q_{e} and f_r. This procedure is repeated for all individual modes visible in the spectrum.

We calculate the center frequency of the stop band of the SAW resonator f_c, by taking the average of the resonance frequencies of all individual modes in the spectrum. We know the wavelength λ of the standing SAW modes in the resonator from the design and calculate the SAW velocity in the resonator using (2.24). Furthermore, we repeat this procedure for all the resonators C1-C4 and summarize the results for the SAW velocities for the different resonators in Tab. 4.3.2. We calculate the free spectral range Δf_{fsr} of the resonator modes in the SAW resonator by calculating the frequency difference between neighbouring modes and calculate L_{eff} with this free spectral range using the standard cavity model from Sec. 2.5.3 and (2.34). The results for L_{eff} for the different resonators C1-C4 are given in Tab. 4.3.2. From these we

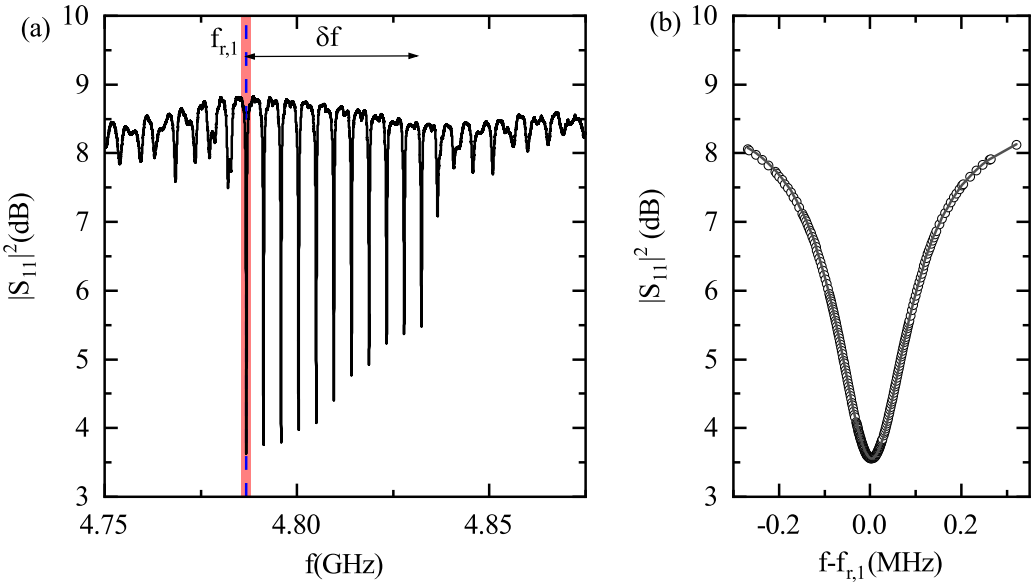

Figure 4.3.2: (a) Uncalibrated spectrum of the resonator C1 in Tab. 4.3.2. The sharp resonance with frequency $f_{r,1}$ in the spectrum is marked with a dashed line. (b) Fit of this resonance with (2.11).

calculate the reflectivity r of a single electrode of the grating with v_{SAW} and L_{eff} in accordance with (2.31). The results for r of the gratings in the resonators C1-C4 are given in Tab. 4.3.2. The experimental results for the SAW velocities for the orientation $\theta = \pi/2$ are about $90\,\mathrm{m/s}$ smaller than the results obtained from the Finite Element simulation shown in Tab. 4.3.1. The same deviation is observed for the other orientation $\theta = 0$. There are two possible contributions to this difference. In Fig. 4.3.3 (b), we show an optical image recorded under white illumination of the chip with the different SAW resonators C1-C4. Assuming that the color displayed in panel (b) can be interpreted in terms of white light Bragg interferometry [74], the different colors suggest a variation on the film thickness over the chip. In (a) we show a SEM image of the edge of the chip at the position indicated by the eye in (b). The height h of the LNO layer at this position is about $370\,\mathrm{nm}$ and therefore larger than nominal thickness of the LNO layer as assumed in the simulations. In Sec. 4.3.1 we simulate the SAW phase velocity for different kh values. For a larger h value the corresponding phase velocity for this multi-layer system gets smaller. A second factor to consider is more trivial. The material properties for cryogenic temperatures are just linear extrapolations and a behaviour, that diverges from this linear interpolation, for cryogenic temperatures is possible.

We introduced that there are two contributions to the reflectivity r of a single electrode. We do not calculate the mechanical contribution r_{m} here using (2.22), because we cannot straightforwardly extract u_x, u_y, u_z and Φ from the Finite Element simulations. However, for a small thickness of the electrodes the electric contribution is typically larger than the mechanical one. The electric contribution to the reflectivity $r_{\mathrm{e}} = 0.8\,\%$ for $\theta = \pi/2$ while $r_{\mathrm{e}} = 1.1\,\%$ for $\theta = 0$

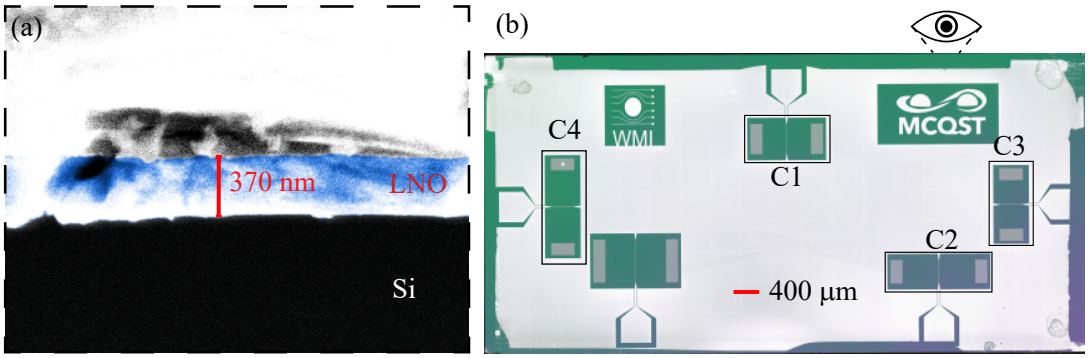

Figure 4.3.3: (b) Optical micrograph of the chip with the resonators in table 4.3.2. The different colors of the chip at the locations of the resonators indicate that the film thickness is not uniform. (a) False-color SEM image of the side-view of the same chip in the location indicated with the eye-symbol in (b).

Table 4.3.2: Physical properties of the SAW resonators on the Si-LNO multi-layer substrate.

device	orientation (rad)	v_{SAW} (km/s)	L_{eff} (mm)	r (%)	r_{SB} (%)
C1	$\pi/2$	3.848	0.843	0.9	1.5
C2	$\pi/2$	3.846	1.254	0.7	1.6
C3	0	3.831	0.898	0.4	1.0
C4	0	3.840	1.334	0.3	0.8

according to (2.20). This does not fit to the experimental results in Tab. 4.3.2. The relative strength of the reflectivity of the two directions is interchanged for these theoretical calculations and the theoretical values are overall too large. In Sec. 2.5.3, we introduce that the width of the stop band Δf is given by the reflectivity r of the gratings. For the resonator C1 we calculate δf using the results from Tab. 4.3.2 and the result is $\delta f = 27.6\,\mathrm{MHz}$. This does not agree with the width of stop band experimentally observed in Fig. 4.3.2 (a). The real value for the reflectivity r therefore must be larger. For the resonators on the other multi-layer material B in Sec. 4.2.2 we have already found that the width of this stop band might be the more accurate way to determine r. We call this r_{SB} to distinguish it from the earlier analysis. We determine the width of the stop band for C1 in the spectrum in fig. 4.3.2 (a) as $\delta f = 45.6\,\mathrm{MHz}$ and calculate r_{SB} from the width of the stop band using (2.16) to $r_{\mathrm{SB}} = 3.0\,\%$. We employ the same method for the other three resonators C2-C4 and give the results in Tab. 4.3.2. This can explain some of the difference between the theoretical reflectivity r_{e} and experimental results, however it remains unclear why the propagation direction $\theta = 0$ displays a smaller r.

4.3.3 External quality factor

We calculate the average value of the external quality factor $\bar{Q}_{\mathrm{e}}$ from the spectrum of resonator C1 in Fig. 4.3.2 (a) by fitting the theoretical model given by (2.11) to the resonances features in

Table 4.3.3: Mean external quality factors $\bar{Q}_\mathrm{e}$ of the four SAW resonators for LNO on Si for different values of N,W and L_eff.

device	orientation (rad)	N	W (µm)	L_eff (mm)	$\bar{Q}_\mathrm{e}$ (10^3)
C1	$\pi/2$	21	502	0.842	78.1 ± 1.5
C2	$\pi/2$	27	388.5	1.254	96.0 ± 1.4
C3	0	27	388.5	0.898	35.9 ± 5.1
C4	0	27	388.5	1.334	63.3 ± 0.7

the spectrum. Then we choose the five centre-most resonances and take the average value $\bar{Q}_\mathrm{e}$. We use the same method for the other resonators C2-C4 and list the results in Tab. 4.3.3.
We plot $\bar{Q}_\mathrm{e}$ against the theoretical dependence of the parameters of the substrate and SAW resonator (see (2.37)) for the four SAW resonators C1-C4. The parameters of the resonator as N,L_eff and W are given in Tab. 4.3.3, while we take the piezoelectric coupling $\Delta v/v$ for the different orientations from the simulation in Sec. 4.3.1 and Tab 4.3.1. $\bar{Q}_\mathrm{e}$ shows a clear linear dependence on this dimensionless combination of SAW resonator parameters and we visualize this linear dependence with a fit to (4.3).
We fit the linear function

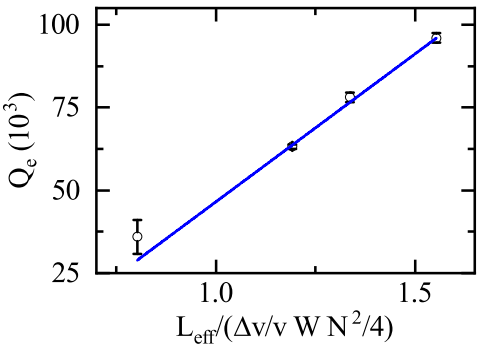

Figure 4.3.4: Mean external quality factor $\bar{Q}_\mathrm{e}$ for the different resonators C1-C4 for LNO on Si with the results given in Tab. 4.3.3. The error $\Delta\bar{Q}_\mathrm{e}$ is the standard deviation of the mean value. There is a linear dependence on L_eff,W and $N/2$ and $\Delta v/v$ as given by the theory in Sec. 2.5.3 and we perform a linear fit to the data (blue).

$$Q_\mathrm{e}\left(L_\mathrm{eff}, W, N\right) = a\frac{4L_\mathrm{eff}}{WN^2\Delta v/v} + b \tag{4.3}$$

with these results and get $a = (98.3 \pm 5.3) \times 10^3$ and $b = (-42.7 \pm 6.7) \times 10^3$. The theory in (2.37) predicts $b = 0$, which is not the case for our fit. From the theory $a = 1/(11.48 v_\mathrm{free}\varepsilon_\infty Z_0)$, however when we assume $Z_0 = 50\,\Omega$ and $v_\mathrm{free} \approx 3.94\,\mathrm{km/s}$ from Tab. 4.3.1, the parameter ε_∞ needs to be $\varepsilon_\infty = 4.5 \times 10^{-12}\,\mathrm{F/m} = 0.5\,\varepsilon_0$. This seems far too small considering, that for bulk LNO $\varepsilon_\infty/\varepsilon_0 = 56$ for 128° Y-X cut bulk lithium niobate [2]. In the end just as in Sec. 4.1.3 we do not understand the value of a. However, the results for a and b should be used in the future in order to choose appropriate coupling κ_e to the SAW resonator.

4.3.4 Intrinsic quality factor

High power limit

From the resonance spectrum in Fig. 4.3.2 with high output power (HP) at the VNA $P_{\text{VNA}} = -10\,\text{dBm}$ we determine Q_i from the resonances with a fit to (2.11) and the mean value of the five center-most resonances is $\bar{Q}_{\text{i,HP}}$. We repeat this for all of the resonators C1-C4 on the LNO-Si substrate and list the results $\bar{Q}_{\text{i,HP}}$ in Tab. 4.3.4. The quality quality factors at high power for the two resonators with propagation direction $\pi/2$ are twice as high as for the 0 direction. The effective length L_eff seems not to have a strong impact on the quality factor of the resonator. The modes in the SAW resonator suffer from a number of different loss channels (see Sec. 2.6), such as the reflectivity of the mirror and diffraction in the LNO-Si multi-layer substrate. In the intrinsic quality factor of a single mode all contributions from the different loss mechanisms are important. We attempt to identify the limiting loss contribution for the SAW resonators on the Si-LNO substrate. The loss contribution the due to the finite reflectivity of the gratings is given by L_eff, N_g and the reflectivity r of a single electrode with (2.40). We calculate this expected contribution $Q_\text{i,g}$ and list it in Tab. 4.3.4. $Q_\text{i,g} \sim 10^6$ and $Q_\text{i,g} \gg \bar{Q}_\text{i}$ and therefore the finite reflectivity is not the dominant loss channel for the high power quality factor for the resonators C1-C4. The loss contribution due to the diffraction in the LNO-Si multi-layer substrate is given by (2.41). $d\gamma/d\theta$ is listed in Tab. 4.3.1 (see Subsec. 4.3.1) for the two orientations and we list the aperture W in Tab. 4.3.4. We calculate the loss contribution due to diffraction $Q_\text{i,d}$ in Tab. 4.3.4 for the SAW resonators. These loss contributions are also $Q_\text{i,d} \sim 10^6$ and therefore not limiting for our SAW resonators. In analogy to Sec. 4.1.4 we calculate the propagation loss α_P for the resonators with the different orientations. Since the HP contributions of the orientations differ greatly we calculate separate propagation losses for the different directions. For the orientation $\pi/2$ the propagation loss is $\alpha_{\text{P},\pi/2} = 0.21\,\text{mm}^{-1}$ taking the average value for the two different resonators C1 and C2. The corresponding free length is then $l_{\text{free},\pi/2} = 4.72\,\text{mm}$. For the other orientation $\theta = 0$ the average propagation loss of the resonator C3 and C4 is $\alpha_{\text{P},0} = 0.44\,\text{mm}^{-1}$. The free length for this orientation is $l_{\text{free},\pi/2} = 2.29\,\text{mm}$.

Table 4.3.4: High power intrinsic quality factor contributions of the four SAW resonators for LNO on Si.

device	orientation	L_eff (mm)	W (µm)	$Q_\text{i,g}$ (10^6)	r (%)	$Q_\text{i,d}$ (10^6)	$\bar{Q}_{\text{i,HP}}$ (10^3)
C1	$\pi/2$	0.842	502	13.4	0.9	6.7	21.0 ± 0.9
C2	$\pi/2$	1.254	388.5	2.7	0.7	4.0	16.6 ± 0.3
C3	0	0.898	388.5	0.1	0.4	3.6	7.9 ± 1.4
C4	0	1.334	388.5	0.06	0.3	3.6	10.4 ± 0.2

Low power limit and TLS contributions

We want to survey the low power characteristics of the resonators on this multi-layer substrate and measure a single resonance of each resonator C1-C4 with varying output power between $P_\text{in} = -160\,\text{dBm}$ and $P_\text{in} = -70\,\text{dBm}$ at the resonator. We choose the resonance with the

maximum value of $Q_i/\Delta Q_i$. We fit the resonances using (2.11) and plot the Q_i as a function of the phonon number n_{phonon} in the resonance of the resonator in Fig. 4.3.5.

We observe, that the two resonators C1 and C2 with propagation direction $\pi/2$ perform better than C3 and C4 with orientation 0. All of the resonances saturate for low n_{phonon}. However in contrast to Sec. 4.1.4 Q_i does not saturate for large n_{phonon}. We interpret this behaviour with the TLS model. For small powers the full contribution to the losses through the TLS is present. For higher powers these TLS are partially saturated, but they still play some role even for high power. We fit the power dependence of Q_i with equation 2.49 and extract the TLS contribution $Q_{i,TLS}$ for the different resonators C1-C4. This behaviour manifests in these fits with $\alpha < 1/2$. In fact for C2 $\alpha = 0.027$, for C3 $\alpha = 0.06$ and for C2 $\alpha = 0.027$. The critical phonon number n_c are $n_c = 2064$ for C2, $n_c = 465$ for C3 and $n_c = 853$ for C4. We plot this spread in Fig.4.3.5. Because of this smaller α the fits become more difficult and come with larger errors for the fit parameters. In the case of C1 the fit fails to converge at all. In the literature this $\alpha < 1/2$ behaviour has been linked to thermally polarized TLS [66].

To quantify this effect, we perform temperature sweeps on the resonator C1 with an input

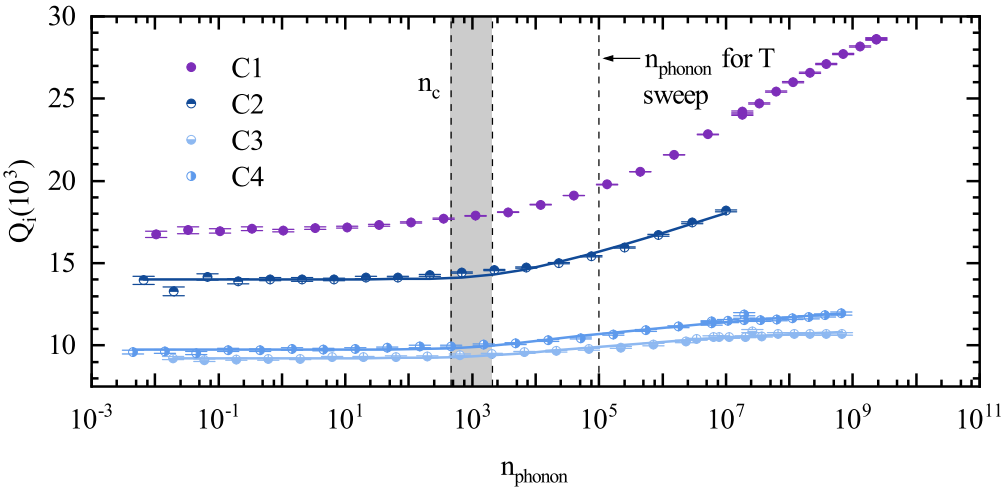

Figure 4.3.5: Intrinsic quality factor for one mode of the different devices on Si-LNO multi-layer substrate from Tab. 4.3.5 as a function of the power (average phonon number in the resonator). Q_i shows a saturation behaviour for small powers - while there is no saturation for large n_{phonon}. We fit the data of all resonators but C1 (the fit formula fails to converge) to the theoretical dependence in (2.49). ΔQ_i for the error-bar is extracted from the fit routine.

power P_{in}, such that $n_{phonon} \sim 10^5$ in the SAW resonator, because in this weak field limit the theory in Sec. 2.7 applies for these measurements. In Fig. 4.3.6 (a) we plot the temperature dependence of the resonance frequency shift f_r with temperature. $f_r(T) - f_r(0)$ has a minimum at $T = 100\,\mathrm{mK}$ with a shift of $\sim -10\,\mathrm{kHz}$ and then increases with higher temperatures to $\sim 40\,\mathrm{kHz}$ for $T = 600\,\mathrm{mK}$. We fit this behaviour to the theoretical behaviour using (2.46) (see Sec. 2.7) and extract an TLS contribution $Q_{i,TLS}$ from the frequency shift. The result from this fit is listed in Tab. 4.3.6. In Fig. 4.3.6 (b), we plot the temperature dependence of Q_i for the resonator C1. The quality factor increases by about $\sim 7.5 \times 10^3$ for higher temperatures. This

Table 4.3.5: TLS contributions of the four SAW resonators C1-C4 for LNO on Si.

device	orientation (rad)	L_{eff} (mm)	$Q_{\text{i,TLS}}$ (10^3)	$Q_{\text{i,LP}}$ (10^3)
C1	$\pi/2$	0.843	36.2 ± 0.2[2]	21.0
C2	$\pi/2$	1.254	14.1 ± 7.6	16.6
C3	0	0.898	35.5 ± 12.3	7.9
C4	0	1.334	35.7 ± 7.8	10.4

Table 4.3.6: TLS contributions of the resonator C1 from the frequency shift and the Q_{i} shift with the temperature sweep.

device	orientation (rad)	Q_{i,TLS,f_r} (10^3)	$Q_{i,\text{TLS},Q_{\text{i}}}$ (10^3)
C1	$\pi/2$	36.2 ± 0.2	27.8 ± 0.4

strong temperature dependence is qualitatively different compared to the behaviour for the LNO (bulk) baseline presented in Fig. 4.1.5 (b). We fit this increase in Q_{i} for higher temperatures to the theoretical model using (2.47) and extract the TLS contribution $Q_{\text{i,TLS}}$ from the temperature shift of Q_{i} and list the result in Tab. 4.3.6. For the TLS contributions $Q_{\text{i,TLS}}$ in Tab. 4.3.5

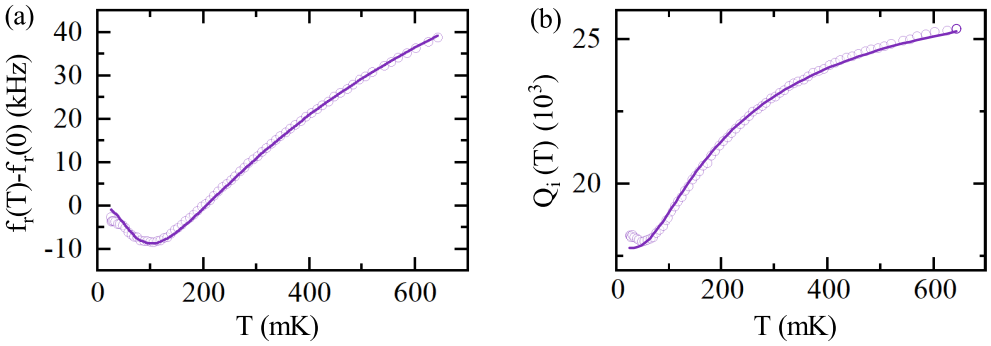

Figure 4.3.6: (a) f_r of a single mode from resonator A3 as function of the temperature. Fit to (2.46). (b) Q_{i} as a function of temperature. Fit to (2.47)

there is no indication that these contributions scale with the mode volume as in the bulk case in Sec. 4.1.4, because the errors contributions from the fits to the power dependence are very large. These TLS contributions $Q_{\text{i,TLS}}$ in the multi-layer case with LNO on Si are an order of magnitude smaller than the contribution for the baseline LNO (bulk) case in Tab 4.1.5. For superconducting resonators LNO is known as a material with large loss tangents due to the piezoelectric effect [75]. Si on the other hand is known as a material with low loss tangents, which makes it an excellent substrate for superconducting quantum circuits [68]. If we were to use the participation ratios simulated in Sec. 4.3.1, the TLS contributions for the multi-layer system should be smaller,

[2]This value is a result from the temperature sweep.

because the acoustic wave travels partially in the Si with better coherence properties. This is however not represented by the results in Tab. 4.3.5. This might be partially explained with a larger thickness of the LNO film in Fig. 4.3.3 (b), because when the film thickness increases the participation ratio of the LNO is increases. However from Sec. 4.1.4 we know, that the TLS losses related to LNO are very small in comparison to the experimental results in Tab. 4.3.5. It is much more likely, that the reason for the TLS related losses lies in the fabrication of the LNO-Si multi-layer substrate. The LNO on Si sample used for the resonators C1-C4 is fabricated with a method called wafer-bonding. Here a typical Si and LNO wafer are bonded together at high temperatures. Subsequently the LNO wafer is polished and etched to reach the $300\,\mathrm{nm}$ thin film. When these wafers become hot the Si wafer must form a layer of thermal SiOx due to the high temperatures involved. We therefore assume that it is highly plausible that a very thin layer of SiO_x in between the LNO and Si forms. However SiO_x is a material with notoriously large loss tangents for superconducting microwave resonators and it is known that even a thin SiO_x layer can dramatically reduce the performance of microwave resonators [68]. This layer of SiO_x could explain the high TLS induced losses in this multi-layer system in comparison to the losses for bulk LNO. We were not able to prove this SiO_x layer or determine its height using the SEM picture in Fig. 4.3.3 (a) and an x-ray diffraction measurement (XRD). The losses through TLS contributions for SAW resonators on the Si-LNO multi-layer substrate ($Q_{\mathrm{i,TLS}} \sim 30 \times 10^3$) are order of magnitude larger than for the TLS losses for the baseline SAW resonators on LNO (bulk). However, even this $Q_{\mathrm{i}} \sim 14.0 \times 10^3$ in the single phonon-limit is sufficient for the application of SAW resonators and devices base on Si-LNO substrates for cQAD applications.

LNO on Si thickness and crystal quality survey using XRD

Motivated by the color variation presented in Fig. 4.3.3 (b) we perform $2\theta - \omega$ measurements[3] with the XRD to study the thickness and quality of the LNO thin-film. The monochromatic X-ray beam is incident on plain of the the sample under the angle ω and is diffracted at the atomic planes of the sample with the angle 2θ [76, 77]. We show the main results from our XRD measurement in Fig. 4.3.7. In (a) we show the results from a **X-ray reflectometry** (XRR) measurement. Here, w as well as 2θ are varied simultaneously under small angles 2θ between $0.5°$ and $5°$ [76]. The direction of the scattering vector $\vec{q}$ remains constant, while the amplitude is changed [76]. In Fig. 4.3.7 (a), we can see that for the angles between $1°$ and $2°$ Kiessig fringes appear due to constructive and destructive interference of reflected X-rays [76]. This intensity profile can be simulated using the **LEPTOS** software to obtain the LNO layer thickness [78]. For the data preselected in Fig. 4.3.7 (a) we obtain $h \approx 350\,\mathrm{nm}$ which agrees with the SEM image in Sec. 4.3.2. A thin SiO_x-layer between the Si and LNO as we proposed would manifest as beat in the reflectometry intensity. There appears to be a beat in Fig. 4.3.7 (a), but the signal quality for large 2θ values is too small for a fit with the software. In (b) we show the results from a **Rocking curve** measurement, where w is varied around the peak of the crystal while 2θ is fixed. The linewidth (FWHM) for the LNO peak $\mathrm{FWHM_{LNO}} = 0.108°$ is far larger than for the Si peak $\mathrm{FWHM_{Si}} = 0.008°$. The expectation for a perfect LNO single crystal would

[3] Here we use the angles 2θ and ω, because that is the notation for XRD measurements in the literature. These are not to the same as θ and ω from other chapters of this thesis.

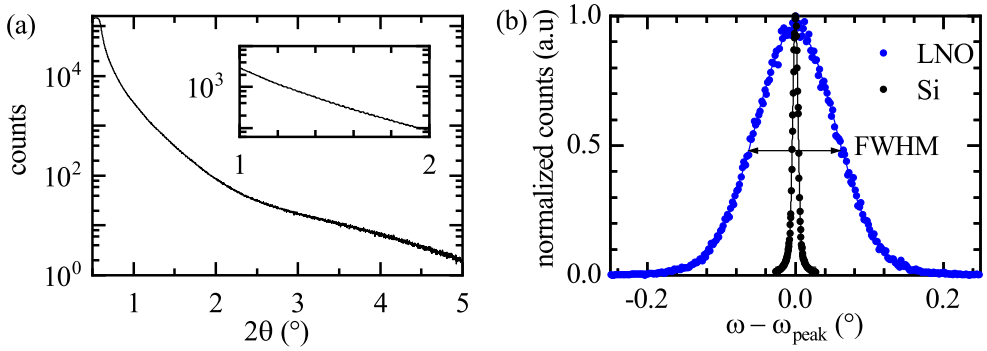

Figure 4.3.7: Results from the XRD measurements on the LNO on Si multi-layer system. (a) **X-ray reflectometry** measurement, where the 2θ angle is varied between $0.5°$ and $5°$. (b) **Rocking curve** in which ω is varied around the peaks for LNO and Si and 2θ is fixed. The maximum counts for both peaks are normalized to unity.

be a similar FWHM value as for the Si, which is a near perfect single crystal. Therefore the crystalline quality of the LNO thin film is not great [76].

4.4 Comparison of the Carious Substrate Materials

After discussing the SAW resonator on three different materials in an isolated fashion, we next compare their relative performance. The multitude of different SAW modes and SAW dispersion in the multi-layer substrate that we witness in Sec 4.2.1 is no fundamental issue for the performance of the SAW resonators. The main difference was observed within the intrinsic loss rate Q_i^{-1} of the resonances for the different substrates.
In Fig. 4.4.1 we plot the average TLS contribution $Q_{i,TLS}$ to Q_i in red for the resonators on the different materials. On the right we plot the average value of the high-power $Q_{i,HP}$ limit (red) for the resonators on the three different materials.
We can see from Fig. 4.4.1 that the SAW resonators on bulk LNO show the best performance of the materials. The TLS limit to Q_i and $Q_{i,HP}$ are far larger for the bulk LNO than for the multi-layer materials. The LNO wafer for the SAW resonator is grown as single crystal and therefore it seems reasonable that there is a reduced amount of defects formed for the bulk LNO. The high power limit is similar for the two multi-layer materials. The reduction in $Q_{i,HP}$ in comparison with the bulk LNO is therefore either inherent to these multi-layer systems or a result of the fabrication techniques employed to establish these multi-layer chips with wafer-bonding. If the loss is inherent to the multi-layer it might be due to the fact that the layer thickness and thereby the SAW velocity is not uniform over the chip. This could lead to a diffraction of the SAW in similar fashion as $Q_{i,d}$ in (2.41). In addition this could also lead to a conversion of SAWs into bulk waves and hereby increase the losses. The other possibility is that a significant portion of the SAW mode travels at the interface of the multi-layers. This interface might have many defects from the wafer-bonding thereby increasing the losses compared to bulk LNO. The limit set by the TLS contribution $Q_{i,TLS}$ of the multi-layer system B with SiO_x is far more severe than

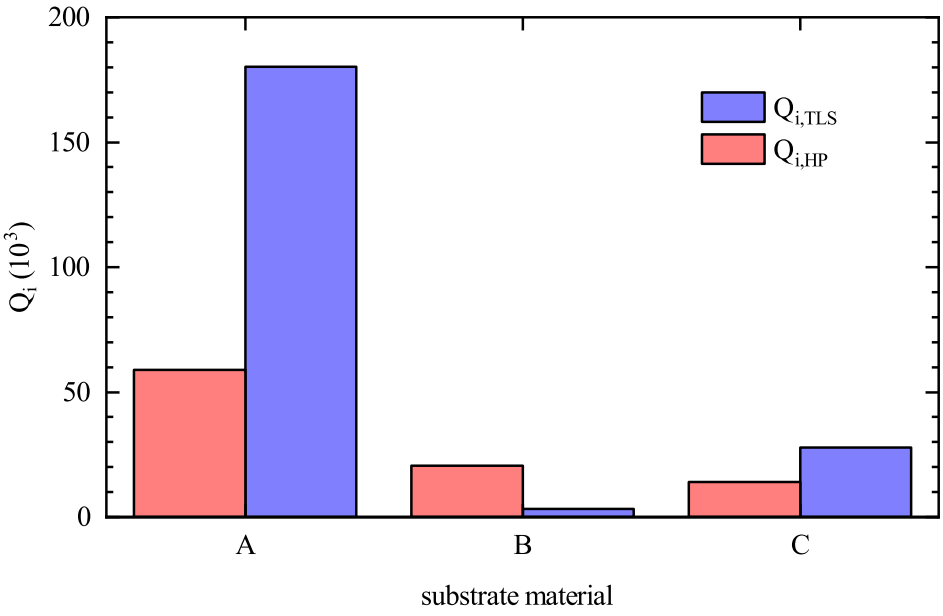

Figure 4.4.1: Average results for the TLS (blue) and HP (red) limits to Q_i for the SAW resonators on the three different material systems.

for the system C without the SiO_x layer in between. Therefore we think that SiO_x induces large TLS related losses for SAW resonators – a phenomena which is established for superconducting microwave resonators [68].

4.5 Conclusion and Future Directions

We have investigated SAW resonators on thin-film LNO on Si and thin-film LNO on SiO_x on Si substrates and compared their performance to reference devices fabricated on the well established bulk LNO. These SAW resonators on the multi-layer substrates work and can be analysed with similar methods as the resonators on bulk LNO. We focus on the internal quality factor Q_i of the resonators, which can be used as an indication for the losses that might limit quantum applications of the SAW devices. On the bulk LNO and thin-film LNO on Si the SAW resonators can be operated down to single phonon occupation levels – with moderate intrinsic Q-factor of 45.7×10^3 and 14.0×10^3 respectively – a pre-requisite for the integration into quantum circuits. We used power- and temperature-dependent measurements to gain further insight into the underlying loss channels in the different substrates, with a focus on the contribution of two-level systems (TLS), which are often limiting the performance of electromagnetic resonators used in circuit electrodynamics [35]. Models for thermal and non-thermal TLS allow us to describe our experimental results and we extract the contribution of the TLS to the total losses of the devices. For bulk LNO we see that $Q_{i,TLS} \gg \bar{Q}_{i,HP}$ suggesting that the TLS are not limiting for these devices, while for the thin-film LNO on Si substrate $Q_{i,TLS} \approx \bar{Q}_{i,HP}$, which is consistent with TLS

limiting the devices in the quantum regime. We attribute this difference in loss behaviour to the additional interfaces introduced due to the multi-layer structure. Studies on superconducting microwave resonators show that interfaces and surface oxides lead to large TLS losses in coplanar waveguide resonators [68]. For the LNOI substrate with SiO_x, that is known to be a dielectric with large TLS related losses, these large TLS related losses appear reasonable. We also suspect that during the wafer-bonding process used to fuse thin-film LNO to Si, a non-negligible thermal oxide layer is formed in between the two layers, producing additional interfaces, potential TLS and defects in the LNO in general. However, even with the increased loss rates compared to bulk LNO devices, SAW resonators on thin-film LNO on Si show sufficient performance in the single-phonon regime to be viable components in quantum acoustic circuits.

Part II

Circuit Quantum Acoustodynamics (cQAD)

Chapter 5

Theory

In this chapter, we want to give an overview on the theoretical considerations behind our design of circuit quantum electrodynamics (cQED) and circuit quantum acoustic devices and introduce the necessary circuit components along with the theoretical framework needed to understand their working principles.

5.1 Circuit Parts

In the following, we will discuss cQED using the so-called X-mon qubit, a variant of the transmon qubit as an effective two-level system [79, 80]. This two-level system is coupled to a microwave resonator and inductive coupler linking the superconducting microwave circuit with the acoustic elements [15, 80, 81].

5.1.1 Xmon qubit

The quantum bit – or qubit – is a quantum-mechanical two-level system with a ground state $|g\rangle$ and an excited state $|e\rangle$. They are separated in energy by $E_\mathrm{e} - E_\mathrm{g} = \hbar\omega_{01}$. According to quantum mechanics, we can express the quantum state of this system by

$$|\Psi\rangle = \alpha\,|e\rangle + \beta\,|g\rangle \tag{5.1}$$

where the complex parameters α and β fulfill the normalization criteria $\alpha^2 + \beta^2 = 1$ [80, 82]. One possible physical realization of such a two level system can be achieved with superconducting circuits. The transmon qubit, that we use for our circuits, is a Cooper-Pair box qubit in a special regime. In Fig. 5.1.1 (a) we illustrate the circuit diagram of a Cooper-pair box qubit. The two physical degrees of freedom in the circuit are charge $\hat{Q}$ and phase $\hat{\Phi}$ operators [83]. This is an LC-circuit with capacitance C_c shunted to ground via a loop of two Josephson junctions with their respective inductive energies $E_{\mathrm{J},1}$ and $E_{\mathrm{J},2}$. We can define $\gamma = E_{\mathrm{J},2}/E_{\mathrm{J},1} > 1$ and without loss of generality $E_{\mathrm{J},2} > E_{\mathrm{J},1}$. Another important quantity for a Josephson junction is the critical current $I_{\mathrm{c},i} = 2\pi E_{\mathrm{J},i}/\Phi_0$ $(i = 1, 2)$ with $\Phi_0 = h/2e$ the flux quantum. The LC-circuit is capacitively coupled to a stiff drive V_g via an additional capacitance C_g. The LC-circuit analogy

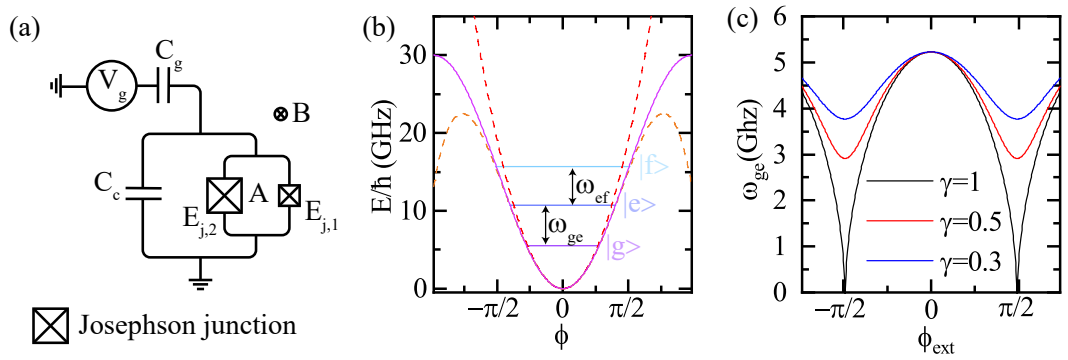

Figure 5.1.1: (a) Illustration of the circuit diagram of a flux-tunable cooper-pair box qubit. (b) Energy level diagram of a transmon qubit with the cosine potential in blue, harmonic and Duffing potential in red and orange dashed lines respectively with $E_\mathrm{C}/h = 250\,\mathrm{MHz}$ and $E_{\mathrm{J},\Sigma}/h = 15\,\mathrm{GHz}$. (c) Tuning curve of the transmon frequency ω_{01} against the external flux for different γ.

becomes more evident, when we write the Hamiltonian $\hat{H}$ describing the circuit of Fig.5.1.1 (a) in the basis of the number of Cooper pairs on the capacitor $n = Q/2e$ and the reduced flux $\phi = 2\pi\Phi/\Phi_0$ with the respective operators $\hat{n}$ and $\hat{\phi}$.

$$\hat{H} = 4E_\mathrm{C}(\hat{n} - n_\mathrm{g})^2 - E_{\mathrm{J},\Sigma}(\phi_\mathrm{ext}).\cos\hat{\phi}. \tag{5.2}$$

Here, the charging energy $E_\mathrm{C} = e^2/2C_\Sigma$ with electron charge e and the sum capacitance $C_\Sigma = C_\mathrm{g} + C_\mathrm{c}$. The number of Cooper pairs $n_\mathrm{g} = -C_\mathrm{g}V_\mathrm{g}/2e$. while the total inductive energy is $E_{\mathrm{J},\Sigma}$ [80, 84]. While the cosine term evidently results in an anharmonicity of the level spectrum, it is useful to expand the cosine term using a Taylor expansion as we are interested in the lowest

lying states

$$\hat{H} = 4E_{\mathrm{C}}(\hat{n} - n_{\mathrm{g}})^2 - E_{\mathrm{J},\Sigma}(\phi_{\mathrm{ext}})(1 - \frac{\hat{\phi}^2}{2} + \frac{\hat{\phi}^4}{24} - \mathcal{O}(\hat{\phi}^6)). \tag{5.3}$$

Figure 5.1.1 (b) shows the potential of the cosine-term in blue, harmonic ($\hat{\phi}^2$) and Duffing-type ($\hat{\phi}^4$) potentials with red and green dashed lines respectively for $E_{\mathrm{C}}/h = 250\,\mathrm{MHz}$ and $E_{J,\Sigma}/h = 15\,\mathrm{GHz}$. Quantization of the harmonic contribution yields the typical energy level structure of the quantum harmonic oscillator [80, 85]. The non-linearity introduced by the Josephson junctions results in an anharmonicity even at the lowest excitation numbers, such that the transition frequency for the $|e\rangle \rightarrow |f\rangle$ transition, where $|f\rangle$ is the second excited state, is given by

$$\omega_{\mathrm{ef}} = \omega_{\mathrm{ge}} - \frac{E_{\mathrm{C}}}{\hbar}, \omega_{ge} = \frac{\sqrt{8E_{\mathrm{C}}E_{\mathrm{J},\Sigma}} - E_{\mathrm{C}}}{\hbar}. \tag{5.4}$$

Note that we identify ω_{eg} as ω_Q as the frequency of the qubit. The anharmonicity α of the qubit is defined as $\alpha = \omega_{ef} - \omega_{\mathrm{ge}}$ and is given by the charging energy $E_{\mathrm{C}}/\hbar$. We operate our qubits in the transmon regime, i.e. $E_{\mathrm{J},\Sigma}/E_{\mathrm{C}} \gg 1$ (typical values are $E_{\mathrm{J},\Sigma}/E_{\mathrm{C}} \sim 100$) which makes them insensitive to charge noise and increases coherence times [80, 86].
When the Josephson junction loop in Fig. 5.1.1 (a) is in a magnetic field B, this magnetic field leads to an external flux $\Phi_{\mathrm{ext}} = A \cdot B$ with A the area of the loop. We can write this as reduced external flux $\phi_{\mathrm{ext}} = 2\pi\Phi_{\mathrm{ext}}/\Phi_0$. The inductive energy of the Josephson junctions $E_{\mathrm{J},\Sigma}$ of the circuit can be tuned with the reduced external magnetic flux

$$E_{\mathrm{J},\Sigma} = (E_{\mathrm{J},1} + E_{\mathrm{J},2})\sqrt{\cos\phi_{\mathrm{ext}}{}^2 + \upsilon^2 \sin\phi_{\mathrm{ext}}{}^2}, \tag{5.5}$$

where $\upsilon = (\gamma - 1)/(\gamma + 1)$ [80]. Taken together, this external flux dependence combined with (5.4) leads to a reduced external flux dependent operating frequency of the transmon qubit. We plot this ϕ_{ext} dependence of the qubit frequency ω_{Q} in Fig. 5.1.1 (c) for different values of γ.

5.1.2 Coplanar waveguide resonator

In Fig. 5.1.2 (a) we illustrate the superconducting circuit version of an harmonic oscillator, the coplanar waveguide resonator (CPWR). The CPWR consists of a center conductor of width $\bar{\mathrm{w}}$ separated from the lateral ground planes by the gap $\bar{\mathrm{s}}$ and with open boundary conditions at each end of the center conductor with length L, [87]. Figure 5.1.2 (b) illustrates the distributed circuit description of a CPWR. For the fundamental mode, a standing wave forms in the center conductor with node and anti-node of the electric field at the open ends of the resonator. The wavelength λ of the fundamental mode is then $\lambda = 2L$ and the frequency of this fundamental mode is

$$f_{\mathrm{r}} = \frac{v}{\lambda} = \frac{c}{\sqrt{\varepsilon_{\mathrm{eff}}}2L}, \tag{5.6}$$

where c is the velocity of light and the effective velocity in the resonator is re-scaled with the permittivity of the substrate $\varepsilon_{\mathrm{eff}} = (1 + \varepsilon_{\mathrm{r}})/2$ [87, 88]. This is due to the fact, that half of the electric field of the mode is located in the substrate and the other half in vacuum ($\varepsilon_{\mathrm{vac}} = 1$) [87]. The $\lambda/2$ mode in the resonator behaves like a quantum harmonic oscillator, i.e. the

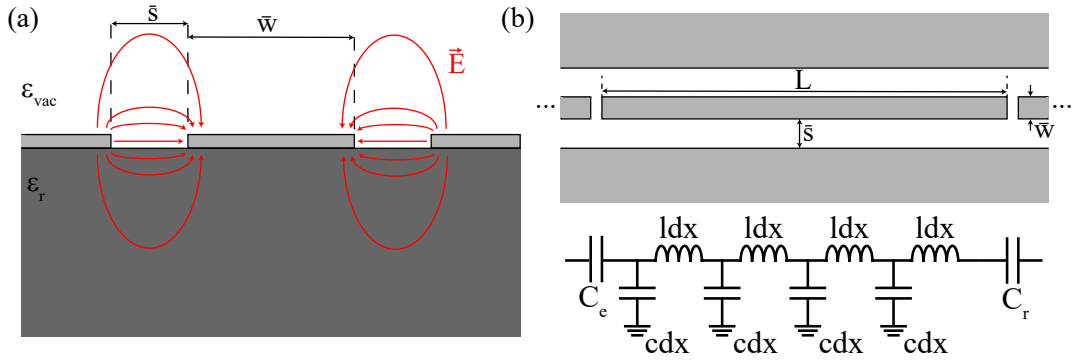

Figure 5.1.2: (a) Illustration of the cross section of a $\lambda/2$ CPWR. (b) Illustration of the $\lambda/2$ CPWR with length L and a distributed circuit model below. The inductance and capacitance of each element dx is given by c and l respectively.

energy levels are equally spaced with the energy difference hf_r. There are three main differences in comparison with the SAW resonator investigated in the previous part of this work: (i) The SAW resonator confines a standing acoustic wave in the resonator, while the coplanar waveguide resonator confines a standing electromagnetic wave. (ii) The effective phase velocity of a mode in a coplanar waveguide is $v_\mathrm{CPW} = c/\varepsilon_\mathrm{eff}$, approximately 3×10^8 m/s and therefore large compared to the SAW phase velocity v_SAW, which is of the order of km/s. (iii) Due to the large difference between v_SAW and v_CPW, SAW resonators usually operate in the large mode number limit. For the SAW resonator usually investigate modes with a large mode number, i.e. higher harmonics, whereas we can directly observe the fundamental mode for the CPWR. The distributed element description in Fig. 5.1.2 (b) allows to calculate the coupling between a coplanar waveguide resonator and a transmon qubit as

$$g = \omega_\mathrm{r} \frac{C_\mathrm{r}}{C_\Sigma} \left(\frac{E_{\mathrm{J},\Sigma}}{2E_\mathrm{C}} \right)^{\frac{1}{4}} \sqrt{\frac{\pi Z_\mathrm{r}}{R_\mathrm{K}}}, \tag{5.7}$$

where C_r is the coupling capacitance between qubit and resonator, Z_r the impedance of the resonator mode and $R_\mathrm{K} = h/e^2$ the resistance quantum [44, 85].

5.1.3 The Jaynes-Cummings Hamiltonian

The interaction between a quantum harmonic oscillator (like a CPWR) with frequency $f_\mathrm{r} = \omega_\mathrm{r}/2\pi$ and a qubit with transition frequency $\omega_\mathrm{Q}/2\pi$ is given by the Jaynes-Cummings Hamiltonian

$$\hat{H}/\hbar = \omega_\mathrm{r}(\hat{a}^\dagger \hat{a} + \frac{1}{2}) + \frac{\omega_\mathrm{Q}}{2}\hat{\sigma}^z + g(\hat{a}^\dagger \sigma^- + \sigma^+ \hat{a}), \tag{5.8}$$

where we neglect decay and higher qubit transitions [85]. The qubit-resonator interaction has the strength g and $\hat{a}^\dagger$ and $\hat{a}$ are the raising and lowering operators of the quantum harmonic oscillator [80, 89]. $\hat{\sigma}^z$ is one of the Pauli matrices and $\hat{\sigma}^\pm = (\hat{\sigma}^x \pm \hat{\sigma}^y)/2$ are the lowering and

raising operators of the qubit [44]. Diagonalization leads to the dressed eigenstates[1] $|+,n\rangle$ and $|-,n\rangle$

$$|+,n\rangle = \cos\theta_{\mathrm{n}}\,|g,n\rangle + \sin\theta_{\mathrm{n}}\,|e,n+1\rangle\,;\; |-,n\rangle = \sin\theta_{\mathrm{n}}\,|g,n\rangle + \cos\theta_{\mathrm{n}}\,|e,n+1\rangle \tag{5.9}$$

with the mixing angle $2\theta_{\mathrm{n}} = \arctan\left(2g\sqrt{n+1}/\Delta\right)$, where $\Delta = f_{\mathrm{Q}} - f_{\mathrm{r}}$ is the qubit-resonator detuning [89]. Through the qubit-resonator coupling g, the dressed eigenstates $|+,n\rangle$ and $|-,n\rangle$ repel in the spectrum of the composite system. One can distinguish between the resonant and dispersive regimes based on the detuning Δ.

Dispersive regime

In the dispersive regime, i.e. $|\Delta| = f_{\mathrm{Q}} - f_{\mathrm{r}} \gg g$ the Jaynes-Cummings Hamiltonian takes the modified form

$$\hat{H}_{\mathrm{dis}}/\hbar = (w_{\mathrm{r}} + \chi\hat{\sigma}^z)\,\hat{a}^\dagger\hat{a} + \frac{1}{2}\,(w_{\mathrm{Q}} + \chi)\,\hat{\sigma}^z, \tag{5.10}$$

where $\chi = g^2/\Delta$ and $\hat{H}_{\mathrm{dis}}$ was expanded up to second order in g [89]. The resonator experiences a dispersive shift $\chi\hat{\sigma}^z$, where the sign of the shift depends on the state of the qubit [85]. This dispersive shift can be used for dispersive readout of the qubit [80, 85].

Dispersive readout

In order to perform quantum non-demolition (QND) readout, the following conditions must be met. If the qubit is not in the eigenstate the QND readout collapses this state into an eigenstate $|e\rangle$ or $|g\rangle$, but does not demolish it [90]. In the dispersive limit $|\Delta| \gg g, \kappa$ there is no longer a direct exchange of energy and the resonator frequency (see Subsec. 5.1.3) and when the first higher transition at the frequency $\omega_{ef}/2\pi$ is taken into account the dispersive shift χ in (5.10) modifies [80] to

$$\chi = \chi_{01} + \frac{\chi_{12}}{2} = -\frac{g^2}{\Delta}\left(\frac{1}{1-\Delta/\alpha}\right). \tag{5.11}$$

In the small photon number limit ($n < n_{\mathrm{c}} = \Delta^2/4g^2$) the interaction term in equation 5.10 commutes with the observable $\hat{\sigma}^z$, which results in a QND measurement [80, 90]. For our experiments we choose the readout power small enough, such that the qubit readout system does not become non-linear, i.e. the resonator frequency does not shift with readout power. The excited and ground states of the qubit are maximal distinguishable in the dispersive QND measurement[2] when $2\chi = \kappa$ [88, 91].

5.1.4 Inductive coupler

For the coupling between the bottom and top elements of the flip-chip assembly we use an inductive coupler as we will mention in chapter 6. For our design we align two coplanar waveguide

[1] $|n\rangle$ is the state of the quantum harmonic oscillator with n photons.

[2] There are different notations for κ, which means that different authors give different results. Here we use the notation for κ from section 2.6.

resonators on the different chips on top of each other in close proximity with the distance $\bar{d}$, while the currents flow in opposite direction for the length $\bar{l}$. For simplicity we assume that the width or diameter of these central conductors is small in comparison to the separation distance[3] $\bar{d}$. We illustrate the assembly in Fig. 5.1.3 (a) as two thin wires separated by the distance $\bar{d}$ with

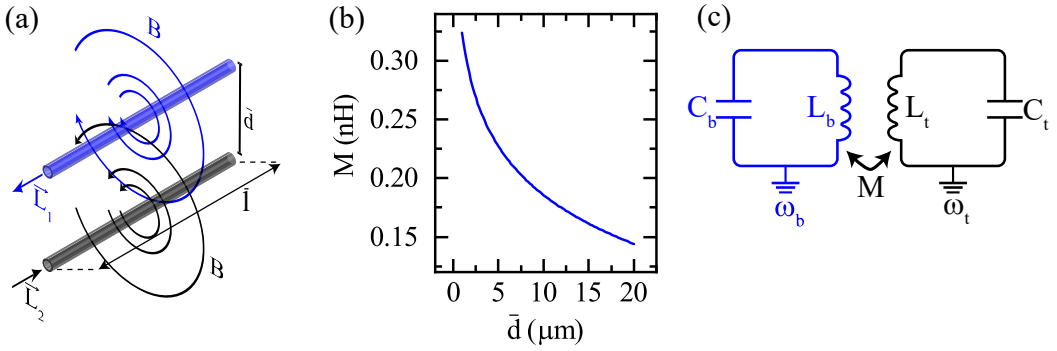

Figure 5.1.3: (a) Illustration of two wires with anti-parallel currents separated by the distance $\bar{d}$ create magnetic fields B. (b) Mutual inductance M between the two wires with $\bar{l} = 300\,\mu\text{m}$ for different separation distance $\bar{d}$. (c) Two harmonic LC-oscillators coupled through the mutual inductance M.

currents flowing in opposite directions $\vec{L}_1$ and $\vec{L}_2$. The current in each of the wires leads to the magnetic field B at the radius r of a thin wire $B(r) = \frac{\mu_0 I}{2\pi r}$ [88, 92]. This creates a magnetic flux Φ in the adjacent wire, which influences the current in this wire. This influence is described by the mutual inductance M. This mutual inductance is given by

$$M = \frac{\Phi}{I} = \frac{\mu_0}{2\pi}\bar{l}(\log\frac{2\bar{l}}{\bar{d}} - 1), \tag{5.12}$$

where we assume that $\mu_\text{r} \approx 1$ [93]. In Fig. 5.1.3 (b) we plot the mutual inductance between two wires of length $\bar{l} = 300\,\mu\text{m}$ as function of their separation distance $\bar{d}$. The mutual inductance increases for smaller separation distance and is of the order of nH.

For our flip-chip assembly (see chapter 7) a coplanar waveguide with unspecified length L is attached to one end of the inductive coupler, while the other end is shorted to ground. This combination of inductive coupler and coplanar waveguide is a $\lambda/4$ coplanar waveguide resonator with the frequency $\omega_{\text{t,b}} = 1/\sqrt{L_{\text{t,b}}C_{\text{t,b}}}$ with the inductance $L_{\text{t,b}}$ and capacitance $C_{\text{t,b}}$. Here we write t and b to indicate, that such a $\lambda/4$ coplanar waveguide resonator exists on both the top (t) and bottom (b) chip and their frequencies do not necessarily coincide. These two CPWRs, which are quantum harmonic oscillators as we introduce before, are coupled through the mutual inductance M of the inductive coupler in (5.12). When two quantum harmonic oscillator couple interact through the mutual inductance M we can write this interaction in a Hamiltonian $\hat{\mathcal{H}}$ (A.18) and determine the coupling g between two quantum harmonic oscillators using circuit quantization in Appendix A.4. The coupling g between the two quantum harmonic oscillators

[3] This is a very strong simplification. We want to describe the theory behind the coupling – the real mutual inductance values will differ greatly.

on the top (t) and bottom (b) chips is then given as

$$g = \frac{1}{4}\sqrt{Z_\mathrm{t} Z_\mathrm{b}}\omega_\mathrm{t}\omega_\mathrm{b}\frac{M}{\sqrt{L_\mathrm{t} L_\mathrm{b}}}. \tag{5.13}$$

When the coupling g between the top and bottom quantum harmonic oscillator modes is large enough the two with frequencies ω_t and ω_b should hybridize into a single mode with frequency ω_hybrid. The superconducting elements, e.g. a qubit on the bottom chip and a SAWR on the top chip, can then couple indirectly through the hybridized mode with indirect coupling strength $\mathcal{J}$ with a type of waveguide extender [94]. Note, that we just give a qualitative description for the inductive coupler and in the future a lot of optimization and simulation is neccessary to improve the coupling strength $\mathcal{J}$. In this chapter we introduce the properties of the superconducting circuit elements, e.g. the transmon qubit that we return to later in Chapter.9 to discuss the qubit measurements. Furthermore we introduce the CPWR and QND read out of the qubit state and finally we discuss the inductive coupler, that we use to connect the superconducting circuit elements to the SAWR on a different chip.

Chapter 6

Mediated Indirect Capacitive Coupling between Qubit and SAWR

The field of circuit quantum acoustodynamics (cQAD) investigates the potential of quantum circuits interfacing acoustical or electrical excitations in mechanical resonators [12, 14, 15, 95–98]. One successful realization is comprised of a superconducting qubit that is piezoelectrically coupled to a surface acoustic wave cavity [19]. Here we distinguish two different options: (i) the SAWR and qubit couple directly with the strength g and (ii) SAWR and qubit couple indirectly through for example a CPWR with the strength $\mathcal{J}$. For the first realization the capacitor plate of the superconducting qubit was in essence the IDT of the SAWR with the direct coupling strength g [96]. For this reason, the superconducting qubit had been fabricated on the same piezoelectric material hosting the SAW resonator [96]. However, this design strategy – while easier to implement – suffers from a reduced performance of the superconducting qubit as the piezoelectric effect creates an unwanted loss channel, which reduces the coherence times T_1 and T_2 [75].
One strategy to mitigate the losses originating from undesired coupling of the qubit is to spatially separate the superconducting circuit elements from the piezoelectric material and mediate the indirect coupling with the strength $\mathcal{J}$ through a superconducting circuit element, e.g. CPWR. We distinguish two possible configurations for the indirect coupling: (i) a planar – etch – integration of coupled elements implemented by spatial separation (see Fig. 6.0.1) and (ii) a flip-chip approach (see Fig. 6.0.2). In this thesis we consider both configurations. Both configurations have in common that the superconducting flux-tunable single-plate-capacitor qubit (Xmon), readout resonator and control lines are made out of metal residing on an silicon substrate chip. A high resistivity silicon substrate at cryogenic temperatures for instance allows to use the great coherence properties and proven fabrication methods for superconducting qubits [23]. Furthermore in both configurations an additional coplanar waveguide (CPW) structure is used to mediate the coupling between qubit and SAWR over a longer distance. In principle, these waveguide extenders form CPW resonators as well, but their length is chosen such, that their resonance frequency is far detuned from the circuits operating frequencies [94].
In the etch configuration in Fig. 6.0.1 we have a multi-layer chip that consists of a silicon chip with a thin-film of a piezoelectric material on top (in our case layer stack C from Sec. 3.3). We then employ reactive ion etching (RIE) to selectively remove the piezoelectric layer on parts of the chip where we place the superconducting circuit elements like the readout resonator and qubit. This process was already shown in-house [44]. However, we identify the challenge that our RIE system is no longer able to provide the power neccessary to etch away the lithium niobate.

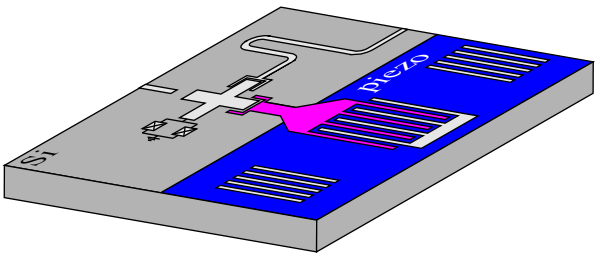

Figure 6.0.1: We illustrate a multi-layer piezoelectric-on-silicon chip, where the piezoelectric layer (blue) has been removed for the superconducting qubit,readout resonator and drive-line - bare silicon (grey). The SAWR is on the part of the chip where the piezoelectric layer still exists and they are connected through a superconducting coupling resonator (magenta).

Figure 6.0.2 shows the alternative ansatz where the superconducting circuit elements and the surface acoustic wave resonator are on separate chips. Both chips are then combined into a single device using a so called flip chip assembly. We have no dedicated flip-chip bonder at the WMI and the piezoelectric material must be transparent for optical light, such that one can use markers to align the two chips with regards to each other. In order to define the separation distance d between the two chips we define thick thick epoxy resist slabs on the bottom chips. When the piezoelectric chip with the SAWR is flipped, aligned on top of the bottom chip and attached to one another, the resist slabs ensure the separation distance d. Inductive couplers are used to allow indirect interaction between SAWR and qubit through electromagnetic fields (magenta). In the illustration we can see two red boxes one on each chip that highlight one inductive coupler – and these red boxes align on top of each other in the final flip-chip assembly. This configuration has been successfully implemented and used for cQAD experiments in Refs.[14, 15, 81].
While the physical possibilities should be the same for both configurations, due to technical difficulties with the RIE process necessary to realize the on-chip configuration, we focus on the second flip-chip configuration for this thesis. This configuration is especially interesting because flip-chip geometries are currently investigated as a platform for 3D integration to scale up the number of qubits for quantum computing [80, 81, 99].

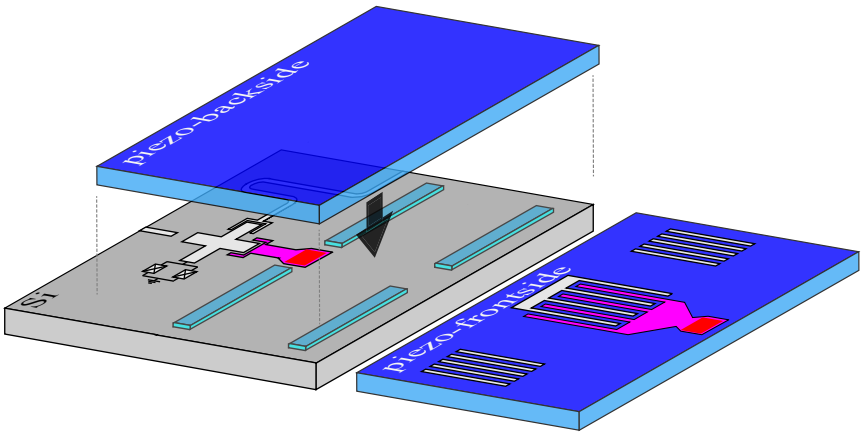

Figure 6.0.2: We illustrate a flip-chip geometry, where qubit and surface acoustic wave resonator are on different chips, one silicon (grey) and the other piezoelectric (blue). In a flip-chip geometry the chips lie on top of each other separated by resist slabs. Qubit and SAWR are coupled through a superconducting resonator (magenta) distributed on both chips, where the red boxes on the silicon and piezo chip lie on top of each other in the end.

Chapter 7

Design cQAD Flip-Chip

Most of the properties of the relevant circuit elements for our cQAD experiments, such as resonance frequency, impedance, coupling strength and mutual inductance depend on the geometry of the element [44]. For the best performance we chose the value for these properties and then design and optimize the circuit with Qiskit Metal[1]. Qiskit Metal supports a connection to Ansys HFSS[2] to optimize the geometric properties of our design.
The finalized design for our cQAD bottom and top chip are shown in Fig. 7.0.1 (a) and (b) respectively. The bottom chip consists of a $\lambda/2$ coplanar waveguide resonator (CPWR) for readout (yellow) and a Xmon qubit(blue/grey). The qubit and CPWR are themselves coupled to transmission lines (light blue). The qubit frequency can be changed with an on-chip flux-line (blue). Finally the bottom chip is coupled inductively to the top chip via a coupling resonator ($\lambda/4$) (midnight blue).

In order to avoid reflection between different circuit elements the impedance $Z_0 = 50\,\Omega$ is matched across elements. In the limit of infinite substrate thickness the inductance of a coplanar waveguide (CPW) is given by

$$Z_0 = \frac{30\pi}{\sqrt{\varepsilon_{\mathrm{r,eff}}}} \frac{K(k_0')}{K(k_0)}, \tag{7.1}$$

where $K(k_0)$ and $K(k_0')$ are elliptic integrals with $k_0 = \bar{w}/(\bar{w} + 2\bar{s})$ and $k_0' = \sqrt{1 - k_0^2}$ [47]. Here $\bar{\mathrm{w}}$ is the width of the CPW and $\bar{s}$ the gap to the ground plane (see Fig. 5.1.2 (a)). For our design we choose $\bar{\mathrm{w}} = 10\,\mu\mathrm{m}$ and $\bar{s} = 6\,\mu\mathrm{m}$ for our readout CPWR. We design all transmission lines, flux line and coupling CPWR with the same $\bar{\mathrm{w}}/\bar{s}$ ratio and therefore with the same inductance Z_0. The effective dielectric constant $\varepsilon_{\mathrm{r,eff}} = (\varepsilon_{\mathrm{r}} + 1)/2 = 6.2$ using the dielectric constant of silicon at cryogenic temperatures $\varepsilon_{\mathrm{r}} = 11.45$ [47, 73].

Xmon qubit

For our qubit we choose the Xmon design [79] shunted to ground via two Josephson-junctions. We have two Josephson junction that form a superconducting quantum interference device (SQUID) and therefore our qubit is flux-tunable. An external flux through an external magnetic field through the area A of the SQUID leads to an external magnetic flux ϕ_{ext} that changes E_{J} of the qubit (see (5.5)) and thereby the fundamental frequency of the qubit $\omega_{\mathrm{ge}} = \omega_{\mathrm{Q}}$ in (5.4). One advantage of the Xmon is the multitude of coupling avenues through the horseshoe

[1] https://qiskit.org/documentation/metal/
[2] https://www.ansys.com/products/electronics/ansys-hfss

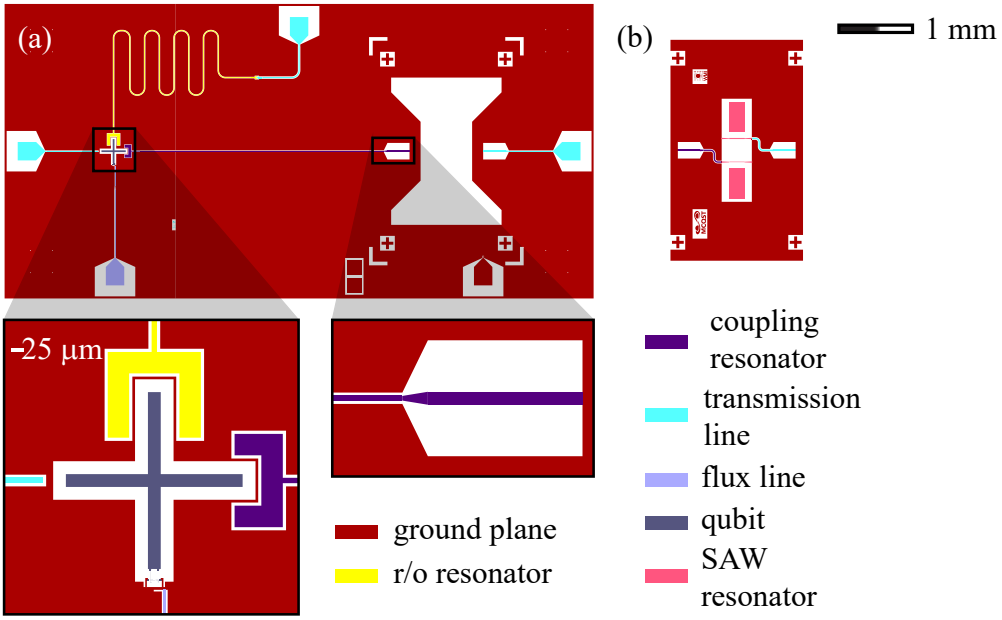

Figure 7.0.1: (a) The full design for the bottom chip for the flip-chip geometry. We zoom in on the Xmon qubit and a inductive coupler that facilitates the coupling between top and bottom chip. (b) The design for the SAW resonator on the top chip. Details for the design can be found in the main text.

couplers. The horseshoe couplers allow for large coupling to a CPWR and good coherence times have been demonstrated [79]. For the Xmon we choose the length of the capacitor arms $X = 165\,\mu\mathrm{m}$ and $\bar{w} = \bar{s} = 24\,\mu\mathrm{m}$ for the width and gap to ground of the X-shaped capacitance [79]. In Fig. 7.0.1 (a), we show a micrograph of the Xmon with the claw-shaped coupling structures to other circuit elements. The X-shaped capacitor plate defines the capacitive energy of the qubit $E_\mathrm{C} \approx e^2/(2C_\mathrm{C})$, where we neglect the capacitance of the junction itself, and the anharmonicity $\alpha = -E_\mathrm{C}/hbar$. From Ansys HFSS simulations we determine $C_\mathrm{C} = 85.78\,\mathrm{fF}$ for the capacitance of the capacitor plate from the Maxwell capacitance matrix [100]. In order to target the qubit frequency, we determine the critical current of a junction from the qubit Q01 (see Tab. 9.1.1). The critical current of a single junction is $42.03\,\mathrm{nA}$ and together with its junction area of the Al/AlO_x/Al interface of $332.8 \times 380.8\,\mathrm{nm}^2$ and we determine the critical current density[3] $j_\mathrm{c} = 33.2\,\mathrm{A/m\,cm}^2$, which is lower but on the same order of magnitude as Ref.[101]. For the frequency target of $5\,\mathrm{GHz}$ this means the junction areas of the asymmetric SQUID are $175 \times 175\,\mathrm{nm}^2$ for the larger Josephson junction and $54.25 \times 54.25\,\mathrm{nm}^2$ for the smaller Josephson junction, where we adjusted for the process blur of our junction fabrication process. This should yield $\gamma = E_{\mathrm{J},2}/E_{\mathrm{J},1} = 3.1$ and $\upsilon = 0.51$ for the asymmetric SQUID.

[3] This is determined from a SEM image of the junction and is larger than the design with $250 \times 250\,\mathrm{nm}^2$.

Readout CPWR

The readout CPWR is a $\lambda/2$ resonator with the length $L \approx 8\,\mathrm{mm}$ in order to target the resonator frequency $f_\mathrm{r} \approx 7\,\mathrm{GHz}$. The CPWR meanders (see Fig. 7.0.1 (a)) in order to reduce the footprint on the chip. This meander will reduce the effect capacitance c and inductance l per unit length due to floating ground around the center-conductor [88]. This resonator is coupled to the transmission line in reflection through a capacitance structure. We determine the external quality factor Q_e with a driven model study in Ansys HFSS [102, 103] and target an external quality factor for the resonator of $Q_\mathrm{e} = 8 \times 10^3$. The qubit is capacitively coupled to the resonator through the large claw capacitance in Fig. 7.0.1 (a) and we determine the coupling capacitance $C_\mathrm{r} = 6.46\,\mathrm{fF}$ from the Maxwell capacitance matrix. With (5.7) we aim for $g \approx 100\,\mathrm{MHz}$. This puts the resonator qubit system in the dispersive regime $\Delta \gg g$ which is used for dispersive readout of the qubit.

Flux line

We design the qubit with an on-chip fluxline (light blue). This CPW splits into two branches at the end – thereby forming two current loops. The current through this flux bias line results in a magnetic field and thereby changes the flux inside the SQUID [88]. The current flow in the superconductor is however not straightforward and magnetic imaging has been used on these flux-lines [104]. We choose the design for the fluxline from Ref. [79]. The main advantage of an on-chip flux-line over a superconducting coil mounted over the SAW resonator is, that multiple flux-tunable elements can be accessed independently of each other, which is very important in order to scale the devices up and be able to host multiple flux-tunable components.

Coupling resonator

The coupling resonator for information exchange between the top and bottom chip is a $\lambda/4$ resonator, where one end is shorted to ground via a wider section of CPW - the inductor. This inductor is wider than the rest of the CPWR in order to increase the overlap in a flip-chip geometry and reduce the necessary accuracy for the alignment. In order to avoid impedance mismatch we taper the CPW to the width of the inductor. The length of this CPWR is $L = 3.8\,\mathrm{mm}$ and the corresponding frequency of this resonator is $f_\mathrm{r,CO} = 7.9\,\mathrm{GHz}$. The other part of the coupling resonator on the top piezoelectric chip is even shorter. In theory these two modes should hybridize to $\omega_\mathrm{hybridize}$ (see Subsec 5.1.4). The capacitive coupling to the qubit is quantified with the Maxwell capacitance matrix with $2.76\,\mathrm{fF}$. In the future one needs to simulate the mutual inductance M between the two resonators on the top and bottom chips.

SAW resonator

For the SAW resonator on the top chip we follow the design for the SAW resonator in Sec. 3.1. There is an additional IDT structure for coupling between the qubit and the SAW resonator. Both IDTs have $N = 21$ fingers and $N_\mathrm{g} = 1000$ and length $L = 0.5\,\mathrm{mm}$. The inductor couples the transmission line and coupling resonator to the bottom chip. The IDTs relative position is set by

Table 7.0.1: Design parameters for the bottom chip.

Qubit	Q01
$\omega_{\mathrm{r}}/2\pi$	$7\,\mathrm{GHz}$
Q_{e}	8×10^3
$\omega_{\mathrm{Q}}/2\pi$	$5\,\mathrm{GHz}$
g	$100\,\mathrm{MHz}$

design so that they couple to the same symmetric standing waves in the resonator.

In this chapter we have discussed the design choices for the circuit elements for our cQAD flip-chip assembly, such as the qubit frequency, readout resonator f_{r} and external quality factor Q_{e} and the coupling resonator. In the future further optimization for all these superconducting circuit elements will be neccessary to improve the performance.

Chapter 8

cQAD Methods

In this chapter we introduce the methods, that we use for our version of circuit quantum acousto-dynamics (cQAD). We start with the fabrication of our design, which we introduced in Chap. 7. Then we discuss our approach for the flip-chip assembly and explain some of the challenges we saw ourselves up against. Finally we discuss our experimental setup for frequency- and time-domain measurements.

8.1 Qubit Fabrication

For the qubit fabrication process we closely follow established process flows, which have been optimized at the WMI to achieve reliable fabrication of superconducting circuits for quantum computing applications. A more detailed description of the recipes is given in Appendix B and for even more details of our qubit process at the WMI we refer to Ref.[23]. The essential steps of the process are illustrated in Fig. 8.1.1.
The bare high resistivity ($\rho > 10\,\mathrm{k}\Omega$) Si substrate is cleaned with Acetone and IPA in the ultrasonic bath and subsequently immersed in Piranha solution[1] to remove organic contamination. The native silicon oxide layer is removed by dipping the substrate in a buffered oxide etch (BOE)[2] solution. Afterwards a $150\,\mathrm{nm}$ thick Nb film is sputter deposited in the Plassys ultra-high vacuum (UHV) system at room temperature. This is where our illustration in Fig. 8.1.1 starts off with panel (a). In panel (b) the sample is spin coated with the optical resist **AZ MIR 701**, which is patterned with a laserwriter and subsequently developed to define a negative mask. In the reactive ion etching (RIE) system the Nb is removed, where it is not protected by the resist mask. When the mask is removed, everything besides the Josephson elements is completed. Next, the chip is spin-coated with a double electron beam resist system, where the bottom layer is **CSAR 62** and the top layer polymethylmethacrylate (**PMMA**) (see panel (c)). This allows in principle for highly tunable undercuts to achieve reproducible Josephson junctions with a high yield [23]. The resist for the Manhattan-type Josephson junctions is patterned in our in-house electron beam lithography, developed and subsequently transferred to the Plassys evaporation system. For the description of the next steps (d)-(f) in Fig. 8.1.1, we leave out the resist-structure to keep it simple. We deposit an Al/AlO_x/Al trilayer for our Josephson junctions with a technique know as shadow-angle evaporation [105]. (d) The sample is tilted by $\beta = 50°$ and only the arms of the Manhattan junction in parallel with the evaporation direction is evaporated with

[1] Mixture of concentrated H_2S_{04} and aqueous H_2O_2 [23]
[2] BOE consists of HF,NH_4F and H_2O [23]

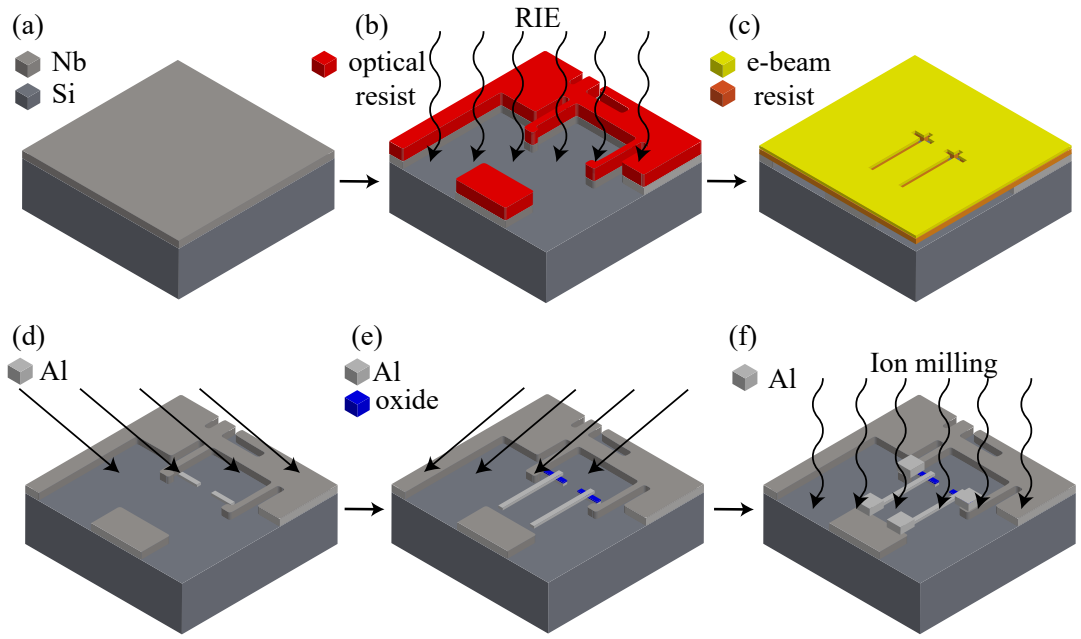

Figure 8.1.1: Illustration of the qubit fabrication process around the SQUID of our Xmon. Details to the fabrication steps are given in the main text. The sizes are not to scale.

30 nm of Al, while the rest is evaporated into the resist walls. (e) To create the insulating AlO_x the sample is oxidized in-situ in a low-pressure O_2 atmosphere, where we use dynamic oxidation. Subsequently, the sample is rotated by 90° around the normal axis and the second arm of the Manhattan junction is evaporated using Al with a thickness of 70 nm. The overlap of the two arms form the Al/AlO_x/Al Josephson junctions. The excess Al is removed in a lift-off process. In order to ensure galvanic contact between the Nb structures and the Al arms of the Josephson junctions a separate bandaging step is required [106]. This step can help to reduce damage to the substrate below the metal film of the Josephson junctions and hereby help to improve the coherence times [106]. Then, the sample is again coated with the double-layer e-beam resist system (see panel (f)). Bandages are patterned and developed with the e-beam lithography system and the surface oxides of Al and Nb underneath the bandages are removed prior to the deposition of a 200 nm Al layer with argon-ion milling in the Plassys UHV system.
The qubit sample is ready for further fabrication steps or to be transferred into a dilution refrigerator.

8.2 Flip-Chip Assembly

The design for the top and bottom chip for the flip-chip assembly is described in Chap. 7 and we discuss the neccessary fabrication steps for the bottom qubit chip on Si and top SAW resonator chip on $LiNbO_3$ (LNO) in Secs. 8.1 and 3.2, respectively. A similar approach for the flip-chip assembly was described in [15, 107]. Resist spacers on the bottom qubit chip are defined

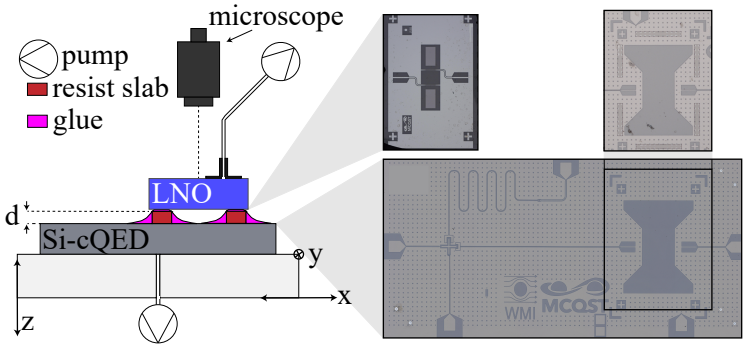

Figure 8.2.1: Illustration of the flip-chip assembly with optical microscope pictures of the bottom qubit and top SAW resonator chips. Details are given in the main text.

with optical lithography in order to define a controlled separation distance d between the chips. While Refs. [15, 81] use the epoxy-based SU-8 resist, that is sensitive to near UV $365\,\mathrm{nm}$ light, we choose the microresist product **DWL-5**, because the exposure wavelength of $405\,\mathrm{nm}$ is compatible with the writing-head of our in-house laserwriter. The chip is spin-coated with the **DWL-5** resist, where the thickness d of the film is determined by the rotation speed during the spin-coating. We aim for a thickness d of $5\,\mu\mathrm{m}$. The separation structure in form of a pedestal is exposed using the laserwriter and subsequently developed. In order to improve the stability of the spacers we apply a post process hard-bake to the resist spacers. A detailed recipe for the resist spacer fabrication is given in the Appendix B. Our fabrication process and available $128°$Y-X cut $\mathrm{LiNbO_3}$ chips force us to fabricate the SAW resonators on $10 \times 6\,\mathrm{mm}^2$ chips. We have to cut the chip into the smaller $2 \times 3\,\mathrm{mm}^2$ size after the fabrication. In order to protect the SAW resonator structure from damage we coat the chip in the optical **AZ MIR 701** resist before cutting the chips with a small circular saw. During this process the chip gets heats up to a temperature, where the resist starts to cross-link. Thus it was not possible to remove the protective resist layer completely. Furthermore the $\mathrm{LiNbO_3}$ chip tends to splinter during the cutting process.

The final process for flip-chip assembly is illustrated in Fig. 8.2.1. The bottom qubit chip with the resist spacers is held in place by the suction of low pressure of a pump on a stage, that can be moved independently in x,y and z direction. The LNO chip is fixed to a suction-cup with low pressure provided by a second pump, while the SAW resonator structure faces down. The mounting of this suction cup needs to be stable during the process. The transparent LNO chip allows to align the markers on both chips on top of each other with appropriate movement of the stage with the help of a microscope. Before the chips are pressed together we apply a small amount of glue (also **DWL-5** epoxy resist) on the resist spacers. When the chips are pressed together the glue is quickly heated up with a heat-gun and the two chips are glued to each other. However, we discovered some issues with this process. First of all there is a finite angle between the bottom-chip and top chip with the suction-cup and they are not perfectly parallel. This mismatch leads to an error for the alignment between the chips of $\sim 10\,\mu\mathrm{m}$. The width of our inductive couplers is just $25\,\mu\mathrm{m}$, so a $10\,\mu\mathrm{m}$ offset can impact the coupling performance quite

significantly. Secondly the amount of glue needs to be carefully dosed, one needs enough glue to make sure the two chips stick to each other, while excess glue should be avoided, as it can act as a dielectric and/or mass loading influence on the SAW resonator and CPW resonators.
Due to these challenges we were up to now not able to successfully assemble a functioning flip-chip assembly.
Note, that the flip-chip technique employed here is rather primitive and relies on readily available equipment. Therefore we are confident that more suitable equipment will improve the required accuracy for this process.

8.3 Measurement Setup

For the measurements of the qubit chip, we use the same commercial dilution refrigerator which we used for the measurements of the SAW resonator with $T_{\text{base}} \approx 20\,\text{mK}$. The device under testing (DUT) for the experiments is described in Chap. 7 and consists of a frequency-tunable Xmon qubit capacitively coupled to a readout resonator, that is itself coupled capacitively to a feedline in the reflection geometry. The chip is bonded to our qubit package and we show an image of the chip in the box in Fig. 8.3.1. The complete measurement setup is illustrated in Fig. 8.3.2 and a DC voltage source generates a current that passes through attenuators and a low-pass filter to induce a magnetic flux through the SQUID loop and thereby control the qubit frequency. We start with the the continuous wave (CW) spectroscopy experiments in the frequency domain and then explain the setup for the pulsed-time domain experiments.

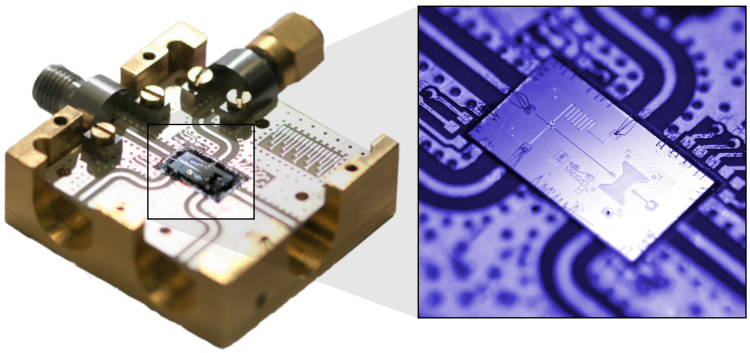

Figure 8.3.1: Isographic image of the qubit chip with Q02 in the package.

8.3.1 Frequency domain

For the measurements in the frequency domain we use a vector network analyser (VNA), operating in CW mode. We use the microwave setup depicted in Fig.8.3.2. For our experiment, we make use of two microwave input lines: One to probe the readout resonator in a reflection measurement (readout line) and a second one to excite the qubit (drive line). In the illustration of the time domain measurement setup in Fig. 8.3.2, we connect the ports 1 and 2 of the VNA at the points 1 and 2 in the illustration. The output signal of the VNA goes through microwave

attenuators with a total attenuation of $-66\,\mathrm{dB}$ and is then routed through a cryogenic circulator to the DUT. The attenuation on the input lines is important for the reduction of thermal noise photons as well as proper thermalization of the microwave lines at the lower stages of the dilution refrigerator [108]. Thermal noise due to the connection of the chip to the electronics at room-temperature leads to both qubit dephasing and energy relaxation through the creation of quasi-particles [108]. And proper thermalization of the cables, attenuators and other microwave components is therefore essential [108, 109]. The signal is reflected at the DUT and rerouted with the circulator to a dedicated readout line with superconducting microwave cables. This readout line is isolated from the environment with four cryogenic circulators and the signal in the readout line is amplified with a cold amplifier at $4\,\mathrm{K}$ and an additional one at room temperature, each providing $42\,\mathrm{dB}$ gain. The VNA measures the complex scattering parameter S_{21}. We use the red microwave-input line in Fig. 8.3.2 in order to excite the qubit. For a two-tone measurement, we connect a third port of the VNA at the point 3 in the illustration. Our VNA supports a two-tone measurement mode, generating the drive tone itself at an additional output port 3. Alternatively, a separate microwave source can be used. The drive signal is attenuated with $-66\,\mathrm{dB}$ for the same reasons as the readout-line and excites the qubit with an on-chip antenna.

8.3.2 Time domain

For the time domain measurements the setup should allow to detect the qubit state in a time resolved manner in order to investigate the characteristic timescales on which decoherence and dephasing takes place. The qubit state is encoded in the phase and amplitude of the microwave signal, that is reflected at the readout resonator [110]. We perform a **heterodyne** readout of our qubit, that means the output quadratures $I(t)$ and $Q(t)$ oscillate at an intermediate frequency f_{IF}. There are two major advantages: If we were to demodulate the signals to DC they are subject to much stronger 1/f electronic noise [80]. Furthermore this intermediate frequency allows for frequency division multiplexing, i.e. the simultaneous readout of multiple qubits at different f_{IF} pulse frequencies [80, 111]. We use a commercial quantum analyzer device (UHFQA[3]), which combines the function of arbitrary waveform generator (AWG) and analog-to-digital converter (ADC). This greatly simplifies the usually challenging task of synchronizing microwave pulses used for probing the resonator with the subsequent digitization of time resolved data. Readout pulses are generated at readout pulse in the quadratures I and Q at the intermediate frequency $f_{\mathrm{IF,RO}} = 200\,\mathrm{MHz}$ and separated into the quadratures I and Q. Individual control of I and Q allows for advanced pulse shaping and potentially even "optimal control" (i.e. algorithmically optimized pulse shapes [111]). Up-conversion of the pulses to the frequency of the readout resonator $f_{\mathrm{r}} = f_{\mathrm{LO,RO}} - f_{\mathrm{IF,RO}}$ in the red-side-band is achieved with a balanced I-Q mixer with the carrier frequency of a local oscillator at the frequency $f_{\mathrm{LO,RO}}$. After an additional attenuation step, in order to reach appropriate powers for the readout pulse, the signal enters the fridge and is reflected at the readout-resonator. Down-conversion of the reflected signal to f_{IF} is achieved with an identical balanced I-Q mixer, and the same local oscillator which was split by a power divider. The I-Q quadratures $s_{\mathrm{out,IF}}$ at the intermediate frequency are amplified separately and

[3] Here we use the 600 MHz UHFQA from Zurich Instruments

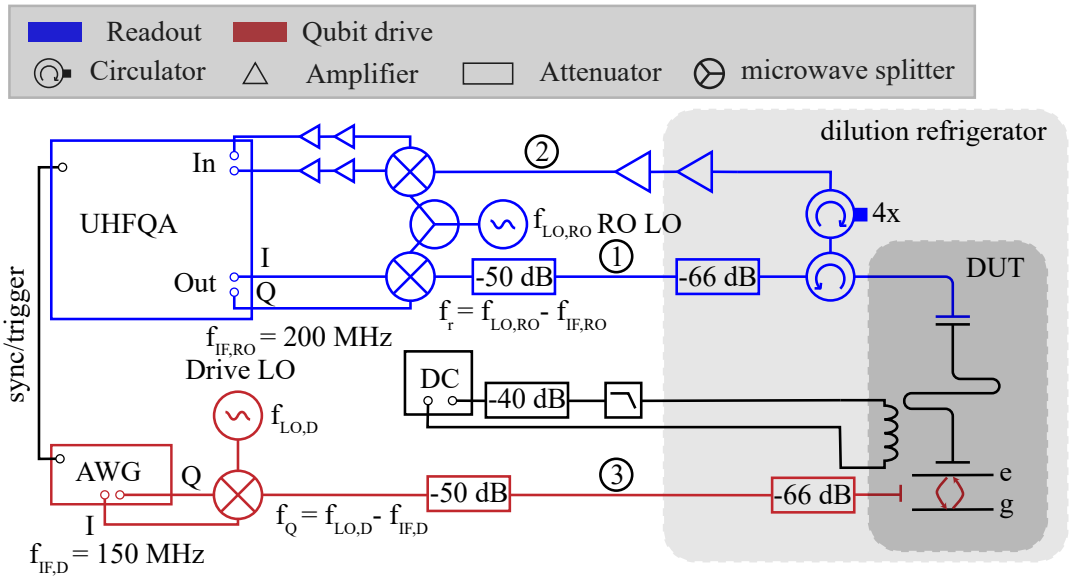

Figure 8.3.2: Illustration of the time domain measurement setup for the cQAD measurements. All devices are synchronized to a 10 MHz rubidium clock. We describe the individual aspects the setup in detail in the main text.

enter the UHFQA

$$s_{\text{out,IF}} = \frac{A_{\text{LO}} A_{\text{RO}}}{8} \left[\cos\left(w_{\text{IF}} t + \vartheta\right) + \sin\left(w_{\text{IF}} t + \vartheta\right)\right]. \tag{8.1}$$

After down-conversion the signal is digitally demodulated and integrated with the UHFQA [111]. This digital demodulation comprises and multiplication of I_{IF} and Q_{IF} with $\cos w_{\text{IF}} t$ and $\sin w_{\text{IF}} t$ respectively. Averaging eliminates the $2w_{\text{IF}}$ component while it retains the DC component and the quadrature can be used to find the amplitude A_{RO} and phase ϑ [80]. We need a lot of averaging for the final result ($\sim 16 \times 10^3$), because the HEMTs do not provide quantum limited amplification [112] and add a non-negligible number of noise photons to the readout signal, which typically only contains one photon on average [109]. The single qubit drive pulse is generated at the intermediate frequency $f_{\text{IF,D}} = 150\,\text{MHz}$ with an AWG and then up-converted to the qubit frequency $f_{\text{Q}} = f_{\text{LO,D}} - f_{\text{IF,D}}$ in the red side-band with another local oscillator and balanced I-Q mixer. This pulse at the qubit frequency is sent into the fridge after an additional attenuation step. All devices operate on the same 10 MHz frequency standard provided by a rubidium clock. The UHFQA triggers the AWG at the appropriate time.

Chapter 9

Qubit Characterization

While final assembly of the flip-chip package was unfortunately not achieved within the time-frame of this thesis, the individual elements were successfully fabricated. In this chapter, we present characterization measurements evaluating the performance of a qubit chip, fabricated according to the design presented in Chap. 7, as it would be used in the final cQAD assembly.

9.1 Qubit Spectroscopy

The setup for the spectroscopy experiments in the frequency domain is described in Subsec. 8.3.1. We start to probe the response of the resonator with single tone spectroscopy and determine S_{11} of the readout resonator in reflection for a small frequency band in the vicinity of the resonance. We plot the absolute values $|S_{11}|$ as function of the applied external flux ϕ_{ext} to the SQUID of the qubit in Fig. 9.1.1 (a). The $|S_{11}|$ reflection amplitude is encoded in color and the dip of the resonance feature can be seen in panel (a) as darker color. This plot becomes clearer, when we analyse a linecut of the colormap at $\phi_{\text{ext}} = 0$ displayed in Fig. 9.1.1 (b). The resonance signature appears as a dip at the frequency $f_{\text{r}} = 6.41\,\text{GHz}$. The frequency of the resonator f_{r} changes on a scale of $\sim 2\,\text{MHz}$ through the coupling to the qubit at frequency $\omega_{\text{Q}}/2\pi$. In Subsec. 5.1.3 we discuss the coupling between a qubit and the readout resonator and through the coupling g the eigenmodes in the qubit and resonator are mixed and the resonance frequency $\omega_{\text{r}}/2\pi$ is dressed through the interaction ω_{Q}. The eigenmodes avoid each other and the change in qubit frequency $\omega_{\text{Q}}/2\pi(\phi_{\text{ext}})$ changes the detuning Δ and therefore the dressed resonator frequency $\omega_{\text{r}}' = \omega_{\text{r}} - g^2/(\Delta - E_{\text{C}}/\hbar)$, where we neglect the dispersive shift [88]. In the future we should be able to extract g from this measurement. We employ the circlefit (see Sec. 2.4) to determine the coupling $\kappa = 5.55\,\text{MHz}$, $Q_{\text{i}} = 30 \times 10^3$ and $Q_{\text{e}} = 9.6 \times 10^3$ of the readout resonator from a fit with (2.11) to the resonance signature in Fig. 9.1.1 (b). The results from the single-tone spectroscopy of the readout resonator are listed in Tab. 9.1.1. Now that we have determined the frequency f_{r} of the resonator we perform a two-tone measurement on the qubit-resonator system. We apply a single tone at the frequency of the readout-resonator f_{r} and determine $S_{11}(f_{\text{r}})$, such that $|S_{11}(f_{\text{r}})|$ is the value of the scattering parameter in the dip of the resonance. If we excite the qubit, f_{r} shifts by 2χ due to the dispersive shift (see Subsec. 5.1.2) and consequently the reflection amplitude $|S_{11}|$ at the fixed readout frequency f_{r} changes [44]. The second tone in order to excite the qubit is applied at the frequency $\omega_{\text{p}}/2\pi$ with another microwave input-line (drive line) and an on-chip antenna. This pump tone at frequency $\omega_{\text{p}}/2\pi$ is varied to perform spectroscopy of the qubit. When the drive frequency coincides with the qubit frequency ω_{Q} or a higher transition the resonator frequency ω_{r} shifts and therefore $S_{11}(f_{\text{r}})$ changes. More details

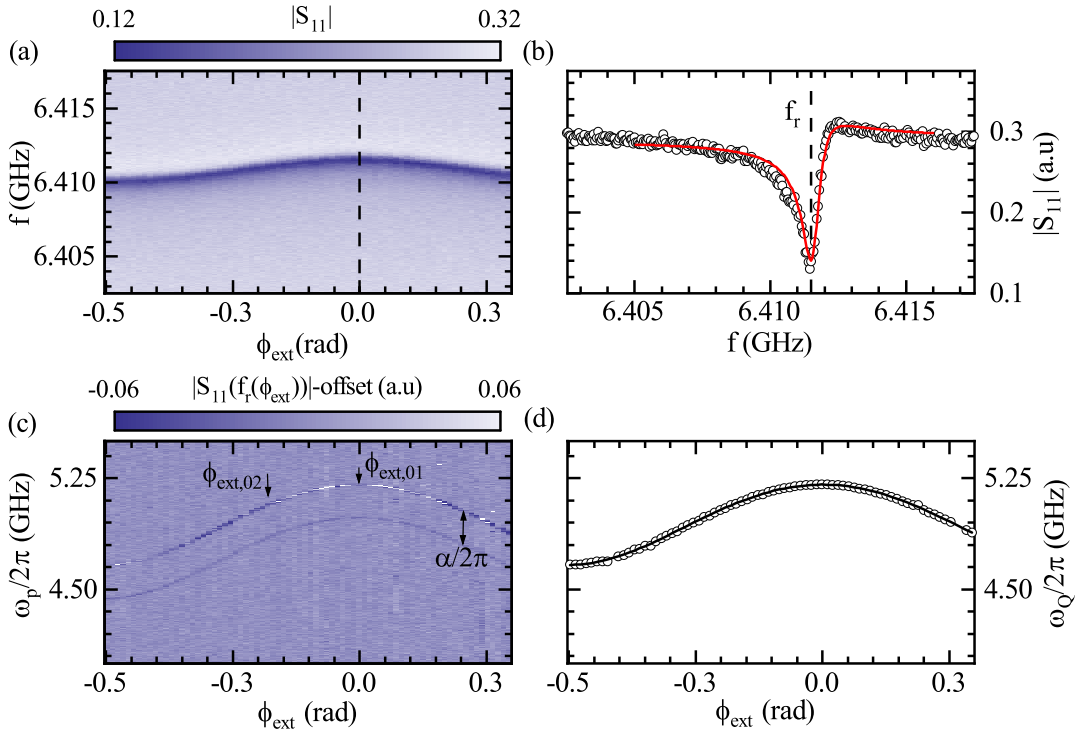

Figure 9.1.1: (a) single tone spectroscopy scattering parameter $|S_{11}|$ of the readout resonator for different external flux ϕ_{ext} in the SQUID of the qubit Q02. Resonance feature of the readout resonator is visible as darker color. When the qubit frequency $\omega_{\text{Q}}/2\pi$ is varied the qubit and resonator avoid one another and the dressed resonator frequency changes as well. (b) Linecut through (a) with flux $\phi_{\text{ext}} = 0$ (dashed line in (a)) and the resonance is fit using (2.11) (solid line). (c) two-tone spectroscopy of the qubit Q02 with varying external flux ϕ_{ext} in the asymmetric SQUID of the qubit in a colormap, where $|S_{11}(f_{\text{r}}|$ is color coded. The qubit frequency changes according to (5.4) and one can see the higher transition $f_{\text{ef}} = f_{\text{eg}} + \alpha$. (d) Qubit frequency $\omega_{\text{Q}}/2\pi$ for different flux values and a fit to equation 5.4 (solid line).

for the two-tone measurement can be found in Refs. [109, 110, 113]
Figure 9.1.1 (c) shows the colormap of a two-tone measurement on the qubit, where the reflection magnitude[1] $|S_{11}(\omega_{\text{r}})|$ is color coded, while we vary the flux in the SQUID of the transmon qubit with a dc-current through a coil and the pump frequency $\omega_{\text{P}}/2\pi$. The fundamental transition $\omega_{\text{eg}}/2\pi$ and higher order $\omega_{\text{ef}}/2\pi = \omega_{eg}/2\pi + \alpha/2\pi$ are visible as thin darker/brighter lines in front of the uniform background. The qubit is flux-tunable with an asymmetric SQUID and the qubit frequency as a function of the external flux $\omega_{\text{Q}}(\phi_{\text{ext}})$ follows the theory (see Subsec. 5.1.1). We extract the qubit frequency $\omega_{\text{Q}}/2\pi$ for the different flux values ϕ_{ext} with a Lorentzian fit and plot the results in Fig. 9.1.1 (d). We fit this qubit frequency to (5.4) with the flux-tunable $E_{\text{J},\Sigma}$ from (5.5) (solid line). From this fit we determine the critical current of the SQUID $I_{\text{c},\Sigma} = 2\pi E_{\text{J},\Sigma}/\Phi_0 = 33.4\,\text{nA}$, which is the sum of the critical currents of both

[1] There is an offset to the value – $|S_{11}|$ has no negative values.

junctions. Furthermore we can determine the asymmetry of the junctions to $\upsilon = 0.81$. For the symmetric SQUID qubit Q01 the qubit frequency $\omega_{\mathrm{Q,max}}/2\pi$ at the flux-sweetspot was too large and we determined $I_{\mathrm{c},\Sigma}$ to target the frequency 5 GHz for Q02 (see Chap. 7). This value is reasonably close to the value we determine from the experiment $\omega_{\mathrm{Q,max}} = 5.207\,\mathrm{GHz}$. The results for the qubit parameters are given in Tab. 9.1.1. While the qubit frequency is very close to the design value ($\pm 200\,\mathrm{MHz}$), the parameter υ for the asymmetry of the Josephson junctions from the experimental results differs from the design ($\upsilon = 0.51$). Next, we use the information encoded in the fluxmap to find suitable flux bias points which we use later for the time-domain measurements. The respective points $\phi_{\mathrm{ext,01}}$ at the sweet spot and $\phi_{\mathrm{ext,02}}$ are marked in the fluxmap. These bias points are of interest, because the qubit's susceptibility to flux-noise depends on the slope qubit frequency curve in Fig. 9.1.1 (d) [80]. At the sweetspot the susceptibility of flux-noise is reduced, while it is important for the qubit's coherence away from the sweetspot [80].

In order to determine the characteristic transmon level structure with the second transition

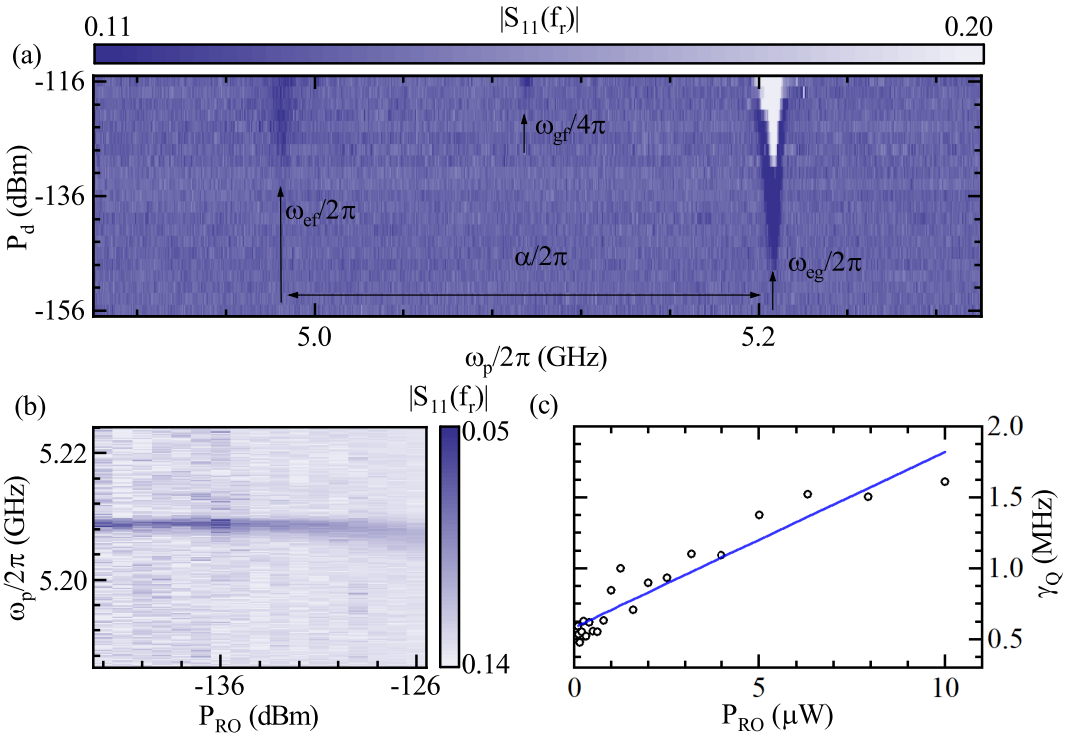

Figure 9.1.2: (a) two-tone spectroscopy of the qubit with different power P_{d} at the drive line of the qubit. The qubit transitions f_{ge}, $f_{\mathrm{ef}} = f_{\mathrm{ge}} + \alpha$ and the two photon transition f_{gf} appear for higher qubit drive power.(b) Colorplot fundamental qubit transition f_{01}, where $|S_{11}(f_{\mathrm{r}})|$ is color coded for varying power on the readout resonator P_{RO} and pump frequency $\omega_{\mathrm{p}}/2\pi$. (c) the linewidth of the transition in (b) for linear powers in the readout resonator.These measurements are performed on Q02 at the flux sweetspot $\phi_{\mathrm{ext,01}}$.

$\omega_{\mathrm{ef}} = \omega_{\mathrm{ge}} + \alpha/2\pi$ and extract $\alpha/2\pi$ we perform another two-tone measurement with different power P_{d} in the drive-tone that excites the qubit. In Fig. 9.1.2 (a) we show a color-plot of the

two-tone measurement, where amplitude of the signal, that is reflected at the resonator $|S_{11}(f_r)|$ at the resonance frequency is color coded for different drive powers P_d and pump frequency $\omega_p/2\pi$. The qubit is operated in the vicinity of the flux-sweetspot $\phi_{ext,01}$ for this two-tone measurement. The fundamental transition at the frequency $\omega_{ge}/2\pi = 5.207\,\mathrm{GHz}$ appears at the lowest power in the drive tone with as dark/bright line in Fig. 9.1.2 (a). There is significant power broadening for the resonance of the qubit for higher drive powers. The appearance of the qubit resonance in the $|S_{11}|$ signal changes from a dip to a peak for higher drive powers. The probable reason for this behaviour is, that the resonator frequency f_r was not set on the exact resonance frequency f_r of the readout resonator before the two-tone measurement. Furthermore the resonance frequency f_r could shift slightly as a function of the drive power P_d and we do not determine f_r individually for the different P_{RO}. In the heatmap the second transition appears as a dark line with frequency $\omega_{ef}/2\pi = 4.984\,\mathrm{GHz}$ appears for higher drive powers and we determine the anharmonicity $\alpha/2\pi = \omega_{ge}/2\pi - \omega_{ef}/2\pi = -E_C/h = -221.98\,\mathrm{MHz}$ by fitting a Lorentzian to the fundamental and second transition. The result for $\alpha/2\pi$ is listed in Tab. 9.1.1. The transition at the frequency $\omega_{gf}/4\pi = 5.094\,\mathrm{GHz}$ (dark line in between fundamental and second transitions) is excited in a two-photon process and therefore has the frequency difference of $\alpha/2$ from the fundamental transition.
Figure 9.1.2 (b) shows a similar two-tone measurement around the fundamental qubit transition at the flux-sweet spot $\phi_{ext,01}$, but this time we vary the power of the tone on the readout-resonator P_{RO}. The absolute value of the complex reflection $|S_{11}(f_r)|$ is color coded and the darker spots in the plot is the fundamental qubit transition. For larger P_{RO} the frequency of the qubit is shifted to a slightly lower frequency through the AC-Stark shift. We could alibrate the photon number in the readout resonator from this frequency shift [110]. The linewidth γ_Q of the qubit's resonance in the two-tone measurement increases with with higher readout power which is known as power broadening [110]. In Fig. 9.1.2 (c), we plot the linewidth γ_Q, that we extract by fitting a Lorentzian to the two-tone measurements, as a function of the linearized readout power P_{RO}. The qubit linewidth γ_Q shows a linear dependence on the readout power. Extrapolation to zero power yields the qubit linewidth $\gamma_{Q,0} = 0.58\,\mathrm{MHz}$, that is unaffected from the power broadening. The corresponding coherence time (we discuss these coherence times in more detail in Sec. 9.2) is defined as $T_2 = \gamma_Q^{-1}$ and the result is $T_2 = 1.71\,\mu\mathrm{s}$ [110]. We did not determine the coupling g between qubit and readout resonator directly, but using (5.7). We can determine everything but the coupling capacitance C_r from our results in Tab. 9.1.1. Ansys HFSS is used to determine the coupling capacitance $C_r = 6.46\,\mathrm{fF}$ and then $g = 91.5\,\mathrm{MHz}$. The qubit-resonator system is well in the strong coupling limit with $g \gg \gamma_{Q,0}, \kappa$. For the dispersive readout of the qubit state in the time-domain measurement, we determine the dispersive shift χ (see Subsec. 5.1.2) of the qubit on chip Q02 at the flux-sweetspot as $\chi = 6.96\,\mathrm{MHz}$ with the results in Tab. 9.1.1. The qubit-resonator system is in the dispersive limit with $\Delta = 1.2\,\mathrm{GHz}$.

9.2 Qubit in the Time Domain

Time-resolved measurements are crucial to detect the dynamics of the qubit and determine the time-scales (coherence times) on which the quantum information in the qubit state is lost because

[2] The cross capacitance coupling between Xmon and resonator C_r is determined with Ansys HFSS simulations.

Table 9.1.1: Results from the spectroscopy measurements on the qubits Q01 and Q02.

Qubit	Q01	Q02
$\omega_\mathrm{r}/2\pi$ (GHz)	6.53	6.41
κ (MHz)	10.19 ± 0.03	5.55 ± 0.17
Q_e (10^3)	4.2	9.6
Q_i (10^3)	81.8 ± 4.3	30.0 ± 3.7
$\alpha/2\pi$ (MHz)	-198.21 ± 0.76	-221.98 ± 1.31
$\omega_\mathrm{Q,max}/2\pi$ (GHz)	7.938	5.207
$I_{\mathrm{c},\Sigma}$ (nA)	84.1	33.4
υ	0	0.81
g (MHz)	–	91.5[2]

of disturbances [109]. The qubit is subject to decoherence which is the loss of information caused by the qubit's interaction with the environment [114]. Longitudinal relaxation Γ_1, i.e. the noise acts with $\hat{\sigma}^x$ or $\hat{\sigma}^y$ in a Hamiltonian, corresponds to the coherence time $T_1 = \Gamma_1^{-1}$. Typical processes are charge noise, photon absorption and spontaneous emission [114]. Dephasing with the rate Γ_ϕ captures noise which causes the qubit's frequency to shift, i.e. the noise acts with $\hat{\sigma}^z$ in the Hamiltonian [114]. Typical processes that cause this shift are for example magnetic field fluctuations (flux noise) or two-level systems [114]. The dephasing time $T_2 = \Gamma_2^{-1} = 1/(T_1/2 + \Gamma_\phi)$ can capture this contribution. The setup for the time-domain measurements was introduced in subsection 8.3.2. The pulse shapes for our readout and drive pulses are both rectangular and the power of the readout pulse of 3 µs duration has been calibrated before these measurements. We can determine these coherence times from Ramsey, Hahn-Echo and other measurements, but one needs to define a fundamental set of $\pi/2$ and π gates in order to rotate the qubit into the equal superposition and excited state respectively. In order to define these gates we need to start with a Rabi measurement. In many cases the length of the drive pulse determines the qubit state after the pulse – a $\pi/2$ pulse is half as long as a π pulse.[44] Here we perform power Rabi measurements which means the power P_d of the rectangular pulse that comes out of the arbitrary waveform generator (AWG) varies and the length of the gate is always 200 ns. The drive power P_d of this drive pulse is normalized with the pulse voltage $V_0 = 750\,\mathrm{mV}$, that comes out of the AWG. After we apply the single qubit gates with different powers, the excited state population $|c_1|^2$ of the qubit is read out with the readout-pulse as we illustrate in the insert in Fig. 9.2.1 (a). We plot the result of the Rabi measurement with Q02 at the flux-sweetspot in Fig. 9.2.1 (a). From a cosine fit we extract the power for a π pulse $P_{\mathrm{d},\pi} = 0.676 \pm 0.022$ and for a $\pi/2$ pulse $P_{\mathrm{d},\pi/2} = 0.338 \pm 0.011$. The same Rabi measurement can be performed for different drive frequencies around the qubit and we plot the results in a heatmap in fig. 9.2.1 (b). The dashed-blue line is the cut through the measurement at the qubit frequency $\omega_\mathrm{Q}/2\pi$, that is shown in (a). The qubit can only be excited when the frequency of the drive is in very close proximity to the qubit. With our fundamental gate set defined we want to understand the time-scales for which our qubit can store a quantum information.

We access the coherence time T_1 in the experiment in Fig. 9.2.2 (a). The qubit starts off in

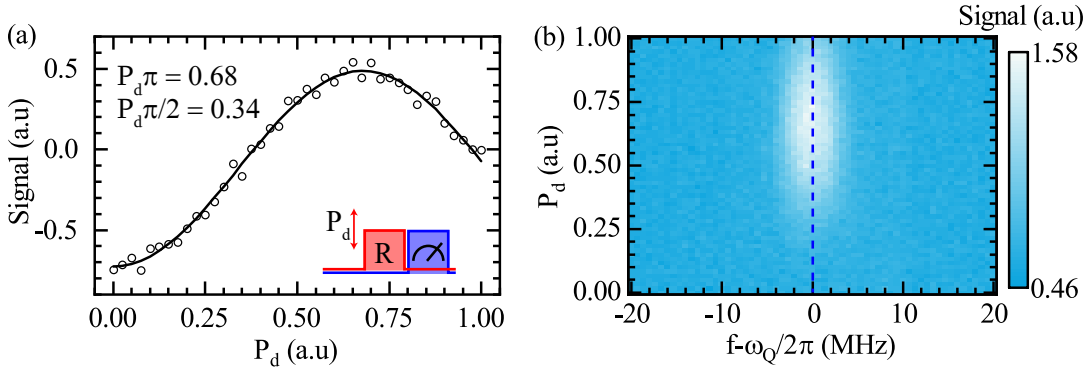

Figure 9.2.1: (a) Rabi measurement on the qubit Q02 at the flux-sweetspot $\phi_{\text{ext,01}}$. The inset shows the measurement protocol and the power of the drive pulse is varied. From the fit to a cosine the drive power necessary for π - and $\pi/2$-pulses is extracted.(b) Colormap of the Rabi in (a), where the signal is color coded, for different frequencies ± 20 MHz of the drive pulse around the qubit frequency.

the ground state $|g\rangle$ and is rotated to $|e\rangle$ using a ϕ pulse. Then we measure the qubit state after different times τ between the π- and readout pulse. The theory predicts

$$|c_1|^2 = e^{-\frac{\tau}{T_1}}, \tag{9.1}$$

with the excited state population $|c_1|^2$ for different times τ [114]. We plot the excited state population $|c_1|^2$ which is normalized with calibration points at small τ values in Fig. 9.2.2 (a). With the exponential decay we can fit the theoretical equation 9.1 and extract $T_1 = (0.867 \pm 0.031)\mu$s.

For the Hahn-Echo measurement the qubit is rotated with a $\pi/2$ pulse into the superposition

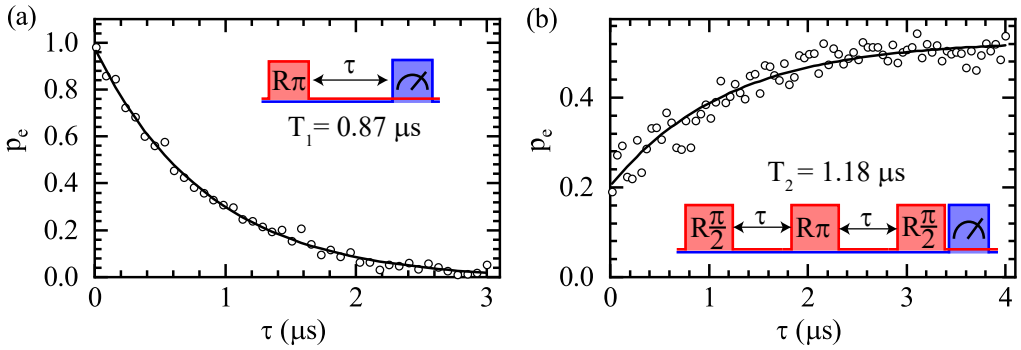

Figure 9.2.2: (a) Longitudinal decay at $\phi_{\text{ext,01}}$. The time-scale of the decay is described by the T_1 time that we extract with a fit to (9.1). (b) Hahn-Echo measurement of the qubit at $\phi_{\text{ext,01}}$. The time-scale for the dephasing in the Hahn-Echo measurement is set by T_2^*, which is extracted in a fit to (9.2). Insets show the measurement protocol.

state $(|g\rangle + |e\rangle)/2$. There the qubit dephases for τ and picks up a phase then the qubit state is refocused with a π pulse. Afterwards, the qubit dephases for the evolution time τ again. If the

disturbances, that cause the dephasing, are equal during the first and second evolution time τ,i.e. low frequency disturbances, the dephasing during the two evolution times cancels each other out. Then the qubit is rotated with a $\pi/2$ pulse before the application of the readout pulse. The theoretical excited state population for this gate sequence is

$$|c_1|^2 = \frac{1}{2}\left(1 - e^{-\frac{\tau}{T_2}}\right), \tag{9.2}$$

where T_2 is the time-scale on which the qubit looses the phase information, when we suppress the effect of low frequency disturbances. In Fig. 9.2.2 (b), we plot the result of the Hahn-Echo measurement, where the first few points are calibration points to calibrate $|c_1|^2$. The qubit is in the excited state after the measurement for small τ, while for large τ the qubit is in the completely dephased state and $|c_1|^2 = 1/2$. We fit this to the theory in (9.2) and determine $T_2 = (1.185 \pm 0.124)\mu s$. This result is significantly smaller than the result from the linewidth of the qubit resonance in a two-tone measurement ($T_2 = 1.71\,\mu s$) from Sec. 8.3.1.

The dephasing time T_2^* can be accessed directly in a Ramsey measurement. The qubit is

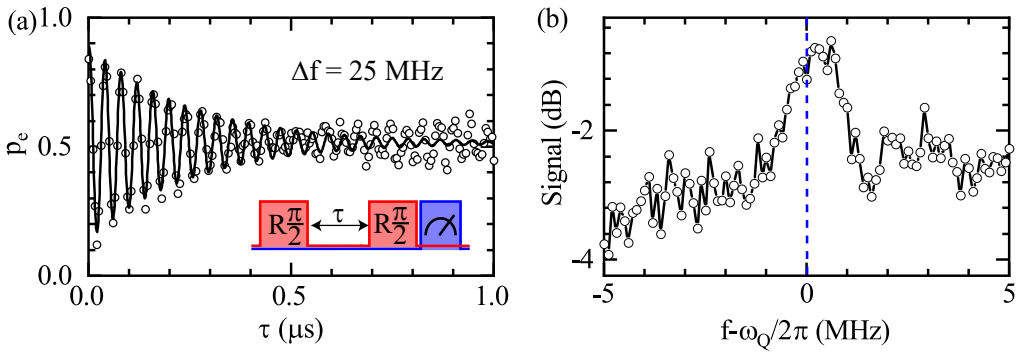

Figure 9.2.3: (a) Ramsey measurement, that is sensitive to low frequency dephasing noise. The T_2 time describes the time-scale for the loss of phase information. The oscillation on the envelope is usually caused by a frequency difference Δf between drive and actual qubit frequency. Δf is extracted from the fit to (9.3). (b) Two-tone measurement on the qubit with the time-domain setup with the peak close to the centre of the frequency span.

rotated with a $\pi/2$ pulse, then dephases for the time τ. After a subsequent $\pi/2$ pulse the qubit is read out with a measurement pulse. The theory for the excited state population in the Ramsey measurement with τ is

$$|c_1|^2 = e^{-\frac{\tau}{T_2^*}} \cos(2\pi\Delta f\tau), \tag{9.3}$$

where T_2^* is the dephasing time and Δf the frequency offset. In Fig. 9.2.3 (a) we plot the results of the Ramsey measurement. The excited state population $|c_1|^2$ decays with τ. In addition the signal exhibits a fast oscillation with $\Delta f = (25.39 \pm 0.04)$ MHz. The dephasing times is $T_2^* = (250 \pm 15)$ns. The fit is not in very good agreement with the result in Fig. 9.2.3 (a) for large τ and the signal decays not as quickly as the fit, because additional to the fast oscillation with frequency Δf, there is another slow oscillation. In many cases the Ramsey measurement can be used to determine the qubit frequency $\omega_Q/2\pi$ with higher accuracy, because Δf gives

Table 9.2.1: Results of the time-domain measurements on the different qubits Q01 and Q02 with two different flux-spots.

Qubit	Q01	Q02	Q02
flux bias	sweet spot	$\phi_{\text{ext,01}}$	$\phi_{\text{ext,02}}$
$w_{\text{Q}}/2\pi$ (GHz)	7.94	5.22	5.05
T_1 (μs)	0.206 ± 0.033	0.867 ± 0.031	0.827 ± 0.028
T_2 (μs)	–	1.18 ± 0.12	–

the frequency difference between the frequency of the drive and the real qubit frequency. This might be the slower oscillation in Fig. 9.2.3 (a). Figure 9.2.3 (b) shows a two-tone measurement in the frequency range around the drive frequency. The peak in the signal shows, that the qubit frequency and drive frequency are very close to one another – far closer than $\Delta f = 25.4\,\text{MHz}$. We believe there is a source for the disturbances with the frequency $\Delta f = 25.4\,\text{MHz}$ and suspect the superconducting coil, that is used to generate the magnetic field to tune the qubit frequency, is the cause for the disturbances. This superconducting coil and the cables leading to and from an LC-circuit that could oscillate the the frequency $\Delta f = 25.4\,\text{MHz}$. The actual detuning of the drive from the qubit frequency might be the beat in the excited state population that can be seen in Fig. 9.2.3 (a).
In Tab. 9.2.1, we summarize the results from our time-domain measurement not only for Q02 at $\phi_{\text{ext,01}}$, but also for the other flux point. For completeness we give the results for Q01 at the flux sweet-spot as well. It seems sensible that the coherence time T_1 for the Q01 is smaller, because due to the high frequency the qubit is closer to box-modes in our packaging. The T_1 time for Q02 at the other flux-spot $\phi_{ext,02}$ is very similar to T_1 at the sweet-spot, because the added flux-noise leads to dephasing and has only influence on T_2.

9.3 Conclusion and Outlook

The contents of the cQAD part of this thesis can be summarised into two main points.
First of all we fabricated flux-tunable Xmon qubits coherence times ($T_1 = 1.18\,\mu\text{s}$) which are acceptable for cQAD – Ref.[19] had a relaxation time of $T_1 = 46\,\text{ns}$. Our coherence times ($T_1 = 1.18\,\mu\text{s}$) are however far off from the state of the art for superconducting Xmon qubits on a Si substrate [23, 79]. Possible reasons for the low coherence times are flux noise, two-level systems and Purcell limitation through the interaction of the qubit with low-Q standing wave modes in our qubit packaging (see Fig. 8.3.1 (a)) [114]. In the future the sensitivity to flux noise can be reduced with $5\,\text{k}\Omega$ series resistor in the circuit for the flux-bias and with a low pass filter inside the fridge. The resistor dampens the LC circuit, that is formed with the superconducting coil. Another qubit package with smaller mode volume could push the frequency of these standing wave modes in the qubit package to higher frequencies and thereby increase our coherence times [114]. Furthermore we discussed two different methods to indirectly couple a SAW resonator to a qubit and avoid the piezoelectric substrate for the qubit: (i) SAW resonator on a multi-layer substrate, where the piezoelectric layer is etched away below the superconducting qubit and

wiring and (ii) a flip-chip geometry, where SAW resonator and qubit are on different chips. We pursued the option for the flip-chip geometry and developed a design (see chapter 7) to couple the qubit and SAW resonator with an inductive coupler. In the future the indirect coupling resonator should be flux-tunable to be reap the benefits of the giant-atom limit. In the current configuration the indirect coupling strength $\mathcal{J}$ consists in part of the direct coupling strength g between the IDT of the SAWR and the CPWR. The giant-atom limit predicts, that this coupling rate g is frequency dependent, however since the frequency of the CPWR is constant the frequency dependence cannot be accessed [20]. A good orientation should be the flux-tunable waveguide extender from Refs. [94, 115]. In the future new machines at the WMI, such as the new RIE and flip-chip bonder will allow more work on both methods.

Chapter 10

Conclusion and Outlook

Within the scope of this thesis, we investigate SAW resonators on bulk lithium niobate (LNO), Si-SiO_x-LNO and Si-LNO multi-layer substrates. In particular we determine important properties of the resonator, such as single electrode reflectivity r, center-frequency of the stop-band f_c and SAW propagation velocity v and compare them to results obtained from Finite Element simulations. Furthermore, we relate the external quality factors Q_e for SAW resonators on LNO (bulk) and the Si-LNO multi-layer system to the model presented in Sec. 2.6. While there is good agreement for the dependence on geometric parameters of the resonator, the agreement with the full theory in (2.37) is not good. Thus, Q_e becomes now a design parameter not only on bulk LNO, but also on the more complex substrate. Our main focus, however is on the intrinsic quality factor Q_i of the resonators, which is a measure of the losses in the resonators and represents a critical parameter for quantum applications. The internal quality factors Q_i of the resonators on the multi-layer substrates are lower than for LNO (bulk), but they remain on the same order of magnitude. For further insight into the the loss channels we employed power- and temperature dependent measurements and in particular investigate the impact of two-level systems (TLS) coupling to the SAW resonators. We use a TLS model established for superconducting microwave resonators, which describes the experimental results very well. This model allows to quantify the contribution of these TLS to the losses of the resonators for the different substrate materials. The comparison between the LNO (bulk) and multi-layer substrates suggests, that the wafer-bonding process, which is used during the fabrication process of the substrates, introduces a large number of TLS. As a consequence, the performance in the low power limit with only a few phonons in the resonator is limited to $Q_{i,LP} = 3.0 \times 10^3$ for LNO-SiO_x-Si and $Q_{i,LP} = 14.0 \times 10^3$ for LNO-Si in comparison with the resonators on LNO (bulk) ($Q_{i,LP} = 45.7 \times 10^3$) by coupling to the TLS. From investigations/studies performed on superconducting microwave resonators it is know, that silicon oxides are a source of large TLS related losses [68]. Our results indicate that SAW resonators show a similar behaviour.

In the second part of the thesis, we explore the viability of the bulk and multi-layer substrates for SAW applications in the context of circuit quantum acoustodynamics (cQAD) [116]. We discuss two different methods for the coupling of SAW resonators on LNO (bulk) and Si-LNO multi-layer to a superconducting qubit, while avoiding the lossy piezoelectric for the qubit (see Chap 6). For the resonator prepared on the multi-layer substrate this includes a selective etch step to remove the LNO layer from the locations where the superconducting circuit components are fabricated in a later step. In a second approach we test a flip-chip assembly pursuing the same goal. We design a qubit chip on silicon and a SAW resonator chip on bulk LNO (see Chap. 7) and fabricate both of them. We measure the performance of the qubit circuit quantum

electrodynamics (cQED) chip, putting emphasis on the coherence times of the qubit. Our coherence times are $T_1 = 0.87\,\mu s$ and $T_2 = 1.18\,\mu s$ and thus lower than the state-of-the-art. However we note that this qubit performance is already sufficient for initial experiments using simple gate operations. We discuss possible explanations for the limited coherence. While both individual components of the flip chip package were successfully fabricated, final assembly could not be realized, due to time-constraints.

We give an outlook for possible future directions. Our study suggests that SAW resonators operating at 4-5 GHz are limited by the free phonon propagation length l_P, which is proportional to f_r^{-3} with the frequency f_r of the resonator [45]. Therefore, it might be interesting to survey the performance of a SAW resonator at lower frequencies ~ 1 GHz, because at this frequency other contributions, such as diffraction might become relevant. We believe significant increases for Q_i can be achieved at lower frequencies and the right diffraction-free substrate, e.g. Y-Z cut LNO [2]. Diffraction free propagation directions for multi-layer substrates can be straightforwardly determined in the future from the Finite Element simulations using the methods established in this work. For these low frequencies novel low frequency qubit architectures, such as the fluxonium qubit might be of interest [117, 118]. Grooves for the mirrors instead of metal electrodes and recessed transducer electrodes can help reduce unwanted reflections and mechanical loading [119]. The following infrastructure would be highly beneficial for this project: (i) A vapor-phase HF for the dry chemical etching of LNO and (ii) a flip-chip bonder, for the precise alignment of the Si and LNO chip.

Lithium niobate can be chemically etched using hydroflouric acid [120]. A vapor-HF system would also allow for removing the SiO_x layer within the Si-SiO_x-LNO substrate to release a freely suspended thin-film LNO resonator. By choosing the etching conditions correctly, this etching step can also be performed in a selective fashion so that the LNO layer remains intact [121]. This is likely to reduce or even eliminate losses to bulk waves. However, the performance of this type of resonator has not been investigated yet [122]. In addition, the selective HF etch of surface oxides, while not attacking the LNO can also be helpful for surface cleaning processes for the cQAD version on the Si-LNO multi-layer. One advantage of this technique is that liquid HF processes etch aluminium. In contrast, the HF vapor-phase process does not etch aluminium and can be useful for a post-fabrication removal of surface oxides for the qubit chip, while the Al/AlO_x/Al junctions are not damaged [123, 124]. A specialized flip-chip bonder should reliably provide parallel alignment of the two chips during assembly and indium bump bonds provide a common ground for the two chips [99].

For the future, the indirect coupler between the SAW resonator and qubit should be flux-tunable [88, 94]. Then the interaction between SAW resonator and the flux-tunable coupler can be changed with the frequency of the tunable element and the effects of the giant-atom limit, i.e. frequency dependent coupling rate, are harnessed [20, 21]. This flux-tunable element could be partially on a piezoelectric substrate and subject to very high electric field densities at the IDTs, which decreases its coherence times [88]. The main question is to determine the fidelity for insertion of the qubit state into the SAW resonator. Then the next step is to scale up the system to two qubits, e.g. by braiding their IDTs, that couple them to the cavity and demonstrate decoherence free interaction between the two artificial atoms [20, 22].

Appendix A

Further Calculations and Relations

A.1 Partial Waves Method for Surface Acoustic Waves

We give more details for the partial waves method for the calculation of SAWs, which was mentioned in Sec. 2.1. Some of the calculations have been implemented in Python and we show excerpts of this code in this section. In order to talk about SAWs with different propagation directions, we first need to implement the Euler rotations from Sec. 2.3 in Python. Then we discuss how to solve the SAW problem itself.

A.1.1 Euler rotations

Euler rotations in the Z-X-Z notation described in Sec. 2.3 rely on the rotation matrix V with the Euler angles α, μ and ν, which is just a concatenation of the common rotation matrices. In order to shorten the notation we write $\cos(\alpha) = c_\alpha$ and $\sin(\nu) = s_\nu$. Then the rotation matrix V is given by

$$V = \begin{pmatrix} c_\alpha c_\nu - s_\alpha c_\mu s_\nu & c_\alpha s_\nu + s_\alpha c_\mu c_\nu & s_\alpha s_\mu \\ -s_\alpha c_\nu - c_\alpha c_\mu s_\nu & -s_\alpha s_\nu + c_\alpha c_\mu c_\nu & c_\alpha s_\mu \\ s_\mu s_\nu & -s_\mu c_\nu & c_\mu \end{pmatrix}. \tag{A.1}$$

The stiffness tensor is rotated by

$$C'_{ijkl} = V_{im} V_{jh} V_{kb} V_{le} C_{mhbe}, \tag{A.2}$$

where we contract over indices m, h, b, e that appear twice. Similar relations hold true for the other tensors such as the piezoelectric tensor $\mathbf{e}$ and $\boldsymbol{\varepsilon}$ as variables. In order to implement this procedure in Python we write a class **material** with the tensors $\mathbf{C}$, $\mathbf{e}$, $\boldsymbol{\varepsilon}$ and the density ρ. For the contraction the tensors must the in the normal notation, while in general the Voigt notation is more common. Therefore we implement functions that translate between the two notations, e.g. **bumrechungCp**.

```
1 class material:
2     def __init__(self,C,e,eps,rho,piezoelectric=True):
3         self.C = C
4         self.e = e
5         self.eps=eps
6         self.rho = rho
7         self.Cn = self.bumrechungCp()
8         self.en = self.bumrechungep()
```

```
9           self.ispiezoelectric = piezoelectric
10      @staticmethod
11      def generalrotation(alpha,beta,gamma,M):
12          V = np.array([[...],[...],[...]])
13          gg = np.outer(V,V)
14          gggg = np.outer(gg,gg).reshape(4*V.shape)
15          M = 2*np.tensordot(gggg,M,axes=((1,3,5,7),(0,1,2,3)))
16          return M
```

The function **generalrotation** defines the matrix V and then contracts the indices according to (A.2) to calculate the stiffness matrix in the rotated coordinate system. Similar functions exist for the other material properties.

A.1.2 Solution to the fundamental equations

In order to solve the SAW problem we write the class **surfaceacoustics**, which has has a variable for a velocity interval (a,b,c) – this use of this interval will become apparent later on. When we insert (2.7) and (2.6) into (2.4) and (2.5) the new problem is a matrix equation given by

$$\begin{pmatrix} F_{11}-\rho v^2 & F_{12} & F_{13} & F_{14} \\ F_{12} & F_{22}-\rho v^2 & F_{23} & F_{24} \\ F_{13} & F_{23} & F_{33}-\rho v^2 & F_{34} \\ F_{14} & F_{24} & F_{34} & F_{44} \end{pmatrix} \begin{pmatrix} \alpha_1 \\ \alpha_2 \\ \alpha_3 \\ \alpha_4 \end{pmatrix} = 0. \tag{A.3}$$

The components, which couple the elastic displacements components between one another is given by [25]

$$\begin{aligned} F_{11} &= c_{55}b^2 + 2c_{15}b + c_{11} \\ F_{22} &= c_{44}b^2 + 2c_{46}b + c_{66} \\ F_{33} &= c_{33}b^2 + 2c_{35}b + c_{55} \\ F_{12} &= c_{45}b^2 + (c_{14}+c_{56})b + c_{16} \\ F_{13} &= c_{35}b^2 + (c_{13}+c_{55})b + c_{15} \\ F_{23} &= c_{34}b^2 + (c_{36}+c_{45})b + c_{56}. \end{aligned}$$

The Fs in the upper-right and lower-left block couple the potential Φ to the components of elastic displacements are given as [25]

$$\begin{aligned} F_{14} &= e_{35}b^2 + (e_{15}+e_{31})b + e_{11} \\ F_{24} &= e_{34}b^2 + (e_{14}+e_{36})b + e_{16} \\ F_{34} &= e_{33}b^2 + (e_{13}+e_{35})b + e_{15} \end{aligned}$$

and the electric term in the lower right corner is given as

$$F_{44} = -(\varepsilon_{33}b^2 + 2\varepsilon_{13}b + \varepsilon_{11}).$$

All of these components depend on the complex parameter b, that determines the phase and amplitude variation with depth. To solve the problem in (A.3) the determinant of the matrix must vanish. The determinant is an eight order polynomial in the parameter b and one can find eight solutions in b, such that the determinant vanishes. This is implemented with the function **polynomial**, that calculates the total polynomial based on the material parameters of an object of the material class that we discussed before, and returns the eight solutions for b. As we mention in Sec. 2.1 only solutions in (2.6)-(2.7), that vanish in the substrate for $z \to \infty$ are valid solutions. This leaves only four valid solutions in b. We do not show the Python function, that sorts out invalid b solutions, here. When we put the valid b solutions into $A.3$ the resulting problem is an eigenvalue problem with the eigenvalue 0. Therefore we solve the eigenvalue problem with the function **solver**. This function returns the smallest value eigenvector. However, there are always four solutions for b and therefore four corresponding eigenvectors $\vec{\alpha}$.

```
import numpy.polynomial as poly
import numpy as np
from scipy.linalg import null_space
from scipy import constants
from scipy.optimize import golden
class surfaceacoustics:
    def __init__(self,v,kh,angle):
        self.v = v # tuple (a,b,c) for the golden section
    @staticmethod
    def polynomial(v,obj):
        Ga11,... = poly.Polynomial([obj.C[0,0]-obj.rho*v**2,
        2*obj.C[0,4],obj.C[4,4]]),...
        determinantpolynomial = (Ga14**2*Ga23**2-...)
        return determinantpolynomial.roots()

    @staticmethod
    def solver(v,sol,obj):
        Ga11,... = poly.Polynomial([obj.C[0,0]-obj.rho*v**2,
                                    2*obj.C[0,4],obj.C[4,4]]),...
        Ga11,... = Ga11(sol),...
        #calculate the determinant of a symmetric 4x4 matrix.
        M = np.array([[Ga11,Ga12,Ga13,Ga14],
                      [Ga12,Ga22,Ga23,Ga24],
                      [Ga13,Ga23,Ga33,Ga34],
                      [Ga14,Ga24,Ga34,Ga44]])
        x = null_space(M,rcond=None)
        return x[:,0]
```

A.1.3 Boundary conditions

Now we insert these eigenvectors $\vec{\alpha}$, and solutions for b (2.6)-(2.7) into the four boundary conditions, three mechanical and one electric. The result is another matrix problem with the matrix M and the relative amplitude of the partial waves $\vec{C}$ with the four components. This matrix M is very complex and we refer to Ref.[25] for the entries. For a SAW solution the determinant

of the matrix M has to vanish. Note, that now the only variable that we did not specify is the velocity v, which appears in (A.3). The velocity, where $det(M) = 0$ is the solution where a SAW solution exists with the frequency v_{SAW}. We plot the absolute value of the determinant of the matrix M in Fig A.1.1 as an example. We can see clearly that there is a minimum in this interval, where $det(M) = 0$. In the code the calculation of the determinant is done by the function **bulkmaterialsurfaceacousticwavedetvalgolden**. How can we determine this v_{SAW} in

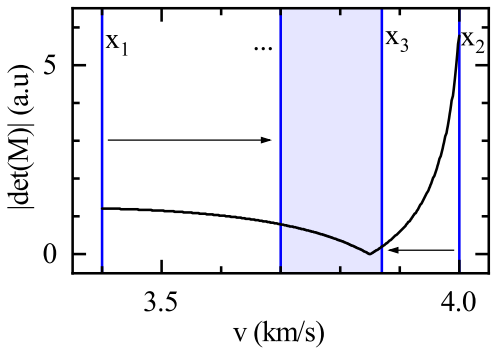

Figure A.1.1: Absolute value of the determinant of the boundary condition matrix M for different velocities. We illustrate the golden section search, which makes the interval smaller an can thereby determine the minimum with the solution v_{SAW}.

an efficient way? The answer is the golden section algorithm [125]. Here the velocity interval (a,b,c) plays an important role. In essence the golden section search works by comparing the two function values $det(M)$ at the velocities a and c. On whichever side of the interval $det(M)$ is larger, the interval shrinks in order to get closer to the minimum. When this is repeated multiple times the result converges quickly to the SAW velocity. This is implemented with the function **bulkgoldensearch**. From the b parameters, the eigenvectors $\vec{\alpha}$ and partial waves amplitudes $\vec{C}$ the total SAW solutions can be calculated by inserting this into (2.6)-(2.7).

```
1     def bulkmaterialsurfaceacousticwavedetvalgolden(self,
2     vel,obj,mode='free'):
3         sol = self.polynomial(vel,obj)
4         soln = self.solfinder(sol)
5         beta = soln
6         alpha = []
7         for j in range(len(soln)):
8             vec = self.solver(vel,beta[j],obj)
9             alpha.append(vec)
10        alpha = np.array(alpha)
11        detval=np.abs(np.linalg.det(self.boundaryconmatrix(beta=beta,
12        alpha=alpha,obj=obj,mode=mode)))
13        return detval
14    def bulkgoldensearch(self,obj,mode='free'):
15        a,b,c = self.v
16        vmin = golden(self.bulkmaterialsurfaceacousticwavedetvalgolden,
17        args=(obj,mode),brack=self.v,tol=1e-10)
18        return vmin
```

A.2 Resonator Fit Model

The function that describes the scattering parameter $S_{11}(f)$ in the vicinity of the resonance of a SAW resonator is given by [19]

$$S_{11}(f) = \frac{(Q_\mathrm{e} - Q_\mathrm{i})/Q_\mathrm{e} + 2iQ_\mathrm{i}(f - f_\mathrm{r})/f}{Q_\mathrm{e} + Q_\mathrm{i})/Q_\mathrm{e} + 2iQ_\mathrm{i}(f - f_\mathrm{r})/f}. \tag{A.4}$$

We define the loaded quality factor:

$$\frac{1}{Q} = \frac{1}{Q_\mathrm{e}} + \frac{1}{Q_\mathrm{i}} \Rightarrow Q_\mathrm{i} = \frac{1}{\frac{1}{Q} - \frac{1}{Q_\mathrm{e}}} = \frac{Q_\mathrm{e}Q}{Q_\mathrm{e} - Q}$$

We insert this into (A.4) with $\delta f = f - f_\mathrm{r}$ and substitute all Q_i entries.

$$\begin{aligned} S_{11}(f) &= \frac{1 - \frac{Q}{Q_\mathrm{e}-Q} + 2i\frac{QQ_\mathrm{e}}{Q_\mathrm{e}-Q}\frac{\delta f}{f}}{1 + \frac{Q}{Q_\mathrm{e}-Q} + 2i\frac{QQ_\mathrm{e}}{Q_\mathrm{e}-Q}\frac{\delta f}{f}} = \frac{Q_\mathrm{e} - 2Q + 2iQQ_\mathrm{e}\frac{\delta f}{f}}{Q_\mathrm{e} + 2iQQ_\mathrm{e}\frac{\delta f}{f}} \\ &= \frac{1 - \frac{2Q}{Q_\mathrm{e}} + 2iQ\frac{\delta f}{f}}{1 + 2iQ\frac{\delta f}{f}} = \left(1 - \frac{2\frac{Q}{Q_\mathrm{e}}}{1 + 2iQ\frac{\delta f}{f}}\right) \end{aligned}$$

$e^{i\theta_\mathrm{f}}$ is introduced with $Q_\mathrm{e} = |Q_\mathrm{e}|e^{i\theta_\mathrm{f}}$ compensating for mismatches between input- and output impedance as well as reflection paths in parallel to the resonator. We introduce the environmental factors $Ae^{i\phi_\mathrm{f}}e^{-2\pi i f\tau}$ with the global amplitude factor A, the electric delay of the cables τ, where the latter two parameters account for the uncalibrated reflection measurement [36, 37].

$$S_{11}(f) = Ae^{i\phi_\mathrm{f}}e^{-2\pi i f\tau}\left(1 - \frac{2\frac{Q}{Q_\mathrm{e}}e^{i\theta_\mathrm{f}}}{1 + 2iQ\frac{\delta f}{f}}\right) \tag{A.5}$$

A.3 Material Properties at Cryogenic Temperatures

In order to calculate or simulate the SAW properties, such as phase velocity v_free, we need the elastic constants, such as the stiffness tensor $\mathbf{C}$, piezoelectric tensor $\mathbf{e}$, dielectric tensor $\boldsymbol{\varepsilon}_\mathrm{r}$ and density ρ of the material on which the SAW propagates. These properties are temperature dependent and there is a lack of data on these properties for cryogenic temperatures on lithium niobate. Therefore we extrapolate these properties linearly for lithium niobate with the results from Ref.[64] and for silicon from Ref.[72] for $T = 1\,\mathrm{K}$.

A.3.1 Lithium niobate

For lithium niobate reference values X_{ref} for the parameters at $T = 298.15\,\text{K}$ are given in Ref.[64]. They also list the linear extrapolation parameters a_1 for a linear extrapolation with

$$X = X_{\text{ref}} \left(1 + \sum_{n=1}^{N} a_n (\Delta T)^n \right), \tag{A.6}$$

where for a linear extrapolation the sum stops at $N = 1$ and ΔT is the temperature difference between the reference temperature and the temperature we want to extrapolate the elastic properties to. Since $LiNbO_3$ is a crystal from the crystal class $3m$ the number of independent components in the stiffness tensor $\mathbf{C}$ is reduced to 6 and in the Voigt notation the stiffness tensor has the form [64]

$$\mathbf{C} = \begin{pmatrix} c_{11} & c_{12} & c_{13} & c_{14} & 0 & 0 \\ c_{12} & c_{11} & c_{13} & -c_{14} & 0 & 0 \\ c_{13} & c_{13} & c_{33} & 0 & 0 & 0 \\ c_{14} & -c_{14} & 0 & c_{44} & 0 & 0 \\ 0 & 0 & 0 & 0 & c_{44} & c_{14} \\ 0 & 0 & 0 & 0 & c_{14} & c_{66} \end{pmatrix}. \tag{A.7}$$

Here $c_{66} = (c_{11} - c_{12})/2$ is not a independent component. When we extrapolate these components with the results from Ref.[64] to $T = 1\,\text{K}$ with $\Delta T = 297.15\,\text{K}$ we get the results in Tab. A.3.1 for the components of the stiffness tensor. The piezoelectric tensor e has 4 independent coefficients for the crystal class $3m$ and in the Voigt notation has the form:

Table A.3.1: Elastic tensor components c_{ij} for lithium niobate at cryogenic temperature ($T = 1\,\text{K}$) interpolated on the basis of the results from [64].

components	c_{11}	c_{12}	c_{13}	c_{14}	c_{33}	c_{44}	c_{66}
$(10^{11} \times \text{N/m}^2)$	2.135	0.616	0.788	0.090	2.534	0.631	0.756

$$\mathbf{e} = \begin{pmatrix} 0 & 0 & 0 & 0 & e_{15} & -e_{22} \\ -e_{22} & e_{22} & 0 & e_{15} & 0 & 0 \\ e_{31} & e_{31} & e_{33} & 0 & 0 & 0 \end{pmatrix}. \tag{A.8}$$

We extrapolate the results from Ref.[64] in a similar way as before for the components of the piezoelectric tensor and give the results in Tab. A.3.2. In the same way the extrapolate for the

Table A.3.2: Piezoelectric tensor components e_{ij} for lithium niobate at cryogenic temperature ($T = 1\,\text{K}$) interpolated on the basis of the results from [64].

components	e_{15}	e_{22}	e_{31}	e_{33}
(C/m^2)	3.596	2.373	0.215	0.979

components of the dielectric tensor and we get $\varepsilon_{11} = 39.91$ and $\varepsilon_{33} = 22.70$, which leads to the dielectric tensor

$$\boldsymbol{\varepsilon}_\mathrm{r} = \begin{pmatrix} \varepsilon_{11} & 0 & 0 \\ 0 & \varepsilon_{11} & 0 \\ 0 & 0 & \varepsilon_{33} \end{pmatrix}. \tag{A.9}$$

For a hexagonal lattice as $LiNbO_3$ there are two lattice constants $\tilde{a}$ and $\tilde{c}$. The volume of an unit cell in a hexagonal crystal is $V = \tilde{a}^2\tilde{c}3^{1/2}1/2$ [27]. We adjust for the density ρ with the linear and quadratic extrapolation of the lattice constants $\tilde{a}$ and $\tilde{c}$ in Ref.[64] and then determine the new density at the cryogenic temperature $\rho_{\mathrm{T=1\,K}} = V_\mathrm{ref}\rho_\mathrm{ref}/V_{\mathrm{T=1\,K}} = 4678\,\mathrm{kg/m^3}$.

A.3.2 Silicon

For silicon reference values at $T = 300\,\mathrm{K}$ and linear extrapolation constants are given in Ref.[72]. The stiffness tensor in the Voigt notation is:

$$\mathbf{C} = \begin{pmatrix} c_{11} & c_{12} & c_{12} & 0 & 0 & 0 \\ c_{12} & c_{11} & c_{12} & 0 & 0 & 0 \\ c_{12} & c_{12} & c_{11} & 0 & 0 & 0 \\ 0 & 0 & 0 & c_{44} & 0 & 0 \\ 0 & 0 & 0 & 0 & c_{44} & 0 \\ 0 & 0 & 0 & 0 & 0 & c_{44} \end{pmatrix}, \tag{A.10}$$

where there are only three independent components because of the cubic crystal symmetry [72]. Linear extrapolation for $T = 1\,\mathrm{K}$ yields the components in Tab. A.3.3. Silicon is not piezoelectric and therefore we do not give results for the piezoelectric tensor e, which is just a tensor with zeros as entries. The dielectric tensor for a cubic material is given as

Table A.3.3: Elastic tensor components c_{ij} for silicon at cryogenic temperature ($T = 1\,\mathrm{K}$) interpolated on the basis of the data from Ref.[72].

components	c_{11}	c_{12}	c_{44}
$(10^{11} \times \mathrm{N/m^2})$	1.703	0.658	0.815

$$\boldsymbol{\varepsilon}_\mathrm{r} = \begin{pmatrix} \varepsilon_{33} & 0 & 0 \\ 0 & \varepsilon_{33} & 0 \\ 0 & 0 & \varepsilon_{33} \end{pmatrix} \tag{A.11}$$

, where $\varepsilon_{33} = 11.45$ for silicon at cryogenic temperatures. For the density we proceed in the same fashion as for lithium niobate, but for the cubic system there is only a single lattice constant $\tilde{a}$ and the volume of the cubic lattice unit cell is $V = \tilde{a}^3$. For silicon at cryogenic temperatures we get the density $\rho = 2335\,\mathrm{kg/m^3}$ with the constants from Ref[72].

A.4 Inductive Coupling

$$\mathcal{L} = \frac{C_1}{2}\phi_1^2 + \frac{C_2}{2}\phi_2^2 - \frac{1}{2}\begin{bmatrix} I_1 I_2 \end{bmatrix}\begin{bmatrix} \Phi_1 \\ \Phi_2 \end{bmatrix} \tag{A.12}$$

$$\begin{bmatrix} \Phi_1 \\ \Phi_2 \end{bmatrix} = \begin{bmatrix} L_1 M \\ M L_2 \end{bmatrix}\begin{bmatrix} I_1 \\ I_2 \end{bmatrix} = \mathbf{L}\vec{I} = \vec{\Phi} \tag{A.13}$$

$$\Rightarrow \vec{I} = \mathbf{L}^{-1}\vec{\Phi} = \frac{1}{L_1 L_2 - M^2}\begin{bmatrix} L_2 & -M \\ -M & L_1 \end{bmatrix}\vec{\Phi} \tag{A.14}$$

$$Q_i = \frac{\partial \mathcal{L}}{\partial \dot{\Phi}_i} \Rightarrow \vec{Q} = \mathbf{C}\vec{\Phi} \tag{A.15}$$

Then we can calculate the Hamiltonian $\mathcal{H}$.

$$\mathcal{H} = \frac{1}{2}\vec{Q}^T\mathbf{C}^{-1}\vec{Q} + \frac{1}{2}\vec{\Phi}^T\mathbf{L}^{-1}\vec{\Phi} \tag{A.16}$$

The frequencies of the two resonators get re scaled through the interaction.

$$\omega_1 = \frac{L_2}{L_1 L_2 - M^2}\frac{1}{C_1} \;\&\; \omega_2 = \frac{L_1}{L_1 L_2 - M^2}\frac{1}{C_2} \tag{A.17}$$

The Hamiltonian is rewritten in single and interaction terms and changed to the usual operator notation.

$$\hat{\mathcal{H}} = \frac{1}{2}\frac{\hat{Q_1}^2}{C_1} + \frac{1}{2}\frac{\hat{Q_2}^2}{C_2} + \frac{1}{2}\hat{\Phi_1}^2\omega_1^2 C_1 + \frac{1}{2}\hat{\Phi_2}^2\omega_2^2 C_2 - \frac{M}{\sqrt{L_1 L_2}}\omega_1\omega_2\hat{\Phi_1}\hat{\Phi_2} \tag{A.18}$$

The interaction term reads the following

$$\hat{V} = -\frac{M}{\sqrt{L_1 L_2}}\omega_1\omega_2\hat{\Phi_1}\hat{\Phi_2}. \tag{A.19}$$

With the typical circuit quantization:

$$\hat{Q}_{1,2} = Q_{\text{ZPF-1,2}}(\hat{a}_{1,2} - \hat{a}_{1,2}^\dagger) \;\&\; \hat{\Phi}_{1,2} = -i\Phi_{\text{ZPF-1,2}}(\hat{a}_{1,2} + \hat{a}_{1,2}^\dagger) \tag{A.20}$$

$$\hat{V} = \hbar g(\hat{a}_1 + \hat{a}_2^\dagger)(\hat{a}_2 + \hat{a}_1^\dagger) \tag{A.21}$$

Then the coupling g is given

$$g = \frac{1}{4}\sqrt{Z_1 Z_2}\omega_1\omega_2\frac{M}{\sqrt{L_1 L_2}}. \tag{A.22}$$

Appendix B

Sample Fabrication Recipes

SAW resonator fabrication

We give the details for our fabrication of the SAW resonators on the different substrates here.

1. Clean the blank lithium niobate (LNO) or multi-layer thin film with the ultrasonic bath for two minutes each in acetone (technical, room temperature), p.a. acetone ($70\,^{\circ}\mathrm{C}$), p.a isopropyl alcohol (IPA) ($70\,^{\circ}\mathrm{C}$) and IPA (room temperature). Dry with N_2 and then bake the sample on the hotplate for one minute ($200\,^{\circ}\mathrm{C}$).

2. Spin-coat the sample with $50\,\mu\mathrm{l}$ of AR-P 6200.09 at $4000\,\mathrm{RPM}$ for $1\,\mathrm{min}$, apply gold nano-particles to the edges of the chip and subsequently bake the sample at $150\,^{\circ}\mathrm{C}$ for $1\,\mathrm{min}$.

3. For the LNO samples we need an additional spin-coat with $40\,\mu\mathrm{l}$ of the conductive resist AR-PC 5091.02 (Electra 92) at $4000\,\mathrm{RPM}$ for $2\,\mathrm{min}$ and bake at $90\,^{\circ}\mathrm{C}$ for $2\,\mathrm{min}$. The multi-layer substrates are conductive enough to prevent charge-effects during the e-beam lithography (EBL) process.

4. Write the structure (after PEC correction) with EBL ($2.1\,\mathrm{C/m^2}$). This dose is chosen with the resist calibration in fig. B.0.1. The dose is chosen, such that the dose clears the resist in (a) and then the width and gap of the electrodes is adjusted with (b) to reach the metallization of 0.5.

5. Immerse the sample in H_2O for $1\,\mathrm{min}$ to remove the conductive resist layer and then develop with AR-500-546 by immersion for $1\,\mathrm{min}$. During this process the chip is moved (8-motion) to ensure a constant flow of the developer over the chip area. Stop the process with IPA and rinse the chip with IPA.

6. Evaporate $20\,\mathrm{nm}$ of Al on the sample with the PLASSYS UHV system.

7. Lift-off the resist layer and excess Al with the remover AR 600-71. Immerse the sample for $2\,\mathrm{h}$ in the remover. Remove the dissolved excess Al with a disposable pipette and repeat this step after a short immersion in fresh remover. Put the sample into the ultrasonic bath for $10\,\mathrm{s}$ with the lowest power and then rinse the sample with IPA and dry with N_2.

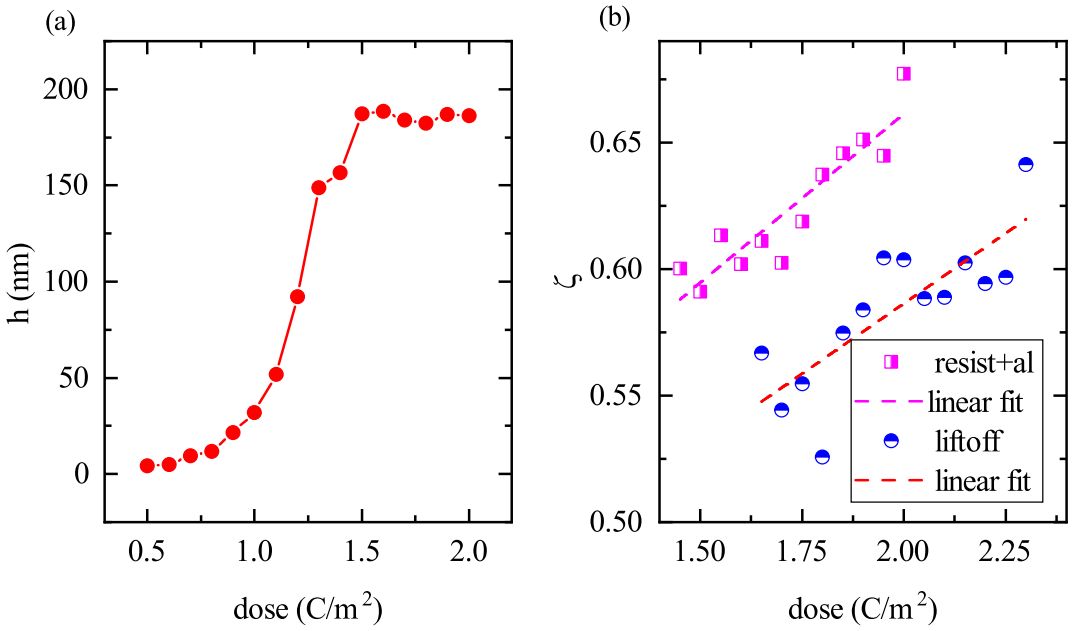

Figure B.0.1: CSAR 6200.09 resist calibration measurements. (a) AFM measurements of the height difference of an edge between area that has been exposed with the different doses and an unexposed area of the chip after development. A dose $> 1.6\,\mathrm{C/m^2}$ clears the resist layer on the chip. (b) Metallization p/a after and before the lift-off process for a structure with an array of $200\,\mathrm{nm}$ wide electrodes with the same gap written in EBL with different doses. Through the process blur the result for the metallization is larger than 0.5

.

Qubit fabrication

The fabrication of the qubit sample with the Josephson elements involves multiple steps. We start with the Non-Josephson elements continue with the fabrication of the SQUID and bandages for galvanic contact. The cleaning processes to remove surface oxides are very important for the qubit fabrication and more details are given in Ref. [23].

Non-Josephson elements

1. Clean the blank Si chip with acetone and IPA. Follow up with Piranha solution to remove organic contamination and then remove the silicon oxide with a BOE solution. Then a $150\,\mathrm{nm}$ thick Nb film is sputtered with the PLASSYS system at room temperature.

2. Spin-coat the sample with $40\,\mu\mathrm{l}$ of AZ MIR 701 at $4000\,\mathrm{RPM}$ for $1\,\mathrm{min}$ and bake the sample at $90\,^{\circ}\mathrm{C}$ for $75\,\mathrm{s}$.

3. Write the structure in the optical laserwriter with the exposure dose of $120\,\mathrm{mJ/cm^2}$.

4. Bake the sample at $110\,^{\circ}\mathrm{C}$ for $1\,\mathrm{min}$ and immerse the sample in the developer AZ MIF 726 for $60\,\mathrm{s}$ (constant 8-motion).

5. This chip with the resist mask is used in our reactive ion etching (RIE) system to selectively etch away the Nb. The mask is removed afterwards with the P1331 photo-resist stripper.

SQUID The SQUID is patterned with EBL, because the structures are so small.

1. Clean the chip with acetone and IPA, dry with N_2 and dehydrate the chip with a subsequent bake at $150\,^{\circ}\mathrm{C}$.

2. Spin-coat the chip with 27 µl of CSAR 6200.13 with $1500\,\mathrm{RPM}$ for $2\,\mathrm{min}$. Bake the chip for $1\,\mathrm{min}$ at $150\,^{\circ}\mathrm{C}$. Then spin-coat the sample with 25 µl of PMMA 950K AR-P 672.045 with $1600\,\mathrm{RPM}$ for $105\,\mathrm{s}$ for the second layer. Bake the chip for $3\,\mathrm{min}$ at $150\,^{\circ}\mathrm{C}$

3. Write the SQUID with EBL (after PEC correction) with $(4.2\,\mathrm{mJ/cm^2})$

4. Immerse the chip in the developer AR 600-546 for $2\,\mathrm{min}$ (constant 8-motion). Stop the process in IPA, rinse the chip with IPA and dry with N_2.

5. Evaporate $30\,\mathrm{nm}$ of Al with the PLASSYS UHV system. Dynamic oxidation of the chip for $40\,\mathrm{min}$. Evaporate another $70\,\mathrm{nm}$ of Al.

6. For lift-off immerse the chip in hot acetone ($70\,^{\circ}\mathrm{C}$). Let the chip soak in the acetone for $2\,\mathrm{h}$ and remove the Al/AlOx/Al from the chip the with a disposable pipette. Repeat this step until the chip looks clean. Remove the resist on the chip with immersion in the remover AR 600-71 for $10\,\mathrm{min}$. Stop the process with IPA, rinse the chip with IPA and dry with N_2.

Bandages Steps 1. - 4. are identical to the SQUID fabrication step, just that this time the bandages are written with EBL. In the PLASSYS UHV system we ion-mill mill remove the oxide layer on the SQUID and Nb structure with Ar-ion-milling for $270\,\mathrm{s}$ with a beam voltage of $400\,\mathrm{V}$, beam current $15\,\mathrm{mA}$ and $90\,\mathrm{V}$ acceleration voltage. Afterwards we evaporate $200\,\mathrm{nm}$ thick Al to provide galvanic contact between SQUID and the rest of the superconducting circuit elements on the chip. The lift-off process is identical to step 6. from the SQUID fabrication.

Flip-chip resist slab fabrication

We describe the details for the fabrication of the resist slabs, that provide the separation of the top and bottom chip for the flip-chip assembly, here.

1. Clean the qubit chip thoroughly in acetone ($70\,^\circ\mathrm{C}$) and IPA ($70\,^\circ\mathrm{C}$). Do not use the ultrasonic bath, because that might damage the SQUID.

2. Spin-coat the sample with $13\,\mu\mathrm{l}$ of mr DWL-5 epoxy resist at $3000\,\mathrm{RPM}$ for $30\,\mathrm{s}$. The resist is very viscose and we use a larger pipette and probably more resist than the nominal value. Bake the sample at $95\,^\circ\mathrm{C}$ for $3\,\mathrm{min}$.

3. Expose the sample in the mask-less laser writer with the exposure dose of $250\,\mathrm{mJ/cm^2}$. The laserwriter blanks the exposure by reducing the current below a threshold value when the laser-diode stops emitting light. For this resist it is essential that this threshold value is correct, because otherwise sections, that should remain unexposed, will be exposed.

4. First bake the sample at $65\,^\circ\mathrm{C}$ for $1\,\mathrm{min}$. In a subsequent bake the sample is at $95\,^\circ\mathrm{C}$ for $2\,\mathrm{min}$ and the design should be visible in the resist afterwards.

5. Immerse the sample in the developer mr Dev-600 for $3\,\mathrm{min}$. Stop the process in IPA, rinse in IPA and dry with N_2.

6. Hard-bake the sample at $150\,^\circ\mathrm{C}$ for $3\,\mathrm{min}$.

Bibliography

[1] Lord Rayleigh (J. Strutt), *On Waves Propagated along the Plane Surface of on Elastic Solid*, Proc. London Math Soc. **17**, 4 (1885).

[2] D. Morgan, *Surface Acoustic Wave Filters: With Applications to Electronic Communications and Signal Processing*, 2nd ed. (Academic Press, Amsterdam ; London, 2007).

[3] R. M. White and F. W. Voltmer, *DIRECT PIEZOELECTRIC COUPLING TO SURFACE ELASTIC WAVES*, Applied Physics Letters **7**, 314 (1965).

[4] W. Soluch, *Design of SAW Delay Lines for Sensors*, Sensors and Actuators A: Physical **67**, 60 (1998).

[5] S. Fujii, T. Odawara, H. Yamada, T. Omori, K.-y. Hashimoto, H. Torii, H. Umezawa, and S. Shikata, *Low Propagation Loss in a One-Port SAW Resonator Fabricated on Single-Crystal Diamond for Super-High-Frequency Applications*, IEEE Transactions on Ultrasonics, Ferroelectrics, and Frequency Control **60**, 986 (2013).

[6] C. C. W. Ruppel, *Acoustic Wave Filter Technology–A Review*, IEEE Transactions on Ultrasonics, Ferroelectrics, and Frequency Control **64**, 1390 (2017).

[7] D. R. Morgan, *Surface Acoustic Wave Devices and Applications: 1. Introductory Review*, Ultrasonics **11**, 121 (1973).

[8] K. Länge, B. E. Rapp, and M. Rapp, *Surface Acoustic Wave Biosensors: A Review*, Analytical and Bioanalytical Chemistry **391**, 1509 (2008).

[9] J. Camacho, L. Svilainis, and T. G. Álvarez-Arenas, *Ultrasonic Imaging and Sensors*, Sensors **22**, 7911 (2022).

[10] A. Kumar and R. Prajesh, *The Potential of Acoustic Wave Devices for Gas Sensing Applications*, Sensors and Actuators A: Physical **339**, 113498 (2022).

[11] A. D. O'Connell, M. Hofheinz, M. Ansmann, R. C. Bialczak, M. Lenander, E. Lucero, M. Neeley, D. Sank, H. Wang, M. Weides, J. Wenner, J. M. Martinis, and A. N. Cleland, *Quantum Ground State and Single-Phonon Control of a Mechanical Resonator*, Nature **464**, 697 (2010).

[12] Y. Chu, P. Kharel, W. H. Renninger, L. D. Burkhart, L. Frunzio, P. T. Rakich, and R. J. Schoelkopf, *Quantum Acoustics with Superconducting Qubits*, Science **358**, 199 (2017).

[13] M. Choquer, M. Weiss, E. D. S. Nysten, M. Lienhart, P. Machnikowski, D. Wigger, H. J. Krenner, and G. Moody, *Quantum Control of Optically Active Artificial Atoms With Surface Acoustic Waves*, IEEE Transactions on Quantum Engineering **3**, 1 (2022).

[14] K. J. Satzinger, Y. P. Zhong, H.-S. Chang, G. A. Peairs, A. Bienfait, M.-H. Chou, A. Y. Cleland, C. R. Conner, É. Dumur, J. Grebel, I. Gutierrez, B. H. November, R. G. Povey, S. J. Whiteley, D. D. Awschalom, D. I. Schuster, and A. N. Cleland, *Quantum Control of Surface Acoustic-Wave Phonons*, Nature **563**, 661 (2018).

[15] A. Bienfait, K. J. Satzinger, Y. P. Zhong, H.-S. Chang, M.-H. Chou, C. R. Conner, É. Dumur, J. Grebel, G. A. Peairs, R. G. Povey, and A. N. Cleland, *Phonon-Mediated Quantum State Transfer and Remote Qubit Entanglement*, Science **364**, 368 (2019), arXiv:1903.05672 .

[16] L. Fan, C.-L. Zou, R. Cheng, X. Guo, X. Han, Z. Gong, S. Wang, and H. X. Tang, *Superconducting Cavity Electro-Optics: A Platform for Coherent Photon Conversion between Superconducting and Photonic Circuits*, Science Advances **4**, eaar4994 (2018).

[17] S. A. Tadesse and M. Li, *Sub-Optical Wavelength Acoustic Wave Modulation of Integrated Photonic Resonators at Microwave Frequencies*, Nature Communications **5**, 5402 (2014).

[18] K. C. Balram, M. I. Davanço, J. D. Song, and K. Srinivasan, *Coherent Coupling between Radiofrequency, Optical and Acoustic Waves in Piezo-Optomechanical Circuits*, Nature Photonics **10**, 346 (2016).

[19] R. Manenti, *Circuit Quantum Acoustodynamics with Surface Acoustic Waves*, http://purl.org/dc/dcmitype/Text, University of Oxford (2018).

[20] A. Frisk Kockum, in *International Symposium on Mathematics, Quantum Theory, and Cryptography*, Mathematics for Industry, edited by T. Takagi, M. Wakayama, K. Tanaka, N. Kunihiro, K. Kimoto, and Y. Ikematsu (Springer, Singapore, 2021) pp. 125–146.

[21] T. Aref, P. Delsing, M. K. Ekström, A. F. Kockum, M. V. Gustafsson, G. Johansson, P. J. Leek, E. Magnusson, and R. Manenti, in *Superconducting Devices in Quantum Optics*, Quantum Science and Technology, edited by R. H. Hadfield and G. Johansson (Springer International Publishing, Cham, 2016) pp. 217–244.

[22] A. F. Kockum, G. Johansson, and F. Nori, *Decoherence-Free Interaction between Giant Atoms in Waveguide Quantum Electrodynamics*, Physical Review Letters **120**, 140404 (2018).

[23] N. Bruckmoser, *Development of a Fabrication Process for High Coherence Niobium Qubits*, Master's thesis, Technische Universität München, Garching (2021).

[24] C. CAMPBELL, *Surface Acoustic Wave Devices and Their Signal Processing Applications* (Elsevier, 2012).

[25] FARNELL, G. W. AND ADLER, E. L., in *Physical Acoustics Edited by Warren P. Mason*, Vol. 9 (Academic Press, New York and London, 1972) pp. 35–127.

[26] M. T. RESCH, *Non-Destructive Evaluation of Small Surface Cracks Using Surface Acoustic Waves*, Ph.D. thesis, Stanford University (1982).

[27] R. GROSS AND A. MARX, *Festkörperphysik* (De Gruyter, 2018).

[28] M. C. MÜHLENHOFF, *Microwave Frequency Magnetoacoustic Interactions in Ferromagnetic Thin Films*, Master's thesis, Technische Unversität München, Garching (2017).

[29] K. A. INGEBRIGTSEN, *Surface Waves in Piezoelectrics*, Journal of Applied Physics **40**, 2681 (1969).

[30] E. ADLER, *Matrix Methods Applied to Acoustic Waves in Multilayers*, IEEE Transactions on Ultrasonics, Ferroelectrics, and Frequency Control **37**, 485 (1990).

[31] A. JUNG, *Characterization of Surface Acoustic Wave Devices on Various Material Systems at Room and Cryogenic Temperatures*, Bachelor's Thesis, Technische Unversität München, Garching (2020).

[32] *COMSOL Multiphysics®*, v.5.5 COMSOL AB, Stockholm, Sweden (2019).

[33] J. RANSLEY, *Piezoelectric Materials: Applying the Standards* (2016).

[34] N. WALET, *Advanced Quantum Mechanics 2*, https://oer.physics.manchester.ac.uk/AQM2/Notes/Notes 3.4.html (2012).

[35] J. GAO, *The Physics of Superconducting Microwave Resonators*, Ph.D. thesis, California Institute of Technology, Pasadena, California (2008).

[36] S. PROBST, F. B. SONG, P. A. BUSHEV, A. V. USTINOV, AND M. WEIDES, *Efficient and Robust Analysis of Complex Scattering Data under Noise in Microwave Resonators*, Review of Scientific Instruments **86**, 024706 (2015).

[37] M. S. KHALIL, M. J. A. STOUTIMORE, F. C. WELLSTOOD, AND K. D. OSBORN, *An Analysis Method for Asymmetric Resonator Transmission Applied to Superconducting Devices*, Journal of Applied Physics **111**, 054510 (2012).

[38] P. J. PETERSAN AND S. M. ANLAGE, *Measurement of Resonant Frequency and Quality Factor of Microwave Resonators: Comparison of Methods*, Journal of Applied Physics **84**, 3392 (1998).

[39] H. WANG, S. SINGH, C. R. H. MCRAE, J. C. BARDIN, S.-X. LIN, N. MESSAOUDI, A. R. CASTELLI, Y. J. ROSEN, E. T. HOLLAND, D. P. PAPPAS, AND J. Y. MUTUS, *Cryogenic Single-Port Calibration for Superconducting Microwave Resonator Measurements*, Quantum Science and Technology **6**, 035015 (2021).

[40] D. Rieger, S. Günzler, M. Spiecker, A. Nambisan, W. Wernsdorfer, and I. M. Pop, *Fano Interference in Microwave Resonator Measurements* (2022), arXiv:2209.03036 [quant-ph] .

[41] qkitgroup, *Qkitgroup/Qkit* (2022).

[42] S. Datta and B. J. Hunsinger, *An Analytical Theory for the Scattering of Surface Acoustic Waves by a Single Electrode in a Periodic Array on a Piezoelectric Substrate*, Journal of Applied Physics **51**, 4817 (1980).

[43] S. Datta, *Surface Acoustic Wave Devices* (Prentice Hall, Englewood Cliffs, 1986).

[44] C. Waas, *Development of Scalable On-Chip Circuit Quantum Acoustodynamics*, Master's thesis, Technische Universität München, Garching (2021).

[45] R. Manenti, M. J. Peterer, A. Nersisyan, E. B. Magnusson, A. Patterson, and P. J. Leek, *Surface Acoustic Wave Resonators in the Quantum Regime*, Physical Review B **93**, 041411 (2016), arXiv:1510.04965 .

[46] M. Aspelmeyer, T. J. Kippenberg, and F. Marquardt, *Cavity Optomechanics*, Reviews of Modern Physics **86**, 1391 (2014).

[47] D. M. Pozar, *Microwave Engineering* (John Wiley & Sons, 2011).

[48] R. Manenti, *Surface Acoustic Wave Resonators for Quantum Information*, Master's thesis, University of Milan, Milan (2013).

[49] J. Slaboszewicz, *Computer-Aided Analysis and Design of Acoustic Wave Devices*, Master's thesis, Mc Gill University, Montreal (1993).

[50] J. P. Parekh and H. S. Tuan, *Effect of Groove-depth Variation on the Performance of Uniform SAW Grooved Reflector Arrays*, Applied Physics Letters **32**, 787 (1978).

[51] A. Slobodnik, *Surface Acoustic Waves and SAW Materials*, Proceedings of the IEEE **64**, 581 (1976).

[52] C. Müller, J. H. Cole, and J. Lisenfeld, *Towards Understanding Two-Level-Systems in Amorphous Solids: Insights from Quantum Circuits*, Reports on Progress in Physics **82**, 124501 (2019).

[53] M. Müller, T. Luschmann, A. Faltermeier, S. Weichselbaumer, L. Koch, G. B. P. Huber, H. W. Schumacher, N. Ubbelohde, D. Reifert, T. Scheller, F. Deppe, A. Marx, S. Filipp, M. Althammer, R. Gross, and H. Huebl, *Magnetic Field Robust High Quality Factor NbTiN Superconducting Microwave Resonators*, Materials for Quantum Technology **2**, 015002 (2022), arXiv:2112.08296 [cond-mat, physics:physics] .

[54] A. Blais, A. L. Grimsmo, S. M. Girvin, and A. Wallraff, *Circuit Quantum Electrodynamics*, Reviews of Modern Physics **93**, 025005 (2021).

[55] T. H. P. CHANG, *Proximity Effect in Electron-beam Lithography*, Journal of Vacuum Science and Technology **12**, 1271 (1975).

[56] *BEAMER*, v 6.3.0 GenISys GmbH (2022).

[57] *TRACER*, v 2.10.0 GenISys GmbH (2021).

[58] H. WARLIMONT AND W. MARTIENSSEN, *Springer Handbook of Materials Data*, 2nd ed., Springer Handbooks (Springer Cham, 2018).

[59] C. HEEG, *Spin Mechanics at Radio Frequencies*, Diploma thesis, Technische Unversität München, München (2010).

[60] R. L. COMSTOCK AND C. E. FAY, *Performance and Ferrimagnetic Material Considerations in Cryogenic Microwave Devices*, Journal of Applied Physics **36**, 1253 (1965).

[61] R. S. WEIS AND T. K. GAYLORD, *Lithium Niobate: Summary of Physical Properties and Crystal Structure*, Applied Physics A **37**, 191 (1985).

[62] A. W. WARNER, M. ONOE, AND G. A. COQUIN, *Determination of Elastic and Piezoelectric Constants for Crystals in Class (3m)*, The Journal of the Acoustical Society of America **42**, 1223 (1967).

[63] J. S. BROWDER AND S. S. BALLARD, *Thermal Expansion Data for Eight Optical Materials from 60 K to 300 K*, Applied Optics **16**, 3214 (1977).

[64] R. T. SMITH AND F. S. WELSH, *Temperature Dependence of the Elastic, Piezoelectric, and Dielectric Constants of Lithium Tantalate and Lithium Niobate*, Journal of Applied Physics **42**, 2219 (1971).

[65] R. MANENTI, M. J. PETERER, A. NERSISYAN, E. B. MAGNUSSON, A. PATTERSON, AND P. J. LEEK, *Surface Acoustic Wave Resonators in the Quantum Regime*, Physical Review B **93**, 041411 (2016), arXiv:1510.04965 .

[66] A. BRUNO, G. DE LANGE, S. ASAAD, K. L. VAN DER ENDEN, N. K. LANGFORD, AND L. DICARLO, *Reducing Intrinsic Loss in Superconducting Resonators by Surface Treatment and Deep Etching of Silicon Substrates*, Applied Physics Letters **106**, 182601 (2015).

[67] D. P. PAPPAS, M. R. VISSERS, D. S. WISBEY, J. S. KLINE, AND J. GAO, *Two Level System Loss in Superconducting Microwave Resonators*, IEEE Transactions on Applied Superconductivity **21**, 871 (2011).

[68] C. R. H. MCRAE, H. WANG, J. GAO, M. R. VISSERS, T. BRECHT, A. DUNSWORTH, D. P. PAPPAS, AND J. MUTUS, *Materials Loss Measurements Using Superconducting Microwave Resonators*, Review of Scientific Instruments **91**, 091101 (2020).

[69] H. Moriceau, F. Rieutord, F. Fournel, Y. L. Tiec, L. D. Cioccio, C. Morales, A. M. Charvet, and C. Deguet, *Overview of Recent Direct Wafer Bonding Advances and Applications*, Advances in Natural Sciences: Nanoscience and Nanotechnology **1**, 043004 (2011).

[70] C.-C. Wu, R.-H. Horng, D.-S. Wuu, T.-N. Chen, S.-S. Ho, C.-J. Ting, and H.-Y. Tsai, *Thinning Technology for Lithium Niobate Wafer by Surface Activated Bonding and Chemical Mechanical Polishing*, Japanese Journal of Applied Physics **45**, 3822 (2006).

[71] P. Rabiei and P. Gunter, *Optical and Electro-Optical Properties of Submicrometer Lithium Niobate Slab Waveguides Prepared by Crystal Ion Slicing and Wafer Bonding*, Applied Physics Letters **85**, 4603 (2004).

[72] S. Adachi, in *Properties of Group-IV, III-V and II-VI Semiconductors* (John Wiley & Sons, Ltd, 2005) Chap. 3, pp. 41–72.

[73] J. Krupka, J. Breeze, A. Centeno, N. Alford, T. Claussen, and L. Jensen, *Measurements of Permittivity, Dielectric Loss Tangent, and Resistivity of Float-Zone Silicon at Microwave Frequencies*, IEEE Transactions on Microwave Theory and Techniques **54**, 3995 (2006).

[74] W. H. Bragg and W. L. Bragg, *The Reflection of X-rays by Crystals*, Proceedings of the Royal Society of London. Series A, Containing Papers of a Mathematical and Physical Character **88**, 428 (1913).

[75] M. Scigliuzzo, L. E. Bruhat, A. Bengtsson, J. J. Burnett, A. F. Roudsari, and P. Delsing, *Phononic Loss in Superconducting Resonators on Piezoelectric Substrates*, New Journal of Physics **22**, 053027 (2020).

[76] M. Scheufele, *Tuning the Amplitude of the Spin Hall Magnetoresistance*, Master's thesis, Technische Universität München, Garching (1. December).

[77] S. Geprägs, *Magnetoelectric Interactions in Multiferroic Thin Films and Composites*, Ph.D. thesis, Technische Universität München, Garching (2011).

[78] *LEPTOS*, BRUKER (2004).

[79] J. S. Kelly, *Fault-Tolerant Superconducting Qubits*, Ph.D. thesis, University of California Santa Barbara, Santa Barbara (2015).

[80] P. Krantz, M. Kjaergaard, F. Yan, T. P. Orlando, S. Gustavsson, and W. D. Oliver, *A Quantum Engineer's Guide to Superconducting Qubits*, Applied Physics Reviews **6**, 021318 (2019), arXiv:1904.06560 .

[81] C. R. Conner, A. Bienfait, H.-S. Chang, M.-H. Chou, É. Dumur, J. Grebel, G. A. Peairs, R. G. Povey, H. Yan, Y. P. Zhong, and A. N. Cleland, *Superconducting Qubits in a Flip-Chip Architecture*, Applied Physics Letters **118**, 232602 (2021).

[82] M. A. Nielsen and I. L. Chuang, *Quantum Computation and Quantum Information*, tenth ed. (Camebridge University Press, 2016).

[83] L. S. Bishop, *Circuit Quantum Electrodynamics*, Ph.D. thesis, Yale University (2010).

[84] S. Filipp, *Quantum Computing qith Superconducting Qubits 2: Advanced Methods* (2021).

[85] A. Blais, R.-S. Huang, A. Wallraff, S. M. Girvin, and R. J. Schoelkopf, *Cavity Quantum Electrodynamics for Superconducting Electrical Circuits: An Architecture for Quantum Computation*, Physical Review A **69**, 062320 (2004).

[86] J. Koch, T. M. Yu, J. Gambetta, A. A. Houck, D. I. Schuster, J. Majer, A. Blais, M. H. Devoret, S. M. Girvin, and R. J. Schoelkopf, *Charge-Insensitive Qubit Design Derived from the Cooper Pair Box*, Physical Review A **76**, 042319 (2007).

[87] M. Göppl, A. Fragner, M. Baur, R. Bianchetti, S. Filipp, J. M. Fink, P. J. Leek, G. Puebla, L. Steffen, and A. Wallraff, *Coplanar Waveguide Resonators for Circuit Quantum Electrodynamics*, Journal of Applied Physics **104**, 113904 (2008).

[88] G. B. P. Huber, *Designing Superconducting Qubit Chips and Multi-Qubit Couplers*, Master's thesis, Technische Unversität München, Garching (2021).

[89] A. Blais, R.-S. Huang, A. Wallraff, S. M. Girvin, and R. J. Schoelkopf, *Cavity Quantum Electrodynamics for Superconducting Electrical Circuits: An Architecture for Quantum Computation*, Physical Review A **69**, 062320 (2004).

[90] V. B. Braginsky and F. Y. Khalili, *Quantum Nondemolition Measurements: The Route from Toys to Tools*, Reviews of Modern Physics **68**, 1 (1996).

[91] Y. Y. Gao, M. A. Rol, S. Touzard, and C. Wang, *Practical Guide for Building Superconducting Quantum Devices*, PRX Quantum **2**, 040202 (2021).

[92] J. D. Jackson, *Klassische Elektrodynamik*, 5th ed. (De Gruyter, 2006).

[93] S. Caniggia and F. Maradei, in *Signal Integrity and Radiated Emission of High-Speed Digital Systems* (John Wiley & Sons, Ltd, 2008) pp. 481–486.

[94] F. Marxer, A. Vepsäläinen, S. W. Jolin, J. Tuorila, A. Landra, C. Ockeloen-Korppi, W. Liu, O. Ahonen, A. Auer, L. Belzane, V. Bergholm, C. F. Chan, K. W. Chan, T. Hiltunen, J. Hotari, E. Hyyppä, J. Ikonen, D. Janzso, M. Koistinen, J. Kotilahti, T. Li, J. Luus, M. Papic, M. Partanen, J. Räbinä, J. Rosti, M. Savytskyi, M. Seppälä, V. Sevriuk, E. Takala, B. Tarasinski, M. J. Thapa, F. Tosto, N. Vorobeva, L. Yu, K. Y. Tan, J. Hassel, M. Möttönen, and J. Heinsoo, *Long-Distance Transmon Coupler with CZ Gate Fidelity above 99.8%* (2022), arXiv:2208.09460 [quant-ph] .

[95] Y. Chu, P. Kharel, T. Yoon, L. Frunzio, P. T. Rakich, and R. J. Schoelkopf, *Creation and Control of Multi-Phonon Fock States in a Bulk Acoustic-Wave Resonator*, Nature **563**, 666 (2018).

[96] R. Manenti, A. F. Kockum, A. Patterson, T. Behrle, J. Rahamim, G. Tancredi, F. Nori, and P. J. Leek, *Circuit Quantum Acoustodynamics with Surface Acoustic Waves*, Nature Communications **8**, 975 (2017), arXiv:1703.04495 .

[97] P. Arrangoiz-Arriola, E. A. Wollack, M. Pechal, J. D. Witmer, J. T. Hill, and A. H. Safavi-Naeini, *Coupling a Superconducting Quantum Circuit to a Phononic Crystal Defect Cavity*, Physical Review X **8**, 031007 (2018).

[98] P. Arrangoiz-Arriola, E. A. Wollack, Z. Wang, M. Pechal, W. Jiang, T. P. McKenna, J. D. Witmer, R. Van Laer, and A. H. Safavi-Naeini, *Resolving the Energy Levels of a Nanomechanical Oscillator*, Nature **571**, 537 (2019).

[99] D. Rosenberg, D. Kim, R. Das, D. Yost, S. Gustavsson, D. Hover, P. Krantz, A. Melville, L. Racz, G. O. Samach, S. J. Weber, F. Yan, J. L. Yoder, A. J. Kerman, and W. D. Oliver, *3D Integrated Superconducting Qubits*, npj Quantum Information **3**, 1 (2017).

[100] Z. K. Minev, T. G. McConkey, M. Takita, A. D. Corcoles, and J. M. Gambetta, *Circuit Quantum Electrodynamics (cQED) with Modular Quasi-Lumped Models*, arXiv:2103.10344 [cond-mat, physics:quant-ph] (2021), arXiv:2103.10344 [cond-mat, physics:quant-ph] .

[101] W. Yi-Lin, H. Deng, Y. Hai-Feng, X. Guang-Min, T. Ye, L. Jie, C. Ying-Fei, Z. Shi-Peng, and Z. Dong-Ning, *Fabrication of Al/AlOx/Al Josephson Junctions and Superconducting Quantum Circuits by Shadow Evaporation and a Dynamic Oxidation Process*, Chinese Physics B **22**, 060309 (2013).

[102] S. E. Nigg, H. Paik, B. Vlastakis, G. Kirchmair, S. Shankar, L. Frunzio, M. H. Devoret, R. J. Schoelkopf, and S. M. Girvin, *Black-Box Superconducting Circuit Quantization*, Physical Review Letters **108**, 240502 (2012).

[103] J. Bourassa, F. Beaudoin, J. M. Gambetta, and A. Blais, *Josephson-Junction-Embedded Transmission-Line Resonators: From Kerr Medium to in-Line Transmon*, Physical Review A **86**, 013814 (2012).

[104] E. Marchiori, L. Ceccarelli, N. Rossi, G. Romagnoli, J. Herrmann, J.-C. Besse, S. Krinner, A. Wallraff, and M. Poggio, *Magnetic Imaging of Superconducting Qubit Devices with Scanning SQUID-on-tip*, Applied Physics Letters **121**, 052601 (2022).

[105] G. J. Dolan, *Offset Masks for Lift-off Photoprocessing*, Applied Physics Letters **31**, 337 (1977).

[106] A. Dunsworth, A. Megrant, C. Quintana, Z. Chen, R. Barends, B. Burkett, B. Foxen, Y. Chen, B. Chiaro, A. Fowler, R. Graff, E. Jeffrey, J. Kelly, E. Lucero, J. Y. Mutus, M. Neeley, C. Neill, P. Roushan, D. Sank, A. Vainsencher, J. Wenner, T. C. White, and J. M. Martinis, *Characterization and Reduction of Capacitive Loss Induced by Sub-Micron Josephson Junction Fabrication in Superconducting Qubits*, Applied Physics Letters **111**, 022601 (2017).

[107] C. R. Conner, A. Bienfait, H.-S. Chang, M.-H. Chou, É. Dumur, J. Grebel, G. A. Peairs, R. G. Povey, H. Yan, Y. P. Zhong, and A. N. Cleland, *Superconducting Qubits in a Flip-Chip Architecture*, Applied Physics Letters **118**, 232602 (2021).

[108] S. Krinner, S. Storz, P. Kurpiers, P. Magnard, J. Heinsoo, R. Keller, J. Lütolf, C. Eichler, and A. Wallraff, *Engineering Cryogenic Setups for 100-Qubit Scale Superconducting Circuit Systems*, EPJ Quantum Technology **6**, 1 (2019).

[109] J. Goetz, *The Interplay of Superconducting Quantum Circuits and Propagating Microwave States*, Ph.D. thesis, Technische Unversität München, Garching (2017).

[110] M. Müting, *Time Domain Characterization of a Transmon Qubit*, Master's thesis, Technische Iniversität München, Garching (2015).

[111] S. Krinner, N. Lacroix, A. Remm, A. Di Paolo, E. Genois, C. Leroux, C. Hellings, S. Lazar, F. Swiadek, J. Herrmann, G. J. Norris, C. K. Andersen, M. Müller, A. Blais, C. Eichler, and A. Wallraff, *Realizing Repeated Quantum Error Correction in a Distance-Three Surface Code*, Nature **605**, 669 (2022).

[112] Atanasova , Desislava Gancheva, *Fabrication and Characterization of a Dimer Josephson Juncion Array Amplifier*, Master's thesis, Universität Innsbruck, Innsbruck (2020).

[113] J. P. Martinez, *Circuit Quantum Electrodynamics with Transmon Qubits*, Master's thesis, Technische Universität München, Munich (2015).

[114] J. Schirk, *Controlling the Environment of Superconducting Qubits*, Master's thesis, Technische Unversität München, Garching (2022).

[115] E. A. Sete, A. Q. Chen, R. Manenti, S. Kulshreshtha, and S. Poletto, *Floating Tunable Coupler for Scalable Quantum Computing Architectures*, Physical Review Applied **15**, 064063 (2021).

[116] R. Manenti, A. F. Kockum, A. Patterson, T. Behrle, J. Rahamim, G. Tancredi, F. Nori, and P. J. Leek, *Circuit Quantum Acoustodynamics with Surface Acoustic Waves*, Nature Communications **8**, 975 (2017).

[117] L. B. Nguyen, Y.-H. Lin, A. Somoroff, R. Mencia, N. Grabon, and V. E. Manucharyan, *High-Coherence Fluxonium Qubit*, Physical Review X **9**, 041041 (2019).

[118] F. Bao, H. Deng, D. Ding, R. Gao, X. Gao, C. Huang, X. Jiang, H.-S. Ku, Z. Li, X. Ma, X. Ni, J. Qin, Z. Song, H. Sun, C. Tang, T. Wang, F. Wu, T. Xia, W. Yu, F. Zhang, G. Zhang, X. Zhang, J. Zhou, X. Zhu, Y. Shi, J. Chen, H.-H. Zhao, and C. Deng, *Fluxonium: An Alternative Qubit Platform for High-Fidelity Operations*, Physical Review Letters **129**, 010502 (2022).

[119] W. Tanski, *Surface Acoustic Wave Resonators on Quartz*, IEEE Transactions on Sonics and Ultrasonics **26**, 93 (1979).

[120] A. B. Randles, M. Esashi, and S. Tanaka, *Etch Rate Dependence on Crystal Orientation of Lithium Niobate*, IEEE Transactions on Ultrasonics, Ferroelectrics, and Frequency Control **57**, 2372 (2010).

[121] J. Bühler, F.-P. Steiner, and H. Baltes, *Silicon Dioxide Sacrificial Layer Etching in Surface Micromachining*, Journal of Micromechanics and Microengineering **7**, R1 (1997).

[122] C. J. Sarabalis, Y. D. Dahmani, A. Y. Cleland, and A. H. Safavi-Naeini, *S-Band Delay Lines in Suspended Lithium Niobate*, Journal of Applied Physics **127**, 054501 (2020).

[123] L. S. Lim, L. C. Wai, D. X. Tham, and Q. Zhang, in *2013 IEEE 15th Electronics Packaging Technology Conference (EPTC 2013)* (2013) pp. 857–862.

[124] memsstar, *HF Acid Etch vs HF Vapor Etch* (2018).

[125] Y.-C. Chang, in *2009 2nd International Conference on Biomedical Engineering and Informatics* (2009) pp. 1–6.

Acknowledgements/Danksagungen

The last year has been at times challenging and my Master's thesis would not have been possible without the support of many people in and outside of the WMI. Even though this is in no way an exhaustive list, I want to thank some of them:

Dieses zuweilen anstrengende letzte Jahr der Masterarbeit wäre ohne die Unterstützung einiger Personen an- und außerhalb des WMI nicht möglich gewesen. Obwohl diese Aufzählung bestimmt nicht vollständig ist möchte ich einigen davon namentlich danken:

Professor Gröblacher for supplying the LNO-Si multi-layer substrates for my SAW resonators.

Hans, du hast mich vor jetzt knapp drei Jahren an das WMI gebracht. In den ersten zwei Jahren des Studiums sitzt man in vielen Vorlesungen aber die meisten Studenten (mich inbegriffen) haben überhaupt keinen Kontakt oder Bezug zu dem der am Pult die Vorlesung hält – diesen Umstand muss man im Kopf haben wenn ich schreibe wie nachhaltig du mich beieindruckt hast, als du dir in meiner Bachelorarbeit die Zeit genommen hast um mit mir Ideen auszutauschen. Das hat mich für die Masterarbeit wieder zu dir ans WMI gebracht. Auch wenn du viel zu tun hast gab es immer die Möglichkeit mich mit dir auszutauschen. Die Zusammenarbeit mit dir und allen voran deine nahezu unerschöpflichen Ideen haben diese Arbeit erst zu dem gemacht was sie jetzt ist.

Thomas, du hast es jetzt auch seit fast drei Jahren mit mir ausgehalten und hast dafür gesorgt, dass auch ich als Masterstudent irgendwie dazugehört habe. Dein enormes Wissen über die Setups für die Experimente, insbesondere für die Time-Domain beeindruckt mich immer wieder und war immer sehr hilfreich. Das meiste was ich in der Experimentalphysik weiß habe ich von dir gelernt.

Marius, weil mir selbst eine kurze Auszeit wie mein Besuch bei dir in Stockholm sehr viel Kraft gegeben hat um das ganze Jahr durchzustehen. Es ist in jeden Fall sehr schade dass wir uns am WMI weitgehend verpasst haben.

Lukas, zu Beginn der Masterarbeit habe ich noch nicht gewusst was für ein Glücksfall es ist, dass wir zeitgleich anfangen. Die häufigen Diskussionen mit dir über physikalische Konzepte, wie zum Beispiel JPAs, hat mein physikalisches Verständnis und meine Masterarbeit weitergebracht. Das Jahr wäre ohne dich in jedem Fall schlechter gewesen.

Patricia, du hast mir geholfen wenn unkluge Experimente im Reinraum mit Remover schiefgelaufen sind. Es hat mir immer Spaß gemacht mit dir zu reden und deine Gesellschaft wird mir in Zukunft fehlen.

Christopher, für die tolle Vorarbeit die du an unserem Thema geleistet hast und mir viele Steine aus dem Weg geschoben hast. Ein solcher Stein ist zum Beispiel die PEC, ohne die eine Fabrikation der SAW Resonatoren kaum möglich gewesen wäre. Ich hoffe sehr dass

meine Masterarbeit einmal eine ähnlich gute Grundlage für meinen Nachfolger ist.
Julian und Christian für all die lustigen Diskussionen und sonstige Vorkommnisse in unserem Büro. Es hat immer Spaß gemacht.
Niklas, Moni, Flo und Johannes für eure Ratschläge, Unterstützung und Hilfe.
Franz, du hast mir viel über Cryos beigebracht und es war immer gut mit dir zu reden.
Ivan, for setting up the qubit measurement setup at the Bottomloader, without your work our qubit measurements would have been far more difficult.
Kedar and Daniil with you around I never felt unwelcome and I will never forget, that you two reached out to me in a moment when not many (including myself) would have done so.
Svenja und Pascal, weil ihr immer für Ablenkung von der Physik gesorgt habt wenn ich es brauchte und du Pascal hast dafür gesorgt dass ich auch nach dem Jahr noch halbwegs in form bin.
Meinem Opa, Papa, Mama und beiden Geschwistern Becci und Domi für eure andauernde Unterstützung.
Unser Familienhund Cindy war mir während meiner Masterarbeit und auch die Jahre da-

vor immer eine große Stütze. Sie hat sich immer gefreut wenn ich nach Hause gekommen bin und danach war meine Laune besser, egal wie der Tag gelaufen ist. Am 5. Oktober 2022 ist Cindy leider im stolzen Hundealter von 13 Jahren verstorben. Sie fehlt jeden Tag aufs Neue wenn ich nach Hause komme und sie nicht hinter der Haustür liegt.